Study of Double-Hypernuclei with Hybrid-Emulsion Method

Hitoshi Takahashi

DISSERTATION

Submitted in Partial Fulfillment of
the Requirements for the Degree of

Doctor of Science

Department of Physics
Faculty of Science
Kyoto University

Jan, 2003

Abstract

An experimental study of double-strangeness nuclei has been performed with a scintillating-fiber/emulsion hybrid method. The experiment has been carried out at the KEK 12 GeV proton synchrotron using a 1.66 GeV/c separated K^- meson beam. We have completed the analysis of 32 % of total emulsion data, among which we have successfully observed three examples of the sequential weak decay of a double-hypernucleus and two events of the production of twin hypernuclei.

The second double-hypernucleus event, named "Nagara event", was interpreted uniquely as a $^6_{\Lambda\Lambda}$He double-hypernucleus ("Lambpha", $\hat{\alpha}$). The binding energy of the two Λ hyperons, $B_{\Lambda\Lambda}$, and the Λ-Λ interaction energy, $\Delta B_{\Lambda\Lambda}$, have been determined for the first time without the ambiguities arising from the possible production in excited states. The value of the Λ-Λ interaction energy was obtained as $\Delta B_{\Lambda\Lambda} = 1.01 \pm 0.20 \, ^{+0.18}_{-0.11}$ MeV, where the Ξ^- binding energy of an atomic $3D$ state in ^{12}C, 0.13 MeV, is used as the most probable value. It demonstrated that the Λ-Λ interaction is attractive but considerably weaker than that widely claimed. The lower limit of the mass of the H dibaryon has been obtained as 2223.7 MeV/c^2 at a 90% confidence level. It narrowed the allowed mass region of the bound H dibaryon to only 7.7 MeV/c^2 below the two-Λ mass.

The weak decays of double-hypernuclei have been investigated experimentally for the first time with respect to the Λ-Λ weak interaction and the existence of the H nuclei. The search for the $\Lambda\Lambda \rightarrow \Sigma^- p$ decay of double-hypernuclei has been performed by detecting the Σ^- hyperon captures and decays in emulsion. Among 166 samples of the Ξ^- capture events, no such event has been observed. The upper limit of the product of the probability of double-hypernuclear production from a Ξ^- hyperon capture at rest in emulsion, $P(\Xi^-_{stop} \rightarrow \, _{\Lambda\Lambda}Z)$, and the branching ratio of the decay mode, $Br(\Lambda\Lambda \rightarrow \Sigma^- p)$, has been obtained as $P(\Xi^-_{stop} \rightarrow \, _{\Lambda\Lambda}Z) \cdot Br(\Lambda\Lambda \rightarrow \Sigma^- p) < 2$ % at a 90 % confidence level. With a rough estimation to the value of $P(\Xi^-_{stop} \rightarrow \, _{\Lambda\Lambda}Z)$ using the result of the previous emulsion experiment, the branching ratio was deduced to be $Br(\Lambda\Lambda \rightarrow \Sigma^- p) < 12$ %.

Contents

Chapter 1

Introduction

1.1 Baryon-baryon interaction

Although the strong interaction between quarks and gluons is well described by quantum chromodynamics (QCD), it is still difficult to derive the nuclear force from QCD due to its non-perturbative nature. As for the strong interaction in the non-perturbative region, phenomenological quark models have been developed with a great success. The simple quark assignment for baryons, as composites of three quarks, and mesons, as those of a quark-antiquark pair, consistently explains their spin, parity, charge, and magnetic moment. The "hyperfine splitting" of the hadron energy levels is also well understood for low-lying states by introducing the color-magnetic interaction associated with the color charge and spin of quarks, as the hyperfine splitting of the energy level of a hydrogen atom due to magnetic moments of the constituent proton and electron. The color-magnetic interaction is parametrized as

$$\Delta = -\alpha \sum_{i<j} \vec{\sigma}_i \cdot \vec{\sigma}_j \ \vec{\lambda}_i \cdot \vec{\lambda}_j / m_i m_j, \tag{1.1}$$

where $\vec{\sigma}_i$ and $\vec{\lambda}_i$ represent the Pauli spin matrix and the Gell-Mann color matrix, respectively, and m_i is the mass of the i-th quark. The factor α denotes the interaction strength. Under $\mathrm{SU(3)_{flavor}}$ symmetry, the sum becomes

$$\sum_{i<j} \vec{\sigma}_i \cdot \vec{\sigma}_j \ \vec{\lambda}_i \cdot \vec{\lambda}_j / m_i m_j = 8N - \frac{1}{2}C_6 + \frac{4}{3}J(J+1), \tag{1.2}$$

where N is the total number of constituent quarks, and J and C_6 represent their angular momentum and eigenvalue of the $\mathrm{SU(6)_{color\text{-}spin}}$ Casimir operator, respectively.

One of the main aim of the strangeness nuclear physics is to extend our detailed knowledge on the nucleon-nucleon (NN) interaction toward the unified understanding of baryon-baryon interactions based on $\mathrm{SU(3)_{flavor}}$ symmetry. Figure 1.1 tabulates irreducible representations for two-baryon systems based on $\mathrm{SU(3)_{flavor}}$. Although the NN interaction has been well studied with rich experimental data, information derived from them is limited to only $\mathbf{27}_s$ and $\overline{\mathbf{10}}_a$ sectors

27s
S=0 NN(T=1)
S=-1 ΣN(T=3/2) ΣN-ΛN(T=1/2)
S=-2 ΣΣ(T=2) ΞN-ΣΛ-ΣΣ(T=1) ΞN-ΣΣ-ΛΛ(T=0)
S=-3 ΞΣ(T=3/2) ΞΣ-ΞΛ(T=1/2)
S=-4 ΞΞ(T=1)

$\overline{10}$a
S=0 NN(T=0)
S=-1 ΣN-ΛN(T=1/2)
S=-2 ΞN-ΣΛ(T=1)
S=-3 ΞΣ(T=3/2)

10a
S=-1 ΣN(T=3/2)
S=-2 ΞN-ΣΛ-ΣΣ(T=1)
S=-3 ΞΣ-ΞΛ(T=1/2)
S=-4 ΞΞ(T=0)

8s
S=-1 ΣN-ΛN(T=1/2)
S=-2 ΞN-ΣΛ(T=1) ΞN-ΣΣ-ΛΛ(T=0)
S=-3 ΞΣ-ΞΛ(T=1/2)

8a
S=-1 ΣN-ΛN(T=1/2)
S=-2 ΞN-ΣΛ-ΣΣ(T=1) ΞN(T=0)
S=-3 ΞΣ-ΞΛ(T=1/2)

1s   ●   S=-2 ΞN-ΣΣ-ΛΛ(T=0)

Figure 1.1: Irreducible representations for two-baryon system based on $\mathrm{SU(3)_{flavor}}$.

of the baryon-baryon interaction. Recent progress of the studies on the hyperon-nucleon interactions gives us information of multiplets other than $\mathbf{1}_s$ sector, even though experimental results are still poor compared to the NN sector. Information of $\mathbf{1}_s$ sector can be obtained only from the studies on doubly strange systems. However, experimental data for $S = -2$ sector on baryon-baryon interaction is extremely limited so far, as mentioned later.

The observation of double-Λ hypernuclei gives important information about the Λ-Λ interaction. The binding energy of two Λ hyperons, $B_{\Lambda\Lambda}$, and the Λ-Λ interaction energy, $\Delta B_{\Lambda\Lambda}$, can be obtained from the measurement of the masses of double-Λ nuclei, where $B_{\Lambda\Lambda}$ and $\Delta B_{\Lambda\Lambda}$ are defined by

$$
\begin{aligned}
B_{\Lambda\Lambda}(^{A}_{\Lambda\Lambda}Z) &= M(^{A-2}Z) + 2M(\Lambda) - M(^{A}_{\Lambda\Lambda}Z) && (1.3) \\
\Delta B_{\Lambda\Lambda}(^{A}_{\Lambda\Lambda}Z) &= B_{\Lambda\Lambda}(^{A}_{\Lambda\Lambda}Z) - 2B_{\Lambda}(^{A-1}_{\Lambda}Z). && (1.4)
\end{aligned}
$$

Since hyperon-hyperon scattering experiments are extremely difficult, the observation of double-hypernuclei is currently an unique experimental approach to extract the information about the Λ-Λ interaction.

Double-Λ hypernuclei are closely related to the existence of an H dibaryon. The H dibaryon was originally predicted by Jaffe in 1977 [1] as a particle constituting six quarks of *uuddss* with the configuration of color-singlet, $SU(3)_{\text{flavor}}$-singlet, and $J^{PC} = 0^{++}$. The eigenvalue of the Casimir operator C_6 in eq. (1.2) becomes 144 in such a configuration. It gives strongly attractive color-magnetic interaction of $\Delta = -24\alpha$. Jaffe predicted the mass of the H dibaryon using the MIT bag model to be 2150 MeV/c^2, which is smaller than twice the Λ hyperon mass. Since then, many theorists have calculated its mass using various models and their results vary from below two nucleons mass to above the two-Λ threshold. The theoretical calculations on the H dibaryon are reviewed in Ref. [2].

If the mass of the H dibaryon, $M(H)$, was less than twice the Λ hyperon mass in a nucleus, two Λ hyperons in the nucleus would be expected to form the H immediately. With this assumption, the lower limit of the mass of the H dibaryon can be calculated from the following relation;

$$M(H) > 2M(\Lambda) - B_{\Lambda\Lambda}, \qquad (1.5)$$

where $M(\Lambda)$ is the mass of a Λ hyperon in free space. This relation would not be changed even if an observed double-hypernucleus had been the H nucleus. If the H dibaryon is bound in a nucleus, the binding energy of the H, B_H, can be defined by

$$B_H = M(^{A-2}Z) + M(H) - M(^{A}_{H}Z), \qquad (1.6)$$

where the mass of the H nucleus, $M(^{A}_{H}Z)$, is equal to $M(^{A}_{\Lambda\Lambda}Z)$ in eq. (1.3). By combining eq. (1.3) and eq. (1.6), the H mass can be written as

$$
\begin{aligned}
M(H) &= 2M(\Lambda) - B_{\Lambda\Lambda} + B_H \\
&> 2M(\Lambda) - B_{\Lambda\Lambda},
\end{aligned}
$$

exactly same as eq. (1.5). In terms of baryon configuration, the H state may appear as a result of the mixing of $\Lambda\Lambda$, ΞN, and $\Sigma\Sigma$ states in a nucleus:

$$|H\rangle = \sqrt{\frac{1}{8}}\,|\Lambda\Lambda\rangle + \sqrt{\frac{4}{8}}\,|\Xi N\rangle - \sqrt{\frac{3}{8}}\,|\Sigma\Sigma\rangle. \qquad (1.7)$$

Theoretical calculations of the binding energies of double-hypernuclei have been made since the 1960s, aiming to obtain information on the Λ-Λ interaction [3, 4, 5]. The effective Λ-Λ interaction was derived from the one-boson-exchange (OBE) models [6][7, 8, 9][10], the quark-cluster model (QCM) [11], and relativistic mean field (RMF) approaches [12].

A number of OBE potentials for the baryon-baryon interactions have been developed by the Nijmegen group. Model D (NHC-D) [13, 14] and F (NHC-F)[15] are two versions of hard-core OBE potentials. Model F includes a scalar-meson nonet, whereas only the unitary singlet out of the nonet is considered in model D. Model F also differs from model D in stronger SU(3) constraints on the hard core radius between various channels. Model D gives a strong attraction in $\Lambda\Lambda$ ($\Delta B_{\Lambda\Lambda} \sim 5$ MeV), while model F leads rather weak interactions. Model NSC [16] is the soft-core OBE potential and NSC97 [17] is its new version. Instead of the phenomenological hard core, the soft core models, NSC and NSC97, employ Reggeon exchanges, including Pomeron and tensor meson exchanges, which produce short-range repulsive forces. Both of NSC and NSC97 models give a weakly attractive Λ-Λ interaction. Recently, the Nijmegen group has constructed an Extended-Soft-Core model (ESC00) [18]. In the ESC00, the soft-core OBE models are extended to include a second scalar-meson nonet, two-pseudo-scalar exchange (TPSE), and meson-pair exchange (MPE). This new soft-core potential gives strongly attractive Λ-Λ interaction of $\Delta B_{\Lambda\Lambda} > 4$ MeV, in contrast to the other soft-core OBE models. These Nijmegen potentials have no H dibaryon state.

The Ehime group presented another OBE model [19]. They extended a NN OBE potential by Ueda, Riewe, and Green to ΛN and $\Lambda\Lambda$ systems in the nonet meson scheme with effective scalar and vector mesons incorporating the correlated and uncorrelated two octet mesons. This model predicts strong Λ-Λ attraction of $\Delta B_{\Lambda\Lambda} > 3.6$ MeV [19, 11] and no H bound state.

The Kyoto-Niigata group proposed the quark-cluster-model (QCM) [20, 21]. In the QCM's, the short-range baryon-baryon interaction is described by (3q)-(3q) resonating-group-method (RGM) formulation of the SU(6)$_{\text{spin-flavor}}$ quark model, while the medium- and long-range forces are employed by the effective meson exchange potentials (EMEP). In their RGM-F model, the medium-range central component in EMEP is generated from the scalar-meson nonet exchange in the Nijmegen model-F potential, and the long-range tensor force is from the π and K mesons. This model gives a large overbinding for double-hypernuclei as $\Delta B_{\Lambda\Lambda}(^{10}_{\Lambda\Lambda}\text{Be}) = 10.2$ MeV [11]. The EMEP is updated in their FSS model by calculating the spin-flavor factors exactly at the quark level and including the spin-spin terms originating from all the pseudo-scalar mesons. It gives weaker at-

traction for the Λ-Λ interaction ($\Delta B_{\Lambda\Lambda}(^{10}_{\Lambda\Lambda}\text{Be}) = 2.5$ MeV) [11]. The RGM-F and FSS versions predict a bound H dibaryon and no H dibaryon state, respectively.

In the $\sigma + \omega$ model of the relativistic-mean-field (RMF) theory, the baryons couple to the mean field of a scalar (σ) and vector (ω, ϕ, ρ) mesons. It well reproduces spectra of single-Λ hypernuclei and gives the weakly attractive Λ-Λ interaction of $\Delta B_{\Lambda\Lambda} \sim 1$ MeV [12]. By introducing the coupling to an additional scalar (σ^*) and vector (ϕ) fields, the calculated value of $\Delta B_{\Lambda\Lambda}$ is increased to about 3 MeV [12].

Hyperons are expected to exist in dense matter, such as the inner crust of neutron stars. The hyperon components in the core region of neutron stars have been considered to play a important role in the rapid cooling scenario of neutron stars. The "hyperon cooling" has been studied [22] as one of the non-standard cooling scenarios to explain the low surface temperatures observed for some neutron stars [23]. Some studies found that the hyperon cooling is too rapid, but the occurance of the hyperon superfluidity suppresses the hyperon direct Urca process [24, 25, 26, 27]. These calculations were performed by using effective interaction between hyperons based on the limited hypernuclear data. The hyperon-hyperon interaction has drawn attention increasingly.

1.2 Past experiments regarding to $S = -2$

There are three reports on the observations of double-Λ hypernuclei in nuclear emulsion. Over three decades ago, M. Danysz *et al.* reported the sequential weak decay of a double-hypernucleus produced from a Ξ^- hyperon capture at rest in emulsion [28]. The event remained two interpretations on the nuclide, $^{10}_{\Lambda\Lambda}\text{Be}$ or $^{11}_{\Lambda\Lambda}\text{Be}$, but later reanalysis indicated the production of $^{10}_{\Lambda\Lambda}\text{Be}$, which leads to $\Delta B_{\Lambda\Lambda} = 4.3 \pm 0.4$ MeV [29]. However, there still remains the possibility of the decay to the single-hypernucleus in excited states, which gives the different value of $\Delta B_{\Lambda\Lambda}$. It should be noticed that it was found in emulsion exposed to about 10^4 K^- mesons, and the expected number of stopped Ξ^- hyperons was no more than four [29].

Another example of the double-hypernucleus was presented by D.J. Prowse in 1960s [30]. It was identified as $^6_{\Lambda\Lambda}\text{He}$, and the value of $\Delta B_{\Lambda\Lambda}$ was obtained to be 4.6 ± 0.5 MeV. However, only a schematic drawing of the event was given in the Letter, and measured angles were not presented. Its authenticity was considered doubtful [29].

Mondal *et al.* reported later the observation of non-mesonic decay of $^{31}_{\Lambda\Lambda}\text{Si}$ using 3.0 GeV/c K^- meson beam at CERN-PS [31]. The event was claimed to be regarded as the sequential decay of $^{31}_{\Lambda\Lambda}\text{Si} \rightarrow {}^{14}_{\Lambda}\text{C} + {}^{16}\text{O} + n$ followed by $^{14}_{\Lambda}\text{C} \rightarrow \alpha + 2t + d + p + n$. However, it was no longer referred to as a double-hypernucleus because the track of the Ξ^- hyperon was not observed and the K^+ meson track was not uniquely identified.

About ten years ago, a hybrid-emulsion experiment, E176, was carried out

at the KEK 12 GeV proton synchrotron. An event accompanied with sequential decay of a double-hypernucleus was found among about 80 Ξ^- hyperon captures at rest in nuclear emulsion. It has two interpretations for the species, $^{10}_{\Lambda\Lambda}$Be giving $\Delta B_{\Lambda\Lambda} = -4.9 \pm 0.7$ MeV, and $^{13}_{\Lambda\Lambda}$B leading to $\Delta B_{\Lambda\Lambda} = 4.9 \pm 0.7$ MeV [32, 33]. The event also remains the possibility of the decay to the single-hypernucleus in excited states. The E176 experiment also reported the productions of three heavy double-hypernuclei [34], but their nuclides could not be identified.

The production of $^{4}_{\Lambda\Lambda}$H hypernuclei was recently reported in a counter experiment, E906, at BNL, which detected two π^- mesons emitted from the sequential weak decays of double-hypernuclei using a cylindrical detector system [35]. But the statistics were limited and a value of $\Delta B_{\Lambda\Lambda}$ was not presented. Further confirmation is needed.

The value of $\Delta B_{\Lambda\Lambda} = 4 \sim 5$ MeV obtained from the three emulsion measurements illustrates the Λ-Λ interaction is attractive, while $\Delta B_{\Lambda\Lambda} = -4.9$ MeV presented by E176 indicates the repulsive Λ-Λ interaction. Moreover, two of the measurements remain the possibility of the decay to the single-hypernucleus in excited states. Hence, the Λ-Λ interaction energy $\Delta B_{\Lambda\Lambda}$ has not been determined uniquely yet.

The E176 reported two events of "twin hypernuclei", where two single-hypernuclei were produced simultaneously after the formation of a Ξ^- nucleus or a Ξ^- atom. Since the masses of some single-hypernuclei were already measured well, the binding energy of a Ξ^- hyperon in the Ξ^- nuclear or atomic state can be measured by the obserbation of a twin-hypernuclei event. The Information of the Ξ^--N interaction can be obtained from the measurements of B_{Ξ^-}. Both of the E176 events were interpreted most probablly as ^{12}C + Ξ^- $\rightarrow$ $^{9}_{\Lambda}$Be + $^{4}_{\Lambda}$H. The value of B_{Ξ^-} associated with the interpretation was obtained to be 0.54 ± 0.20 MeV from one of the events, named "Yokohama" event [36]. The other, called "Korea" event, gave $B_{\Xi^-} = 3.70 ^{+0.18}_{-0.19}$ MeV if both of the single-hypernuclei were in ground states, $B_{\Xi^-} = 0.62 ^{+0.18}_{-0.19}$ MeV if the $^{9}_{\Lambda}$Be was in an excited state, or $B_{\Xi^-} = 2.66 ^{+0.18}_{-0.19}$ MeV if the $^{4}_{\Lambda}$H was in an excited state [37].

There are eight reports of the production of the twin hypernuclei prior to the E176 experiment. One of them, presented by B. Bhowmik [38], remained the possibility of in-flight reaction of a Ξ^- hyperon. The other seven events [39] were all detected at the beam interaction vertices. Since such twin-hypernuclear emission can occur via a two-step process, $p(K^-, \pi^0)\Lambda$ followed by $p(\pi^0, K^+)\Lambda$ reaction, it is hardly said that each of them was the formation of a Ξ^- nucleus.

The Ξ^--N interaction was also studied by counter experiments using the (K^-, K^+) reactions. Excitation-energy spectra from the E885 experiment for the ^{12}C$(K^-, K^+)X$ reactions indicated the existence of Ξ^- hypernuclei and agreed with the theoretical calculation assuming the depth of the Ξ^--nucleus potential with the Woods-Saxon shape is 14 MeV or less [40]. Experimental data to obtain the Ξ^--N interaction is still scarce.

The E176 experiment searched for the short-lived H dibaryon ($\tau < 0.1$ ns) within $0.75 \times 0.75 \times 1.0$-mm^3 area arround Ξ^- hyperon capture points. They

found one candidate event of the $p\pi^-$ decay of a Λ hyperon emitted from a Ξ^- hyperon stopping point, but observed no candidate of the $H \rightarrow \Sigma^- p$ decay [41]. The H dibaryon was searched for in the E224 experiment at KEK-PS using a scintillating-fiber active target, but resulted in no yeild [42, 43]. The H dibaryon searches have been carried out in various experiments [44, 45], but evidence of its existence was not established yet.

On the other hand, the result of the observation of the double-hypernucleus by E176 gave the lower limit of the H mass to be $M(H) > 2203.7$ MeV/c^2 from the relation of eq. (1.5). There still remains the possibility of the H dibaryon being stable against the strong interaction.

1.3 KEK-PS E373 experiment

The E373 experiment has been carried out at the KEK 12 GeV proton synchrotron. It aimed to search for doubly strange nuclei, such as double-Λ nuclei, twin hypernuclei, and the H dibaryon, with ten times as high statistics as that in E176, by using an upgraded hybrid-emulsion technique.

In E373, we concentrated our attention on the production of double-hypernuclei, twin hypernuclei, and the H dibaryon via the nuclear Ξ^- hyperon capture process at rest. The Ξ^- hyperons were created via the (K^-, K^+) reactions in a diamond target, and brought to rest in emulsion. The positions and angles of the Ξ^- hyperons were measured with a scintillating-microfiber-bundle detector directly. Hyperfragments produced via the Ξ^- hyperon captures were observed in the emulsion, and particles emitted from the hyperfragments and escaping from the emulsion stack were detected by scintillating-fiber-block detectors. By combining emulsion and sintillating-fiber detectors, the thickness of a stack of emulsion was reduced to one-fifth of that for E176, and high statistics have been obtained with limited amount of nuclear emulsion.

Figure 1.2 illustrates the production process of doubly strange systems via the Ξ^- hyperon capture at rest. A Ξ^- hyperon is produced via the quasi-free $'p'(K^-, K^+)$ reaction and brought to rest in emulsion. A stopped Ξ^- hyperon is captured by an atom in emulsion. It is firstly captured to an atomic orbit in a highly excited level, and transferred into lower orbits emitting Auger electrons and X-rays. Finally it is absorbed by the nucleus, and then they form, with some probability, a double-hypernucleus, one or two singe-hypernuclei, or, if exists, the H dibaryon.

In the next chapter the procedure of the E373 experiment is described in detail. Chapter 3 provides the detailed description about the analysis of the spectrometer, the scintillating-fiber detectors, and the emulsion. An observed double-hypernucleus event is presented in Chapter 4. In Chapter 5, the weak decay modes of double-hypernuclei are discussed. Finally, this work is summarized in Chapter 6.
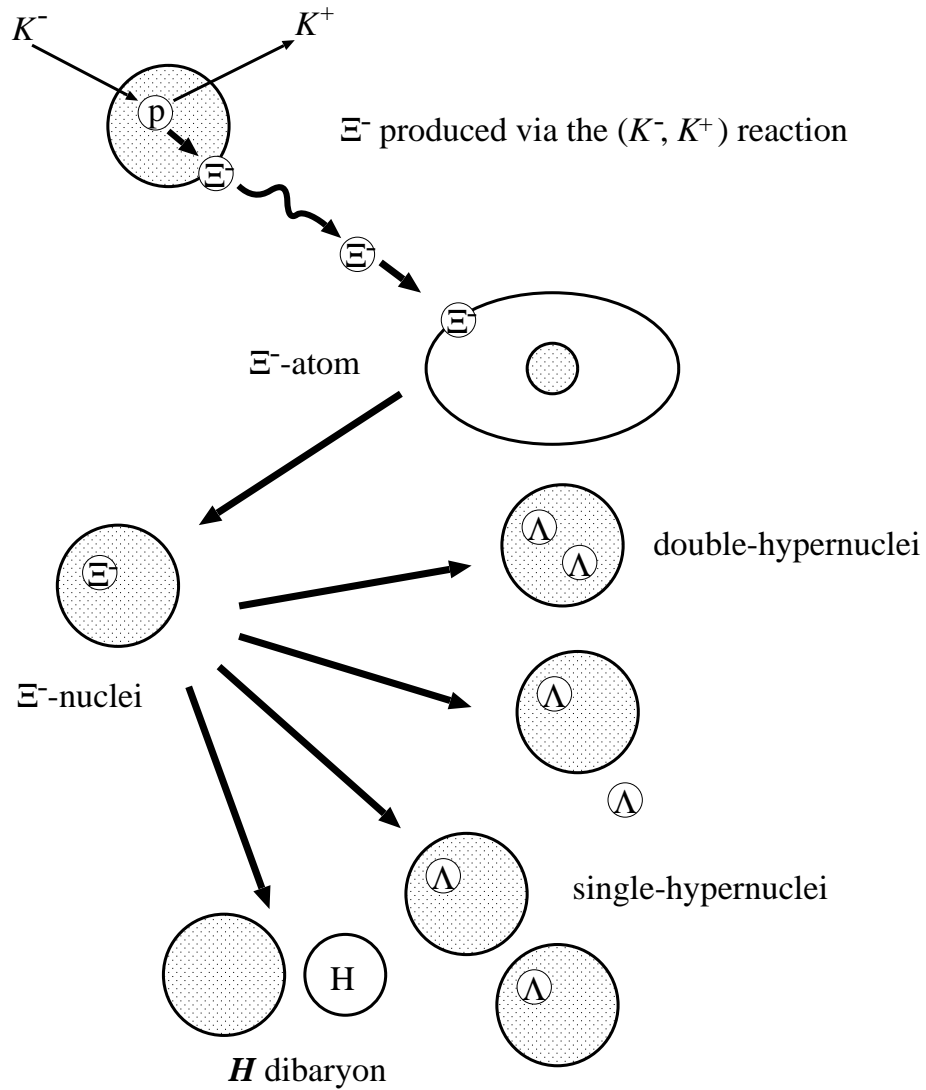
Figure 1.2: Production process of double-hypernuclei, twin hypernuclei, and the *H* dibaryon.

Chapter 2

Experimental Procedure

2.1 Overview

Figure 2.1 shows a schematic view of the target region of the E373 experiment. The Ξ^- particles, produced via the quasi-free $'p'(K^-, K^+)\Xi^-$ reactions in a diamond target, were slowed down in the target, and some of them came to rest in a nuclear emulsion. These (K^-, K^+) reactions were tagged using a magnetic spectrometer system (Fig. 2.2). The positions and directions of the Ξ^- particles were measured with a scintillating-microfiber-bundle detector (SciFi-Bundle), which is located between the diamond target and the nuclear emulsion. Hyperfragments emitted from the Ξ^- hyperon absorption points were observed in the emulsion. Particles emitted from the hyperfragment and escaping from the emulsion stack were detected by scintillating-fiber-block detectors (SciFi-Blocks), placed both upstream and downstream of the emulsion.

Figure 2.2 shows a magnetic spectrometer for measurements of the (K^-, K^+) reactions. The K^- beam spectrometer mainly consisted of a dipole magnet (D2), wire chambers (BPC1-5 and BDC1-3), aerogel Čerenkov counters (BAC1, 2), and plastic scintillators (T1 and T2). The aerogel Čerenkov counters were used in order to discriminate K^- mesons from e^-, μ^-, and π^- particles on line. In the off-line analysis, the particle identification was performed using the time-of-flight (TOF) of incident beam particles measured by the T1 and T2 counters. The K^+ tagging spectrometer was composed of a dipole magnet (KURAMA), wire chambers (DC1-3 and LST), aerogel Čerenkov counters (BVAC and FAC), and scintillator hodoscopes (VH, CH, YH, and FTOF). The momenta of scattered particles were analyzed by the KURAMA magnet, the wire chambers and the hodoscopes. Their velocities were obtained from the TOF measurements between the T2 counter and the FTOF wall. The two aerogel Čerenkov counters eliminated non-interacting beam particles and scattered pions.

The beam exposure of emulsion was carried out from February 1998 to July 2000. Totally 1.4×10^{10} K^- mesons were irradiated to the target, and data of 1.3×10^7 triggered events were acquired during the beam time.

In this thesis, z-coordinate is defined as the beam direction, and x- and y-

coordinates are horizontal and vertical direction, respectively, on the plane perpendicular to the beam direction. The directions of x and y rotated around the z-axis by 45 degrees are labeled as u- and v-coordinates, respectively (Fig. 2.3).

2.2 K^- beam

2.2.1   K2 beam line

The experiment was carried out at the KEK 12 GeV proton synchrotron K2 beam line. The primary protons were accelerated first in a Cockcroft-Walton to 750 keV and second in a linac to 40 MeV, and then injected into a booster. After the acceleration to 500 MeV in the booster, they were injected to a main ring and accelerated to 12 GeV. They were extracted slowly to the EP2 beam line in East Counter Hall during 2 sec in a 4-second cycle, and delivered to a production target of the K2 beam line. Figure 2.4 shows the layout of the K2 beam line. The beam line was designed aiming to provide mainly separated kaon beam with the momentum range from 1.0 GeV/c to 2.0 GeV/c [46]. The secondary beam was produced by the 12 GeV primary protons on a production target made of platinum with the dimension of 6-mm wide, 3-mm thick, and 60-mm long. The production angle at the primary target was 0°. The secondary beam particles were analyzed and focused by two dipole (D1 and D2), six quadrupole (Q1 - Q4, Q6 and Q7), and a sextapole (SX) magnets. The species of the incident particles were separated by an electrostatic separator (SEP) of length 6 m, together with a pair of correction magnets (CM). The voltage of 600 kV was applied between the positive and the negative electrode. The gap of the electrodes was 10 cm and filled with a mixture of Ne (64 %) and He (36 %) gases with the pressure of 2×10^{-4} Torr typically.

The beam size (r.m.s.) near the focal point (measured with the multi-wire chamber, BPC5, located upstream of the target) was 4.1 mm in horizontal and 5.3 mm in vertical.

For emulsion experiments, the statistics strongly depends on the amount of emulsion, because the irradiatable track density in emulsion is limited to keep the transparency of the emulsion plate after the development. Therefore the purity of K^- beam is critical for our experiment. In order to cut off the beam halo, the 600-mm-long collimator made of tungsten-alloy blocks and iron plates was installed just downstream of the Q7 magnet. The gap was 20-mm high and had a trapezoid shape to fit the beam focusing, as shown in Fig. 2.5. Although the cross section of the (K^-, K^+) reaction is maximum at 1.8 GeV/c [47], the K/π ratio of the beam becomes worse at higher momentum. Therefore, the beam momentum was set to 1.66 GeV/c. The ratio of incident K^- mesons to all charged beam particles was typically 25 % during the beam exposure. Typical K^- beam intensity was 1.1×10^4 /spill with the intensity of 2.0×10^{12} primary protons in '98 run, and 1.3×10^4 /spill with 2.4×10^{12} protons in '99 and 2000 runs.

2.2.2 Trigger counters and wire chambers

Two scintillation counters (T1 and T2) were used for the measurement of the time-of-flight (TOF) of incident beam particles. Each of them consisted of a plastic scintillator (Bicron BC418) of 5 mm in thickness, both horizontal ends of which were contacted to photo-multipliers (PMTs), HAMAMATSU H2431-50. The sizes of the scintillators were 100 mm (horizontal) × 50 mm (vertical) for the T1, and 50 mm × 50 mm for the T2 counter. The T1 counter was located upstream of the D2 magnet and the T2 placed upstream of the diamond target. The distance between the T1 and the T2 was 674 cm. Typical TOF resolution was 75 ps (r.m.s.) after the timing correction using the ADC informations.

   Another scintillation counter, TgtDef (Target Defining counter), was installed just upstream of the diamond target for tagging beam particles incident to the target. It consisted of a 3-mm-thick plastic scintillator, Bicron BC-404, of 20 × 20-mm^2 area, and coupled to a HAMAMATSU H3171-03 PMT via a 157.5-mm-long acrylic light guide. The PMT was surrounded by a 2.8-mm-thick iron shield against the magnetic field.

   For the on-line identification of beam particles, two aerogel Čerenkov counters (BAC1 and BAC2) were placed between the beam collimator and the T2 counter. A schematic view and a photograph of the BAC counters are shown in Fig. 2.6. Each of them consisted of a hydrophobic-silica-aerogel block [48], with the size of 10 cm (horizontal) × 7 cm (vertical) × 3 cm (longitudinal) for the BAC1, and the size of 8 cm × 8 cm × 3 cm for the BAC2. They were used to distinguish K^- mesons from the other contamination in the beam. The index of the aerogel is 1.03, which corresponds to the threshold velocity of $\beta = 0.971$ for Čerenkov radiation. In order to avoid overkilling K^- mesons because of knock-out electrons, we used the coincidence signal of the two BAC counters. By taking the coincidence of the two BAC's, the detection efficiency for 1.66 GeV/c pions ($\beta = 0.997$) was 99.8 %, while the efficiency for 1.66 GeV/c kaons ($\beta = 0.959$) was 0.25 %.

   For tracking incident particles and monitoring beam profile, we have used five multi-wire proportional chambers (BPC1 - BPC5) and three multi-wire drift chambers (BDC1 - BDC3). The BPC1, BDC1, BPC2, and BDC2 were placed upstream of the D2 magnet in that order. The BDC3, BPC3, and BPC4 were located just downstream of the D2, the Q7 magnet, and the collimator, respectively. The BPC5 was positioned between the T2 counter and the diamond target. Their specifications are summarized in Table 2.1 and 2.2.

2.3 K^+ spectrometer

2.3.1 Spectrometer magnet

For analyzing the momenta of outgoing particles, we used a large acceptance spectrometer magnet, "KURAMA". The size of the gap is 50-cm high, 100-cm wide, and 80-cm long. It was operated with the central magnetic field of about 1
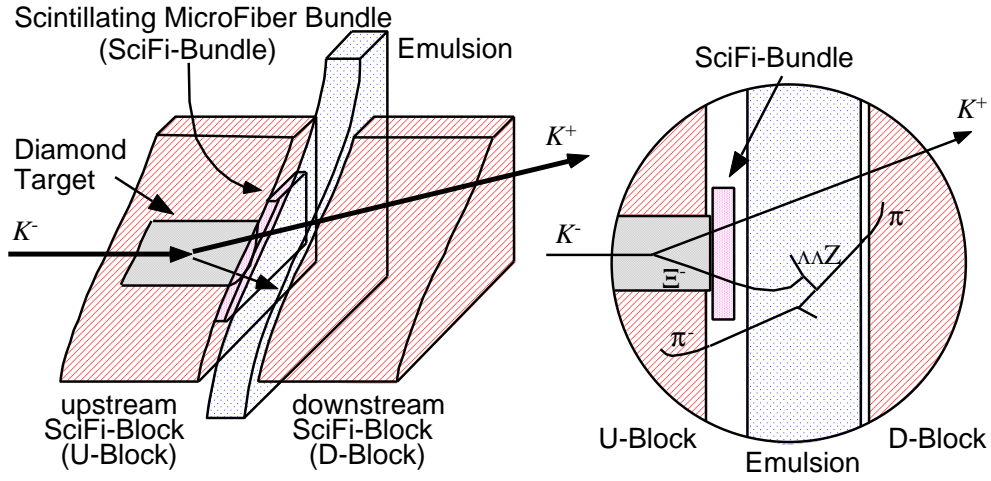
Figure 2.1: Schematic view of the experimental setup.

Table 2.1: Specifications of the BPCs.

anode wire spacing	1 mm
anode wire diameter	10 μm
anode wire material	Au-plated W
cathode material	graphite
operation voltage	4 kV
gas mixture	Ar 73%, Isobutane 23%, Freon 1%, Methylal 3%
active area	
BPC1	112 mm (x) × 64 mm (y)
BPC2	112 mm (x)
BPC3	112 mm (x) × 64 mm (y)
BPC4	112 mm (x) × 64 mm (y)
BPC5	80 mm (x) × 64 mm (y)

Table 2.2: Specifications of BDCs.

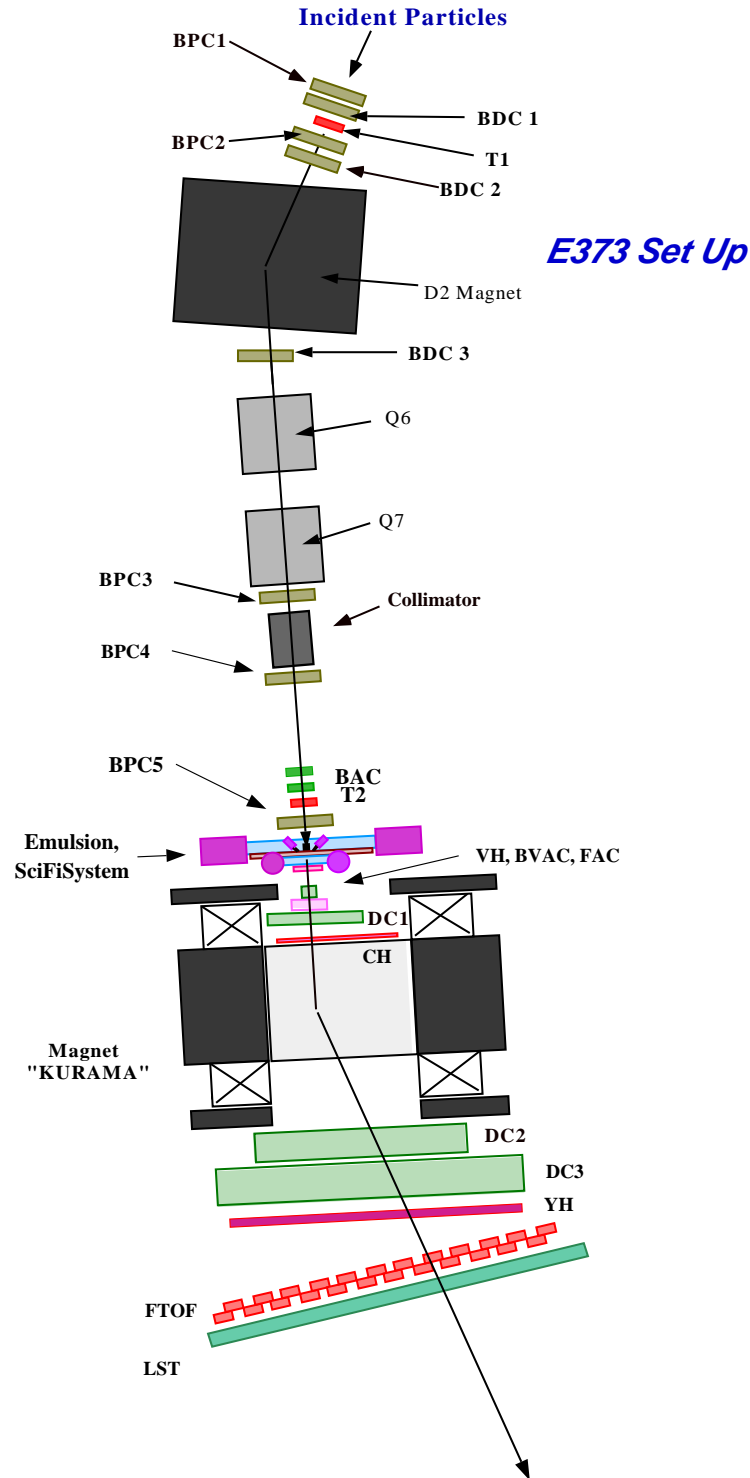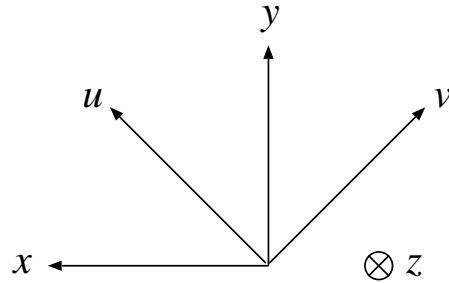|	
sense wire spacing	5 mm
sense wire diameter	10 μm
sense wire material	Au-plated W
potential wire voltage	1.5 kV
cathode plane voltage	1.45 kV
gas mixture	Ar 80%, Isobutane 20%
active area	160 mm $(x$ and $x')$

Figure 2.2: Layout of E373 spectrometer.

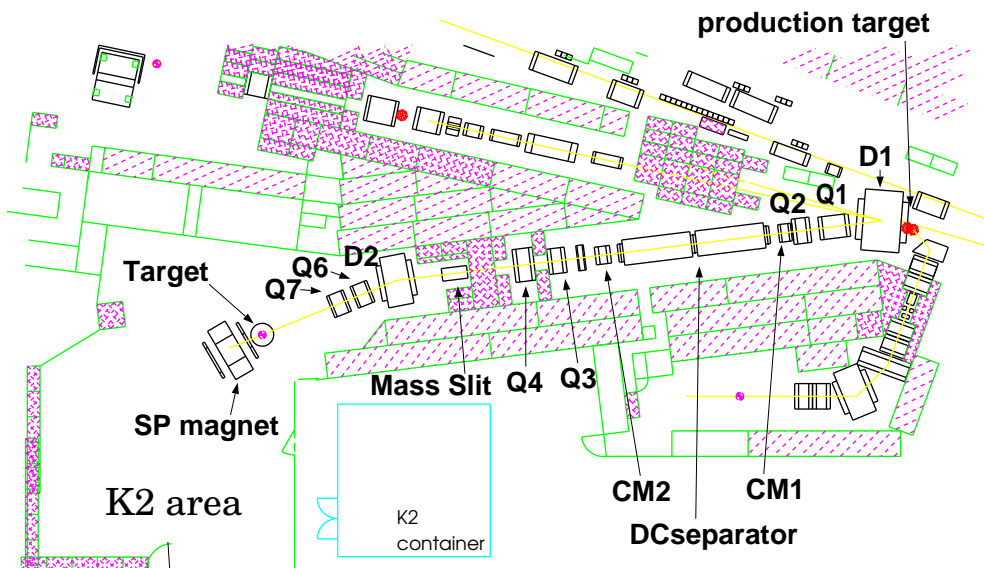Figure 2.3: Definition of the coordinate system.

Figure 2.4: Layout of the K2 beam line at KEK 12 GeV proton synchrotron.
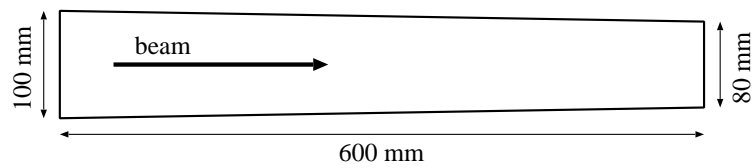

Figure 2.5: Horizontal dimension of the beam collimator window. The gap is 20 mm in vertical.
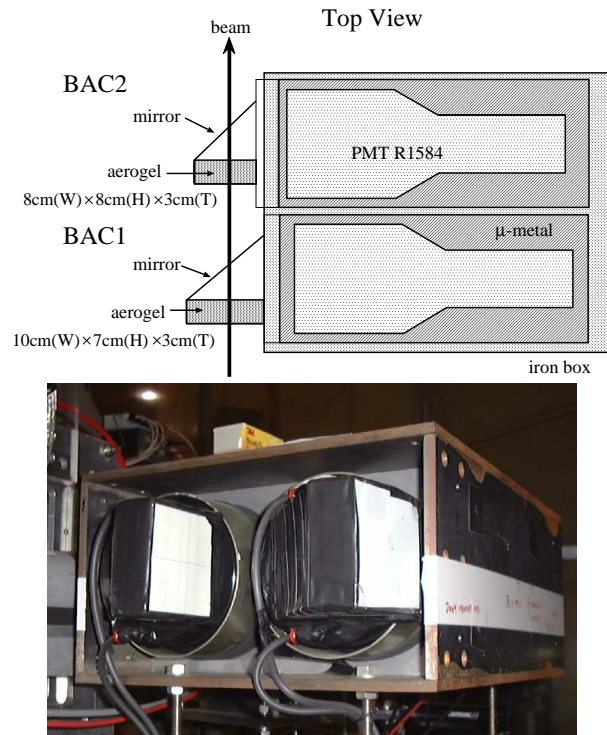
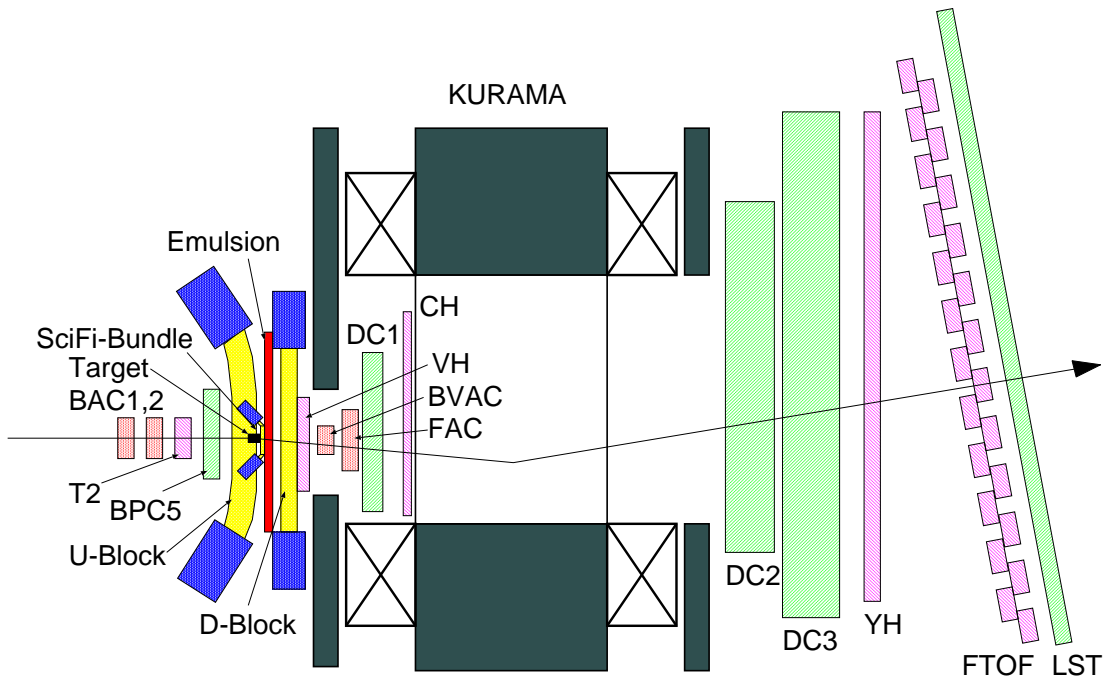Figure 2.6: Schematic drawing and photograph of the BAC counters.

Figure 2.7: Layout of the K^+ tagging spectrometer.
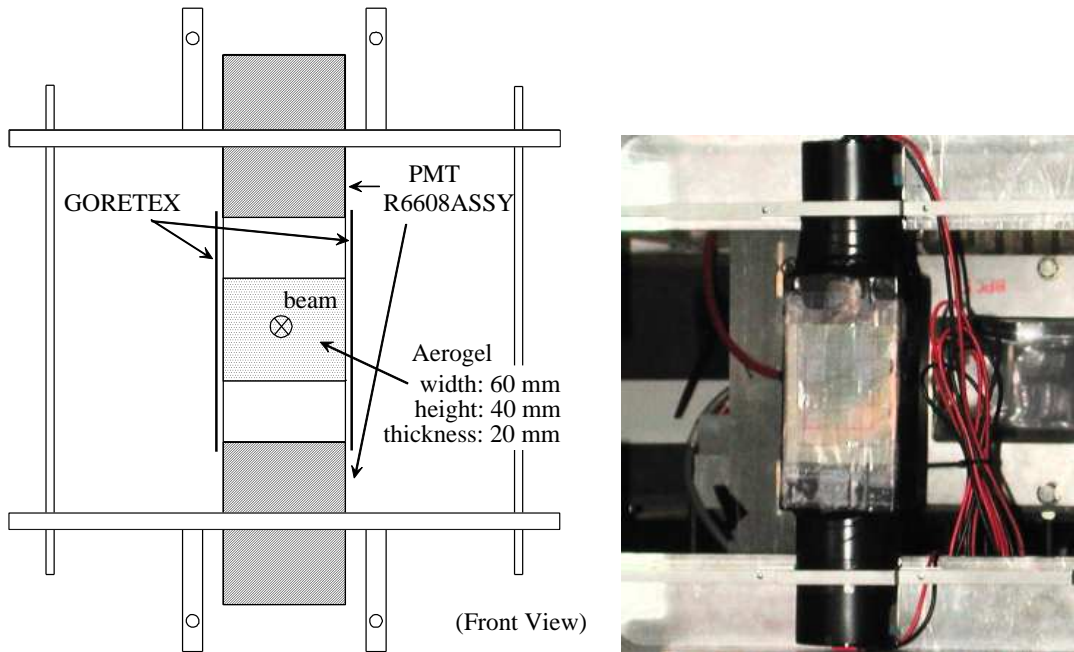
Figure 2.8: Schematic drawing and photograph of the BVAC detector.

Tesla. The acceptance of the spectrometer was 0.17 str.

2.3.2 Aerogel Čerenkov counters

In order to maximize the yield of stopping Ξ^- hyperons, it is very important to detect low-momentum Ξ^- hyperons accompanied with the K^+ mesons scattered forward. In order not to kill such forward-scattered K^+ mesons, an aerogel Čerenkov counter (BVAC) was used to veto non-interacting beam particles. Figure 2.8 shows a schematic drawing and a photograph of the BVAC counter. It was located inside of the aperture of the front end-guard of the KURAMA magnet. The Čerenkov light from the aerogel block was read from top-side and bottom-side PMTs (HAMAMATSU R6608ASSY), which are fine-mesh type for the operation in strong magnetic field, and have UV-transparent input windows. The dimension of the silica-aerogel block is 60-mm wide, 40-mm high, and 20-mm thick. Its refractive index of 1.05, corresponding Čerenkov threshold velocity of $\beta = 0.952$, enables 1.66 GeV/c kaons ($\beta = 0.959$) to emit Čerenkov light, and does not enable those with the momenta less than 1.4 GeV/c ($\beta < 0.943$). Since the momenta of scattered K^+ mesons are less than 1.4 GeV/c, the BVAC can discriminate K^+ mesons in interest from non-interacting K^- mesons. The detection efficiencies for 1.66 GeV/c and 1.2 GeV/c kaons were 97 % and 13 %, respectively.

In order to identify the outgoing particles on line, another aerogel Čerenkov counter (FAC) was placed just downstream of the front end-guard of the KURAMA. The schematic view of the FAC is shown in Fig. 2.9. The size of the

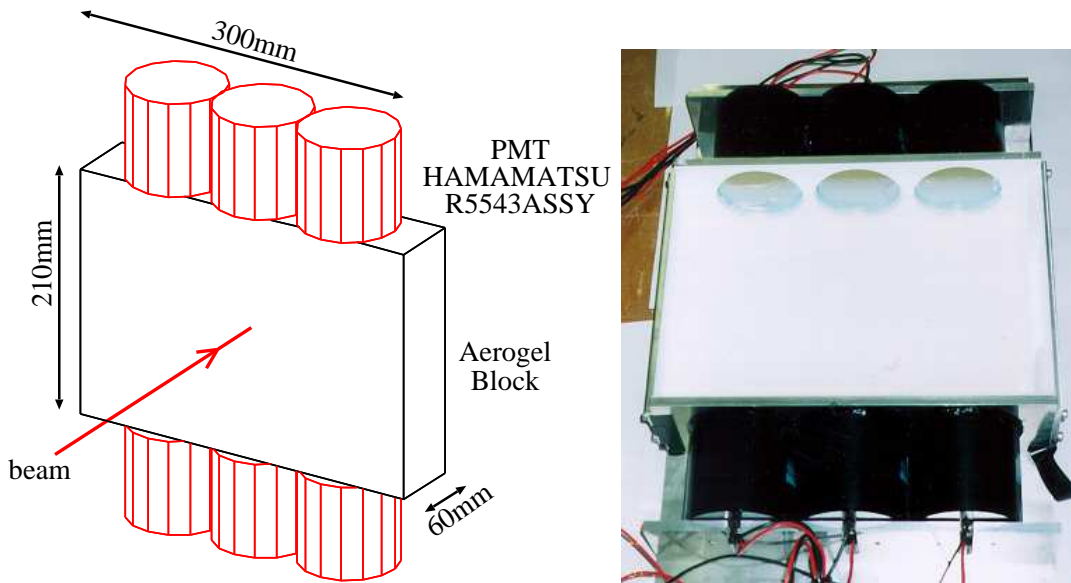Figure 2.9: Schematic drawing and photograph of the FAC counter.

aerogel block is 300 mm in width, 210 mm in height, and 60 mm in thickness. It was viewed by six fine-mesh-type PMTs, HAMAMATSU R5543ASSY, from top and bottom ends. The refractive index is 1.041 and the corresponding Čerenkov β-threshold is 0.962. For the region of momenta from 0.8 GeV/c to 1.4 GeV/c, the efficiency for pions was more than 98 %, while that for kaons was about 8 %.

2.3.3   Scintillator hodoscopes and wire chambers

Four sets of plastic scintillator hodoscopes (VH, CH, YH, and FTOF), three drift chambers (DC1 - DC3), and a limited-streamer-tube detector (LST) were installed for tracking the outgoing particles and the on-line trigger.

Table 2.3 summarizes the specifications of the hodoscopes. All scintillators were coupled to PMTs via lucite light-guides. The VH (Vertex Hodoscope) and CH (Charge Hodoscope) were located just upstream of the front end-guard and the pole pieces, respectively, of the KURAMA magnet. The YH (Y Hodoscope) were placed downstream of the DC3 in order to kill triggers caused by neutral particles hitting the thick FTOF scintillators. The signals of the scintillators were read from both horizontal ends connected to PMTs via lucite light-guides. The FTOF (Forward TOF counter) array was placed downstream of the YH, 3.1 m away from the T2 counter. Two PMTs were coupled to top and bottom ends of each scintillator via lucite light-guides. The TOF information between the T2 and the FTOF was used to measure the velocities of outgoing particles. The average TOF resolution was 130 ps (r.m.s.) in typical after the timing correction using the ADC informations.

The DC1 chamber was placed between the FAC and the CH counters, and the

Table 2.3: Specifications of the plastic scintillator hodoscopes. All PMTs are HAMAMATSU and all scintillators are KURARAY.

	VH		CH	YH	FTOF
array direction	x	y	x	y	x
# of channels	32	18	24	6	24
thickness [mm]	2	2	2	5	30
width [mm]	6.6	9.0	19	200	80
spacing [mm]	4.4	6.0	17.5	180	75
PMT type	R5600U	R3164-10	H3165-01	H1161	H1949
scintillator type	SCSN-50	SCSN-50	SCSN-50	SCSN-56	SCSN-56
effective area [mm(x)×mm(y)]	143×110		421.5×300	1700×1100	1805×1200

DC2 and DC3 were located downstream of the KURAMA magnet. Specifications of the DCs are summarized in Table 2.4. Detailed description is given in Ref. [49].

The LST detector was installed downstream of the FTOF, most downstream of the E373 spectrometer system. It consisted of two arrays of fifteen plastic tubes and two layers of cathode strip. Each of the tube has a characteristic structure as shown in Fig. 2.10 and Fig. 2.11. The high voltage of 5 kV was supplied to the anode wires. When a charged particle passes through the tube, electronic avalanche occurs around the anode wire, and induces charge on cathode strips. By reading the induced signal on cathode strips, the LST measures the horizontal position of the passing charged particle. The r.m.s. position resolution was about 4 mm. Specification of the LST is summarized in Table 2.5. More details about the LST is described in Ref. [50].

2.4   Diamond target

The diamond target was placed in the center hole of the upstream scintillating-fiber-block detector, which is the final focusing point of the beam line. It was composed of $1 \times 1 \times 0.1$-cm^3 wafers of industrial diamonds, which are made by a chemical-vapor-deposition (CVD) process, stacked and epoxied together [51]. The total dimension of the diamond target was 2×2-cm^2 area and 3-cm long. Its density of 3.34 g/cm^3 is about 95 % of that of pure diamond crystal (3.51 g/cm^3). The photograph of the diamond target is shown in Fig. 2.12.

The diamond target was used to produce Ξ^- hyperons via the quasi-free $'p'(K^-, K^+)\Xi^-$ reactions. The forward-angle cross section of the (K^-, K^+) re-action was measured to be proportional to $A^{0.38}$ in the K^+ momentum region of Ξ^- hyperon production being dominant [52]. It was also the function of the

Table 2.4: Specifications of the DCs. As for the DC1 u plane, the wires were tilted by 30 degrees from the vertical direction.

chamber	DC1			DC2		DC3	
plane	x, x'	y	u	x, x'	y, y'	x, x'	y, y'
sense wire spacing (mm)	10.0			9.0		56.0	60.0
sense wire voltage (kV)	-					+1.00	
sense wire diameter (μm)	20.0						
sense wire material	Au-plated W						
potential wire voltage (kV)	-1.85			-2.10		-3.00	
potential wire diameter (μm)	75			200		150	
potential wire material	Au plated Cu-Be			Al		Au plated Cu-Be	
number of channel	48	32	40	128	96	32	16
active area (x mm $\times$ y mm)	500×350			1200×1200		1800×900	
gas mixture	Ar 50%, C_2H_6 50%						

Figure 2.10: Cross-sectional view of the LST.
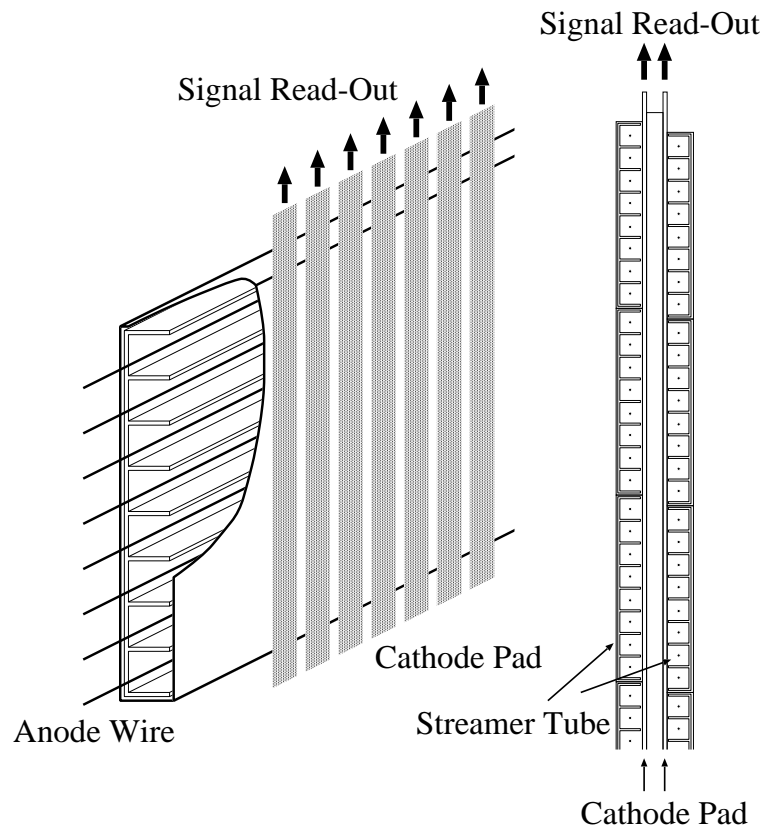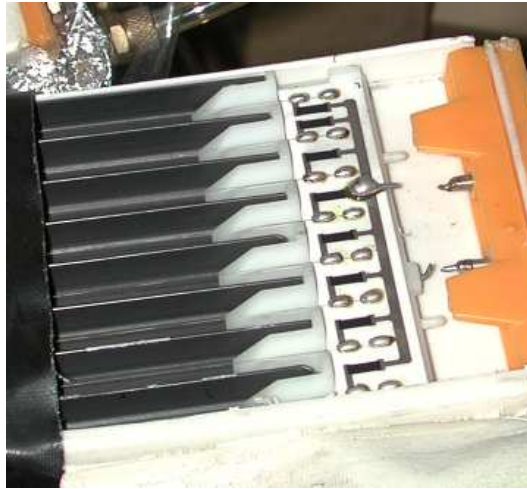
Figure 2.11: Photograph of the inside of the LST.

Table 2.5: Specification of the LST.

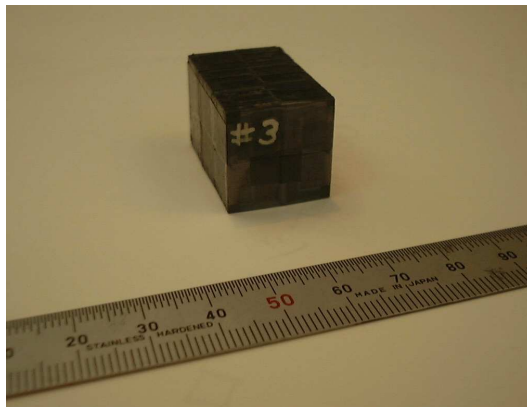| anode wire spacing	1 cm
anode wire diameter	100 μm
anode wire voltage	$\sim$ 5 kV
cathode strip width	4 mm
cathode strip spacing	6 mm
cathode strip material	Al
gas mixture	Ar 25%, Isobutane 75%

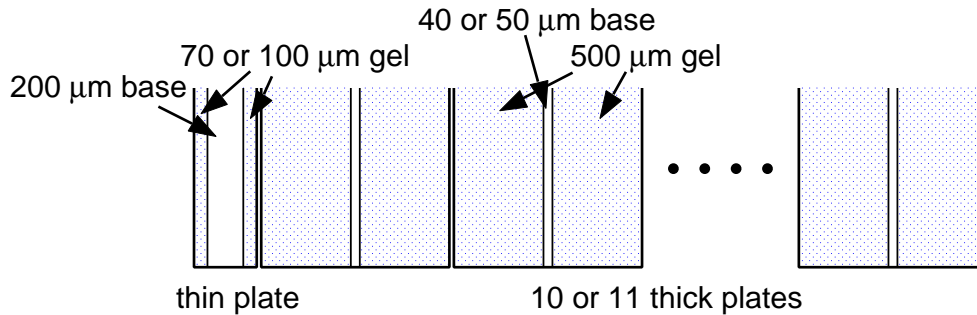Figure 2.12: Photograph of the diamond target.

Figure 2.13: Constitution of an emulsion stack.

diamond block to degrade the kinetic energies of the Ξ^- hyperons efficiently in order to bring them to rest in the emulsion stack. The material with a small mass number and a high density is, therefore, suitable for yielding a large number of Ξ^- hyperon stopping events.

2.5 Nuclear emulsion

An emulsion stack consisted of eleven (for first ten stacks) or twelve (for the others) plates with 24.5×25.0-cm^2 area. Figure 2.13 illustrates the constitution of a stack of emulsion. Since the most upstream plate was used to connect Ξ^- hyperon tracks from the SciFi-Bundle detector, it was necessary to minimize the distortion of the emulsion gel of the plate. For this reason, a thin emulsion plate was located upstream followed by ten or eleven thick emulsion plates [53]. The thin plate had 70-μm-thick or 100-μm-thick emulsion gel on both sides of a 200-μm-thick plastic base film, and each thick plate had 500-μm-thick emulsion gel on both sides of a 40-μm-thick or 50-μm-thick plastic film.

The emulsion gel was Fuji ET-7C and Fuji ET-7D, which were developed by Fuji-film, Gifu University, and Nagoya University. The deviation of the sizes of AgBrI crystals in the ET-7C emulsion is smaller than that in the ET-7B type used in the E176 experiment, and that in the ET-7D is smaller than that in the ET-7C. The composition of the emulsion gel is listed in Table 2.6. Thin acrylic and polystyrene films were utilized for the plate bases, and the methods to glue the emulsion gel and the base film were newly established. The details of the base film handling are given in Ref. [54].

All emulsion plates were prepared in Gifu University with the following procedure. First, emulsion gel was poured to one side of the plastic films. They were dried in a drying cabinet which moved emulsion plates automatically so that they were dried uniformly. In order to minimize the distortion of the emulsion gel during the drying process, "dummy gel" made of colloidal silica was poured around the emulsion gel. After drying the emulsion gel, gel was poured to the other side of the plates and dried in the same manner. Then, the emulsion plates were dried

Table 2.6: The composition of the Fuji ET-7C and ET-7D emulsion.

material	weight ratio (%)	mol ratio (%)
I	0.3	0.06
Ag	45.4	11.2
Br	33.4	11.1
S	0.2	0.2
O	6.8	11.3
N	3.1	5.9
C	9.3	20.6
H	1.5	40.0

Table 2.7: Type of the emulsion gel and material of the base film. The lengths indicated in the parentheses are the thickness of the base films or that of the gel of each side of the film.

run cycle		1998	1999	2000	
stack#		#1 - #45	#46 - #50	#51 - #63	#64 - #100
thin type	gel	ET-7C ($70~\mu$m)	ET-7C ($70~\mu$m)	ET-7D ($100~\mu$m)	ET-7D ($100~\mu$m)
	base	acrylic ($200~\mu$m)	polystyrene ($200~\mu$m)	polystyrene ($200~\mu$m)	polystyrene ($200~\mu$m)
thick type	gel	ET-7C ($500~\mu$m)	ET-7C ($500~\mu$m)	ET-7C ($500~\mu$m)	ET-7D ($500~\mu$m)
	base	acrylic ($50~\mu$m)	polystyrene ($40~\mu$m)	polystyrene ($40~\mu$m)	polystyrene ($40~\mu$m)

again with lower humidity. Each of the emulsion plates was divided to four plates with the size of 24.5×25.0 cm^2. The type of the emulsion gel and the material of the base film used in each run cycle are summarized in Table 2.7.

A stack of emulsion was packed in a stainless vacuum chamber cassette to keep the flatness and the relative positions between the emulsion plates during the beam exposure, and to save time for the installation and uninstallation of the emulsion stacks. Figure 2.14 presents the photograph and the schematic drawing of the emulsion cassette. It was sealed with a 150-μm-thick stainless foil upstream and a 1-mm-thick black rubber plate downstream.

In order to apply the K^- beam to the whole area of the emulsion with a uniform track density (1×10^6 tracks/cm^2), the emulsion stack was moved during the exposure by the emulsion mover (Fig. 2.15). The emulsion mover drove the emulsion stack by the length proportional to the beam intensity of each spill,
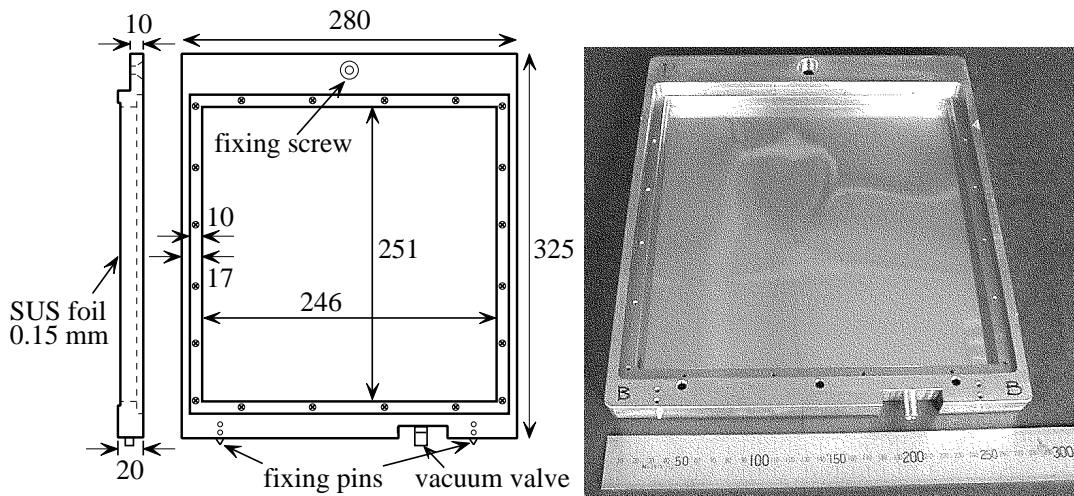
Figure 2.14: Photograph and schematic drawing of the emulsion cassette.

during the 2 seconds intervals between two spills. The emulsion stack was driven in the 22×22-cm^2 area in the following manner. First, the emulsion moved horizontally by the length depending on the beam intensity. After whole the horizontal movement of 220 mm, the stack was shifted vertically by 2 mm, and then, moved horizontally in the opposite direction. The emulsion mover was controlled by a personal computer equipped with control boards and operated by the Windows95 operating system. The position of the emulsion stack was measured with a HEIDENHEIN linear encoder in horizontal and a SONY magne scale in vertical. Their accuracies were less than 10 μm. The cassette shipping a stack of emulsion was fixed to the mover with two pins on the bottom and one screw on the top. Details of the emulsion mover are described in Ref. [55].

2.6 Scintillating-fiber detectors

We have used a scintillating-microfiber-bundle detector and two scintillating-monofiber-block detectors. Scintillation light from each detector was amplified with a chain of image-intensifier tubes (IITs) without losing the two-dimensional position information, and read by a charge-coupled device (CCD).

2.6.1 Scintillating-microfiber-bundle detector

A scintillating-microfiber-bundle detector (SciFi-Bundle) was placed between the diamond target and the emulsion chamber, in order to measure the positions and angles at entrance of Ξ^- hyperons, created via the (K^-, K^+) reaction, to the emulsion stack. Details of the SciFi-Bundle detector are presented in Ref. [56].

Each bundle consisted of scintillating micro-fiber of 45 μm$^\phi$ in diameter. The core of the micro-fiber was made of polystyrene doped with the wave-length shifter
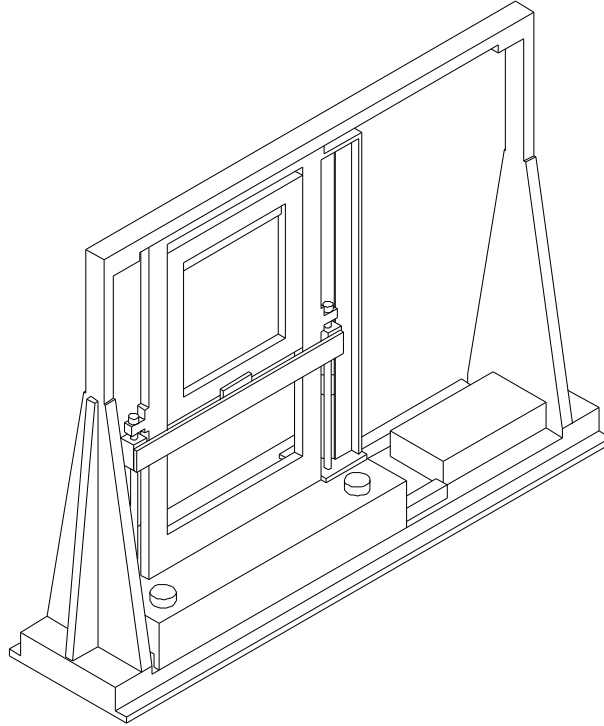
Figure 2.15: Schematic view of the emulsion mover.

Table 2.8: Specifications of the SciFi-Bundle detectors.

run	'98 and '99	2000
bundle size [mm×mm]	0.7×0.7	1.0×1.0
sheet width [mm]	42	40
number of division	5	4

of PMP (1-phenyl-3-mesityl-2-pyrazoline) with the density of 2.0 wt%. It was surrounded by two claddings; inner layer was made of polymethylmethacrylate (PMMA) outer layer fluorinated polymethacrylate with an index of 1.42.

The size of each bundle was 0.7×0.7 mm^2 in '98 and '99 runs, and 1.0×1.0 mm^2 in 2000 run. Four sheets of the bundles of 42 mm or 40 mm in width were piled up with the direction of u and v alternately (Fig. 2.16). In order to utilize the full aperture of the IIT, each sheet was divided into five or four partial sheets, and they were stacked at the input of each IIT. The dimensions of the bundle and the sheet in each run cycle are summarized in Table 2.8.

0.7 mm
or 1.0 mm

sheets (*u,v,u',v'*)

Emulsion Mover

beam

IIT

200mm

front view   side view

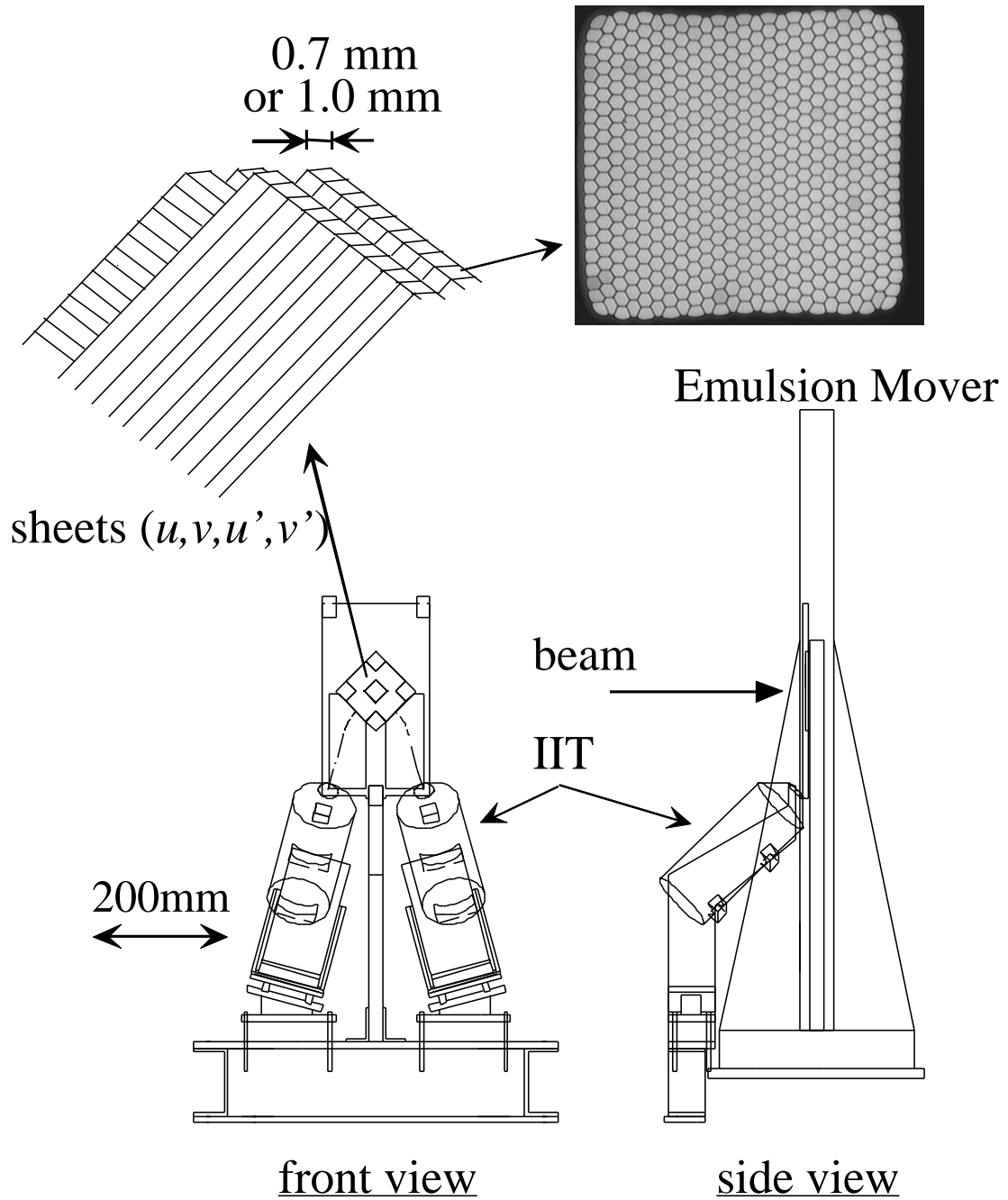Figure 2.16: Layout of the SciFi-Bindle detector. The upside photograph shows the end view of a 1-mm square fiber bundle. The diameter of one fiber is 45 μm.

2.6.2 Scintillating-fiber-block detectors

In order to obtain high statistics with limited amount of nuclear emulsion, the thickness of the emulsion stack has been reduced to about one-fifth of that for E176. For this reason, pions and protons emitted from the weak decays of hypernuclei may not be stopped in the emulsion. It is very important, however, to measure the energy of such particles in identification of the nuclide and in determination of the mass of the double-hypernucleus and the Λ-Λ interaction. Therefore, we used scintillating-fiber-block detectors (SciFi-Blocks) as a range counter for pions and protons. Two SciFi-Blocks were installed; an upstream block (U-Block) was located upstream of the SciFi-Bundle and a downstream block (D-Block) was placed downstream of the emulsion chamber. It was also their purposes to detect Λ hyperons or the H-dibaryon emitted from the stopping points of Ξ^- hyperons or (K^-, K^+) reaction vertices by observing their decays. In addition, they were used for event selection to reduce the number of events to be analyzed in the emulsion, which needs huge amount of time. For example, the event in which a Ξ^- hyperon decayed before stopping in the emulsion was rejected by the human eye scanning.

We have used 0.5 mm $\times$ 0.5 mm square fibers (KURARAY SCSF-78). The core was made of polystyrene with a refractive index of 1.59 and a density of 1.06 g/cm^3. It was surrounded by a 10-μm-thick cladding made of polymethyl-methacrylate (PMMA) with an index of 1.49 and a density of 1.18 g/cm^3. The attenuation length was measured with a radioactive source of β-rays [57]. The number of fibers per one sheet was 144 for the U-Block and 120 for the D-Block. The U-Block consisted of 98 fiber sheets and the D-Block 90 fiber sheets.

The structure of the U-Block is shown in Fig. 2.17. There is a square hole (20 mm $\times$ 20 mm) in the center of the U-Block in order to insert the diamond target and to pass the beam through. For this reason, it has a very complicated structure. To make the hole without making unreadable dead spaces, one sheet was divided into two partial sheets. One was extended to the left-side IIT and the other to the right-side IIT. The partial sheets from the u- and v-direction were piled up by turns at the input window of each IIT chain (Fig. 2.19 (a)). Therefore, two images of uz- and vz-plane were read out as one overlapped image. It is thus necessary to identify hit position of each sheet and reconstruct the original two images. At the readout-end of the fiber sheets, 0.3-mm-thick black vinyl chloride sheets were inserted between fiber sheets to identify each sheet easily. At the detection area, 0.3-mm-thick Al degraders were inserted between fiber sheets in order to increase the acceptance of the block as a range counter. In order to increase the number of detected photoelectrons, one side of each fiber sheet for the U-Block which is opposite to the readout-end was polished and evaporated with aluminum to reflect the photons. The effect of this mirror was studied by measuring the yield of scintillation light induced by the passage of β-rays. It was found that the light yield was increased by 1.6 times with the mirror.

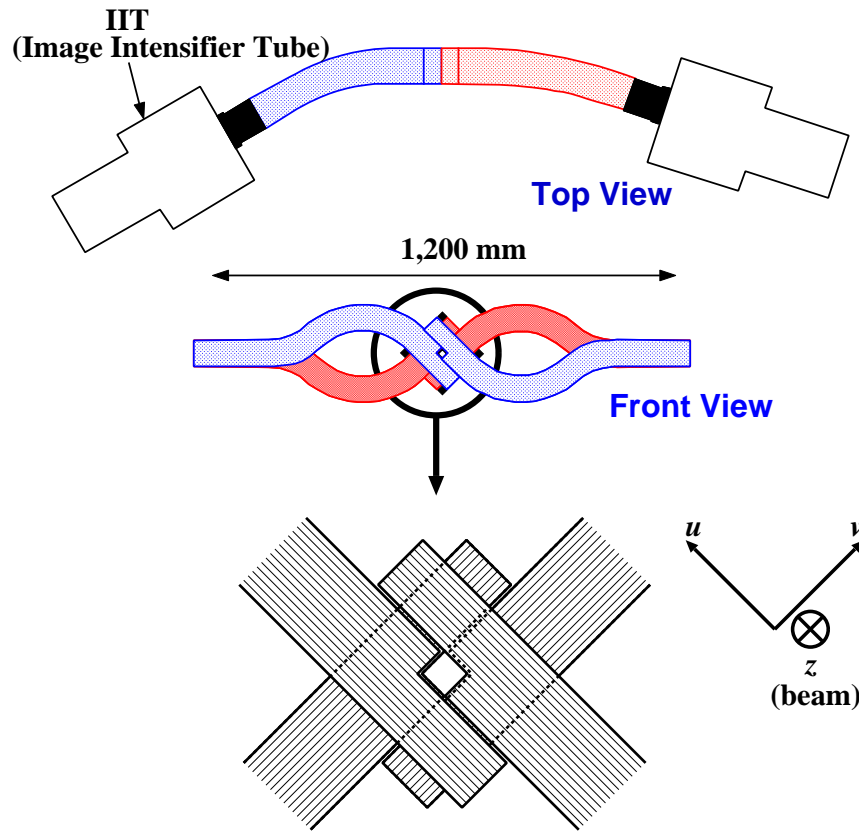The structure of the D-Block is shown in Fig. 2.18. In order to utilize the

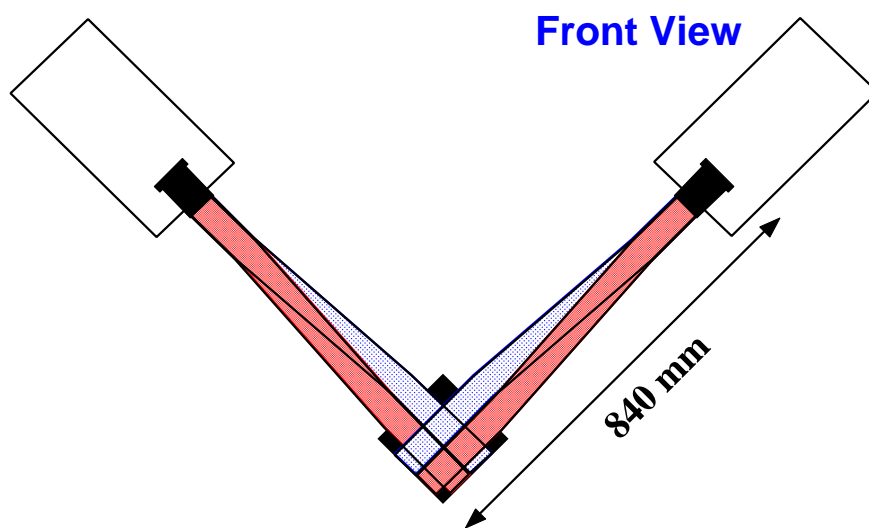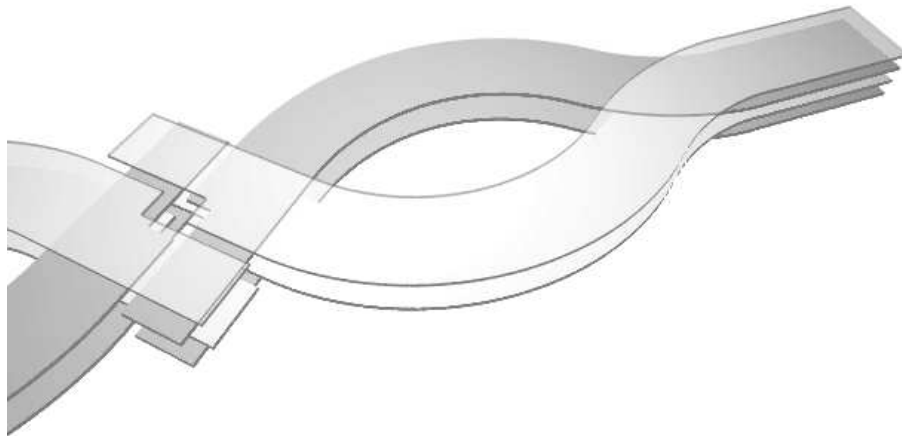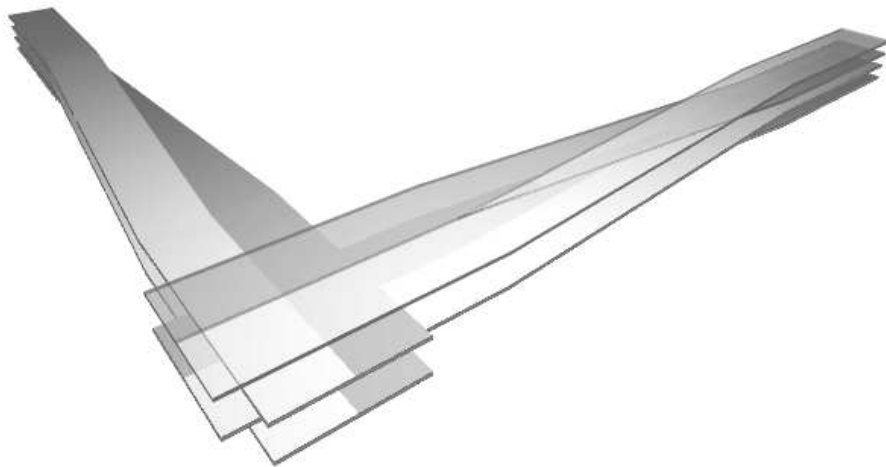Figure 2.17: Schematic view of the U-Block.

Figure 2.18: Schematic view of the D-Block.

(a) U-Block

(b) D-Block

Figure 2.19: Basic structure of (a) the U-Block and (b) the D-Block. In the U-Block, u sheets and v sheets were piled up alternately. In the D-Block, each sheet was divided into upper and lower parts and they were stacked by turns.

full aperture of the IIT, each sheet was divided into two partial sheets, and they were piled up alternately at the input of each IIT (Fig. 2.19 (b)). Hence, images of upper part and lower part were overlapped to each other. Black vinyl chloride sheets of 0.2 mm in thickness and Al degraders of 0.3 mm were inserted at the readout-end of the fiber sheets and at the detection area, respectively, like the U-Block. Black acrylic plates evaporated with aluminum were attached as mirrors to the end of the block opposite to the readout-end.

2.6.3 Image-intensifier tubes

The IIT chains of the SciFi-Bundle consisted of three image-intensifier tubes and a CCD, as shown in Fig. 2.20 (a). The input window of the first-stage IIT is 18 mm$^\phi$ in diameter. Each IIT stage had approximately no magnification factor. A tapered-optical-fiber plate with a magnification of 11/18 was inserted between the third-stage IIT and the CCD chip. The CCD chips (Sony XC-77RR) have 768 × 493 pixels, where the size of each pixel is 11 μm × 13 μm. The first stage of the IIT chain was the electrostatically focusing type (DEP PP0010U). The second and third are the Micro Channel Plate (MCP) type (DEP XX1450HJ and DEP XX1700AB, respectively). Each MCP-type IIT is gatable by applying voltage between the photo-cathode and the MCP. As mentioned later, the gate of the second stage was opened with the first-level trigger, while the third stage gate with the second-level trigger. The type of phosphor of each stage was determined so that it could keep the image during the decision time of the triggers. The phosphor of the first, second, and third stages were P24, P20, and P20, respectively. The mean decay time of the P24 phosphor is about 2.4 μs, and that of the P20 about 50 μs.

Each IIT chain of the U-Block composed of four image-intensifier tubes and a CCD (Fig. 2.20 (b)). The input window of the first-stage IIT is 100 mm$^\phi$ in diameter. The first-stage IIT had a magnification factor of 25/100 and the other stages had a magnification of 1. A tapered-optical-fiber plate with a magnification of 7/25 was inserted between the fourth-stage IIT and the CCD chip. The total magnification factor was, therefore, 7/100. The first (HAMAMATSU V4440PX) and second (DEP PP0030X) stages of the IIT chain were the electrostatically focusing type. The third and fourth (PROXITRONIC BV2583EG) were the gatable MCP type. The phosphor of each stage was PS-5, P46, P20 and P20 in that order. The mean decay time of the PS-5, the P46, and the P20 phosphors are about 1.3 μs, 300 ns, and 20 μs, respectively.

The IIT chain of the D-Block consisted of three image-intensifier tubes (DEP PP0040C) and a CCD (Fig. 2.20 (c)). The input window of the first-stage IIT is 80 mm$^\phi$. The first stage of the IIT chain was the electrostatically focusing type with a magnification of 16/80. The second and third IITs were the MCP type. The third-stage IIT were contacted to the CCD chip via a tapered-optical-fiber plate with a magnification of 11/18, giving the total magnification of 11/90. The phosphors of the first, second, and third stages were P24, P20, and P20,

1st stage: converter type
DEP PP0010U

2nd stage: MCP type
DEP XX1450HJ

3rd stage: MCP type
DEP XX1700AB

SciFi-Bundle

CCD (Sony XC-77RR)

ϕ18

phospher P24
$\tau \sim 2.4\,\mu s$

phospher P20
$\tau \sim 50\,\mu s$

tapered fiber 11/18

(a) SciFi-Bundle IIT System

1st stage: converter type
HAMAMATSU VP4440PX

2nd stage: converter type
DEP PP0030x

3rd stage: MCP type
PROXITRONIC BV2583EG

4th stage: MCP type
PROXITRONIC BV2583EG

U-Block

CCD (Sony XC-77RR)

tapered fiber 7/25

ϕ100

ϕ25
phospher PS-5
$\tau \sim 1.3\,\mu s$

phospher P46
$\tau \sim 300\,ns$

phospher P20
$\tau \sim 20\,\mu s$

(b) U-Block IIT System

1st stage: converter type

2nd stage: MCP type

3rd stage: MCP type

D-Block

CCD (Sony XC-77RR)

tapered fiber 11/18

ϕ80

ϕ16
phospher P24
$\tau \sim 2.4\,\mu s$

phospher P20
$\tau \sim 50\,\mu s$

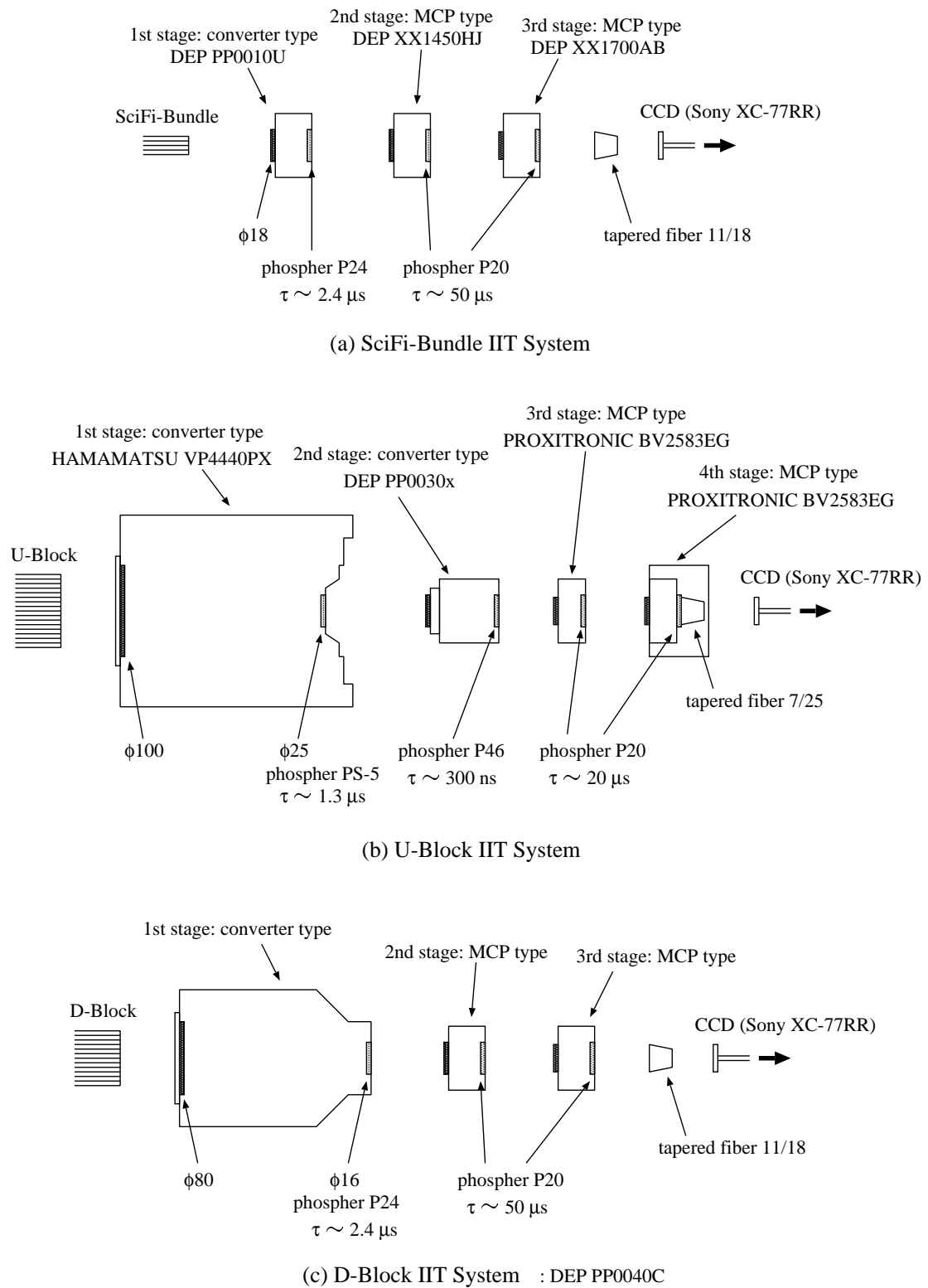(c) D-Block IIT System   : DEP PP0040C

Figure 2.20: Schematic drawing of the structure of IIT chains for (a) the SciFi-Bundle, (b) the U-Block, and (c) the D-Block.

respectively.

2.7 Trigger

For the efficient data taking, the trigger was separated to the first level and the second level. The first-level trigger uses only the hit signals of the plastic scintillators and the aerogel Čerenkov counters, while the second-level uses digitized timing informations and hit addresses of the drift chamber (DC1). The first and second gates in the IIT chains were opened with the first- and second-level trigger, respectively. The signals from PMTs and chambers were digitized with the first-level trigger, but they were cleared if the second-level trigger was not fired.

2.7.1 First-level trigger

The logic diagram of the first-level trigger is given in Fig. 2.21. The incident particles were tagged by the signals from the T1 and the T2. For the exposure of some emulsion stacks, the signal from the TgtDef was also required to reduce the trigger rate. The incident K^- mesons were discriminated by using the BAC counters as a veto. Non-interacting beam particles and scattered pions were rejected with the signal of the BVAC and the FAC, respectively. By taking matrix coincidences of the CH and the FTOF hodoscopes, the charges and momenta of the outgoing particles were roughly selected ("charge trigger", CT). To cut off the neutral particles hitting the FTOF, the "OR"ed signal of the YH was required. Thus, the first-level trigger was defined by

$$T1 \otimes T2 \otimes \overline{BAC} \otimes \overline{BVAC} \otimes \overline{FAC} \otimes CT \otimes YH,$$

or

$$T1 \otimes T2 \otimes TgtDef \otimes \overline{BAC} \otimes \overline{BVAC} \otimes \overline{FAC} \otimes CT \otimes YH.$$

The decision time of the first-level trigger was about 150 ns. Including the cable delay between the IITs and the logic units, the first gates of the IIT chains were opened about 260 ns after a particle hit the T2 counter. The rate of the first-level trigger was typically 75 /spill for the beam intensity of 1.1×10^4 K^-'s/spill.

2.7.2 Second-level trigger

The second-level trigger was used mainly to kill scattered protons, which cannot be discriminate by threshold-type aerogel Čerenkov counters. The main component of the second-level trigger was the mass trigger (MT). In '98 run, the x or y hit of the VH was also required to eliminate the background triggers caused by the neutral particles such as K_s^0 mesons. The second-level trigger for '98 run was defined by

$$1st\text{-}level\ trigger \otimes MT \otimes (VHx \oplus VHy).$$
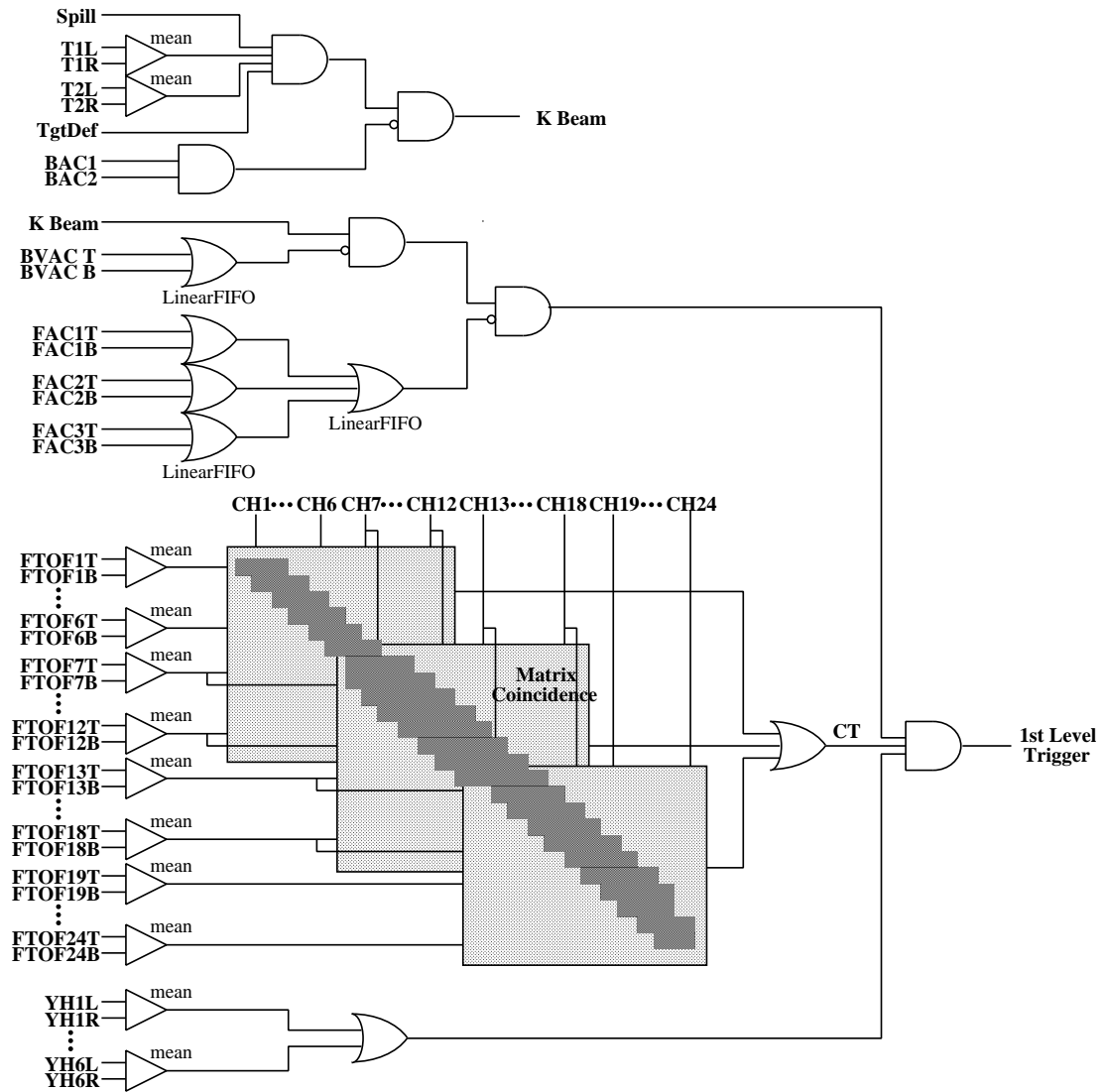
Figure 2.21: Logic diagram of the first-level trigger. The TgtDef signal was not always used.

Since '99 run, the VH hit was replaced by the momentum-selection trigger (MS), which also uses the VH hit information. The second-level trigger for '99 and 2000 run was defined by

$$1st\text{-}level\ trigger \otimes MT \otimes MS.$$

Mass trigger

The principle of the mass trigger is following. When the momenta of outgoing particles are selected using the combination of the CH and the FTOF hodoscopes as like the charge trigger, the difference of their masses should appear as the difference of their TOFs. The particle identification can be done, therefore, by setting a suitable window against TOF for each combination of the CH and the FTOF.

The trigger scheme of the mass trigger is illustrated in Fig. 2.22. The timing information of the CH and the FTOF signals were digitized with LeCroy 4303 TFC (Time-to-Fera Converter) and LeCroy 4300B FERA (Fast Encoding and Read out ADC) modules (FERET). The hit addresses and the timing informations of the FTOF were stored in the memorys in the FERA modules, and the hit informations of the CH were stored in a LeCroy 2375 Data Stack module. The hit addresses of the CH and the FTOF were sent to a LeCroy 2372 MLU (Memory Lookup Unit) module and decoded into momentum informations. Another MLU stored the trigger windows against the FTOF TDC data for corresponding combinations of the CH and the FTOF. It selected the particle masses by combining the FTOF timing data and the momentum informations obtained by the first MLU.

The decision time of the mass trigger was about 14 μs. The trigger rate in '98 run was about 13 per spill for the K^- beam intensity of 1.1×10^4. The contamination due to scattered protons were reduced to typically 1/4 with the mass trigger, while the rate to overkill K^+ mesons were about 8 % (Fig. 2.23).

Momentum-selection trigger

With the mass trigger, the dead time of the data acquisition was about 15 %. In order to reduce the trigger rate and the dead time, additional second-level trigger was developed and applied since 1999 run. Main background of triggered events were proton; high-momentum protons also fire the trigger even when the mass trigger is used, because the velocities of such protons are almost same as those of kaons of $p_{K^+} < 1.4$ GeV/c. The new trigger was designed to reject such high-momentum scattered protons. It can select the momenta of outgoing particles more precisely than the charge trigger by using hit patterns of the VH, the DC1, and the FTOF, and is referred to as "momentum-selection trigger" (MS).

The trigger logic is shown in Fig. 2.24. The logic was established in a TKO module which has four programmable LSIs, Lattice ispLSI3256. The LSIs are connected each other via 64-bit bus line. The trigger module has six 32-channel I/O connectors compatible to TKO TDC modules (Dr.T), two 16-channel I/O
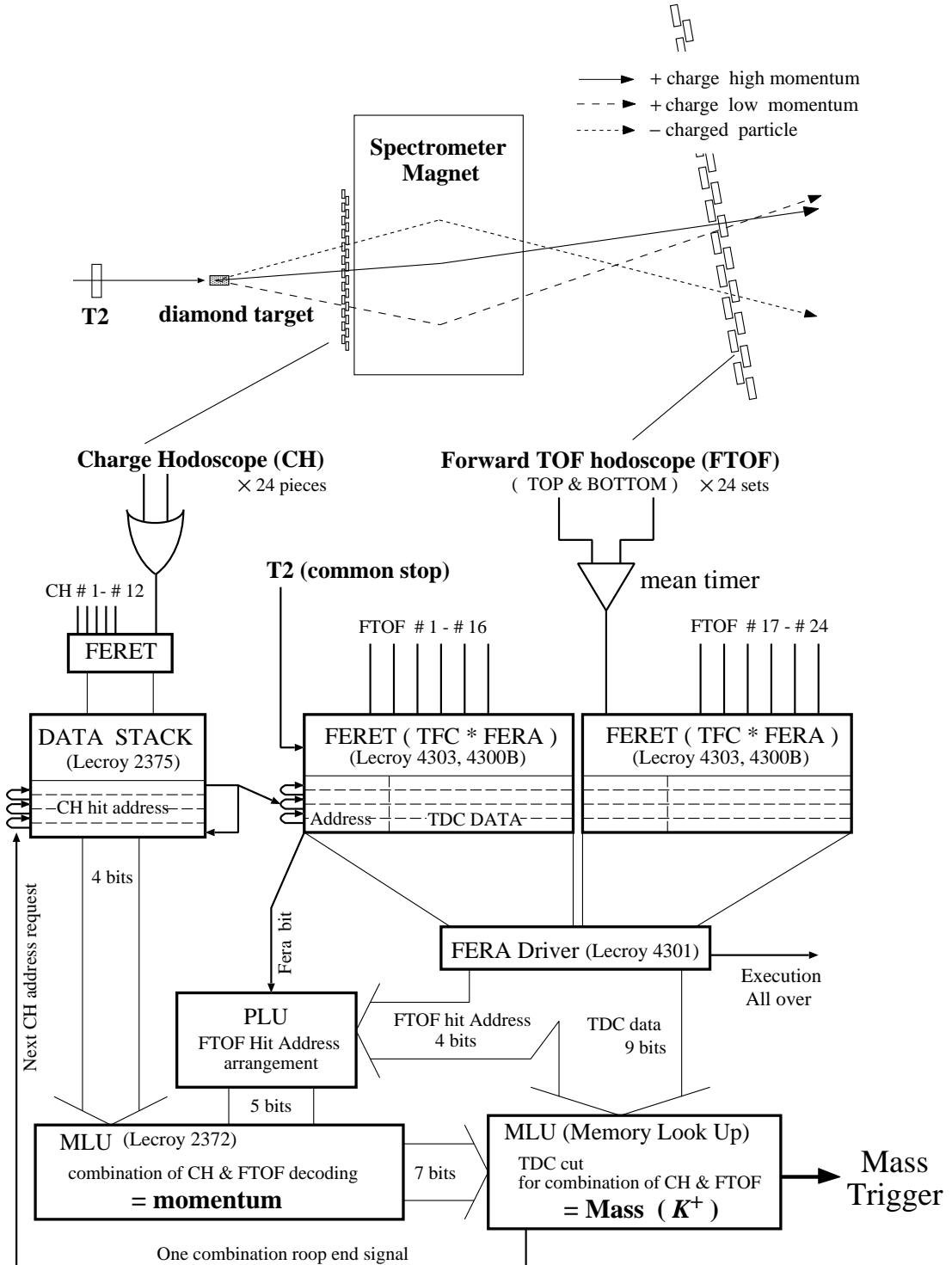
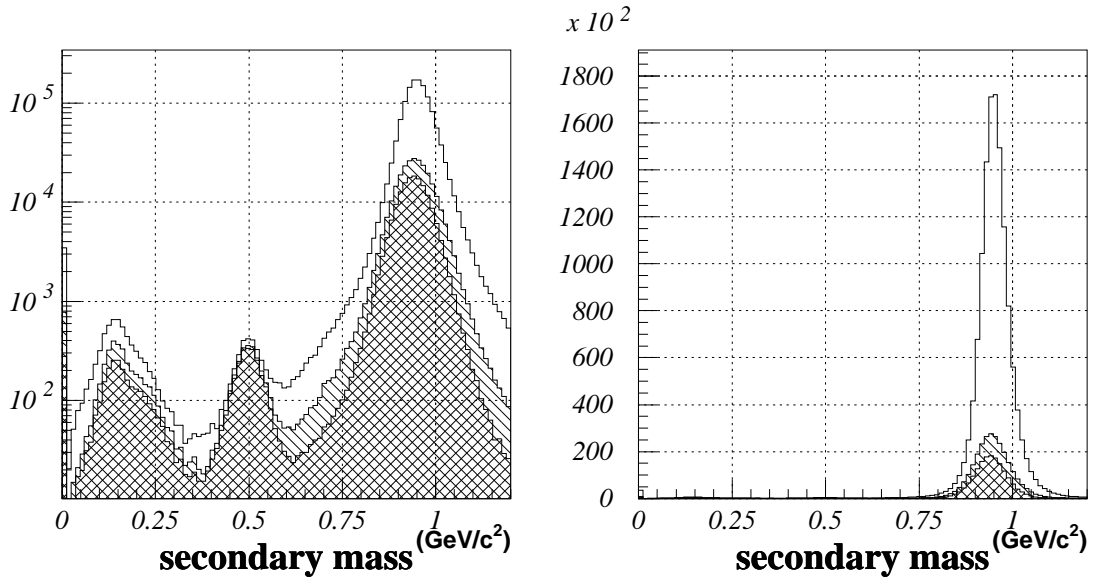Figure 2.22: Logic scheme of the mass trigger.

Figure 2.23: Mass distribution of outgoing particles with the first-level trigger (white), the mass trigger (hatched), and the momentum-selection trigger (doubly hatched).

connectors compatible to PT2 modules [58], three NIM-level input connectors, and three NIM-level output connectors. Details of the module is given in Ref. [59]. The hit addresses of the x and x' planes of the DC1 came from the front panel of the Dr.T modules. The hit signals of the VH and the FTOF also came from Dr.T modules, which were used just as interfaces to the TKO logic module. Although each of the DC1 x and x' planes has 48 channels, outgoing particles in triggered events hit only 32 channels among them. Those 32 channels were selected, therefore, and each of corresponding channels of the x and x' planes were ORed to reduce the inefficiency of the DC1. The trigger was decided by the three-dimensional coincidence map for the VH, the FTOF, and the ORed DC1 signals. The trigger output was synchronized with a 1-μs-delayed first-level-trigger signal. The LSIs were operated with external clock signals of about 20 MHz *.

Using the momentum-selection trigger, the trigger rate of each spill was reduced to less than 10 for 1.3×10^4 K^- mesons, and the dead time of the data acquisition was decreased to less than 10 %. Figure 2.23 shows that the background due to scattered protons were reduced to 2/3 with the momentum-selection trigger. The inefficiency of the trigger for K^+ mesons was less than 2 %.

---

*They can be operated with clock of up to 50 MHz [59].

TKO trigger module

clock

DC1x

Dr.T

Dr.T

DC1x
48ch

hit
address

select
32 channels

DC1x
32ch

DC1x'

Dr.T

Dr.T

DC1x'
48ch

hit
address

make OR
of DC1x and x'

DC1OR
32ch

VHx

Dr.T

VHx
32ch

FTOF

Dr.T

FTOF
24ch

hit
address

**3-dimensional
matrix
coincidence**

Trigger

1st level trigger

LATCH clear

LATCH

Momentum
Selection
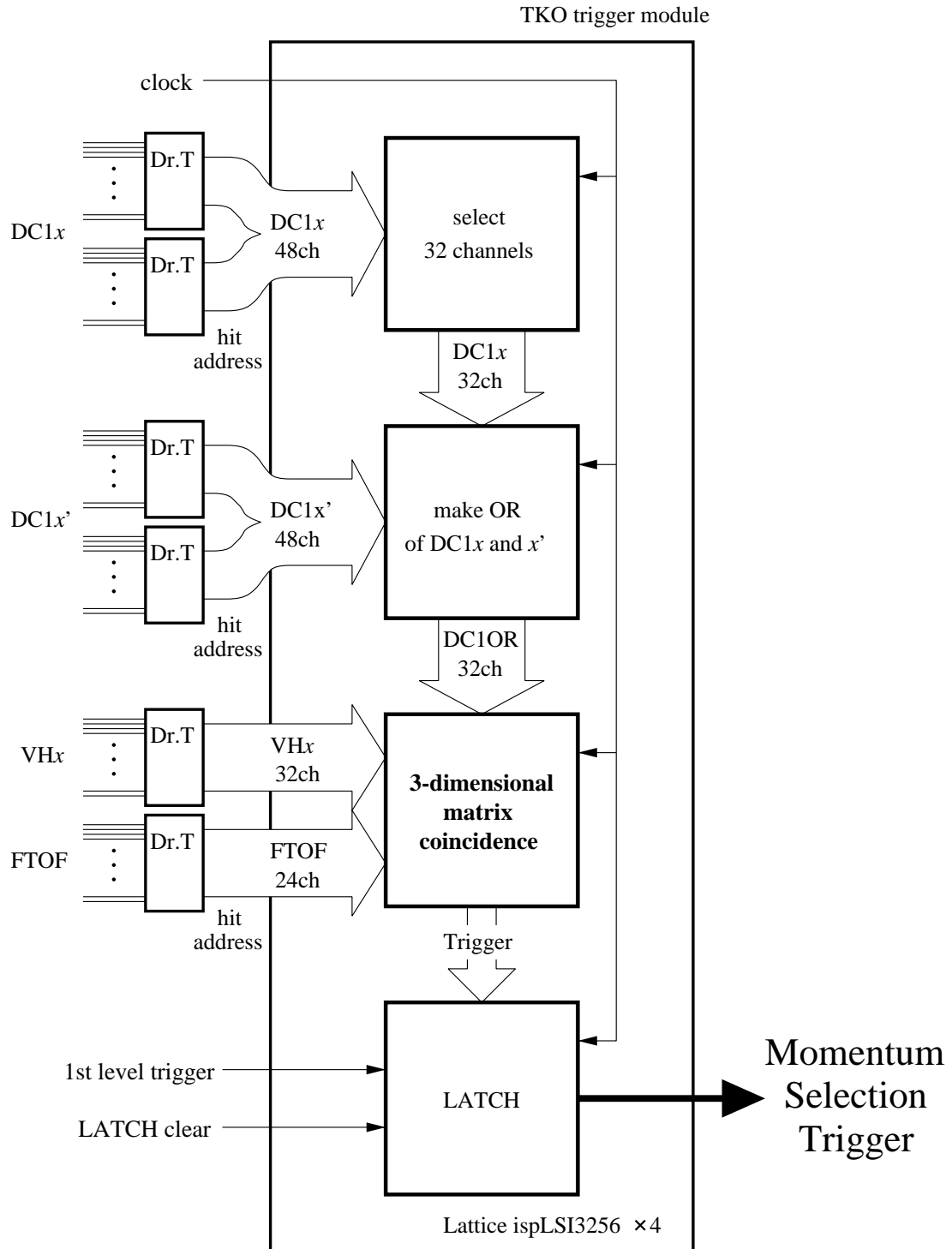Trigger

Lattice ispLSI3256 ×4

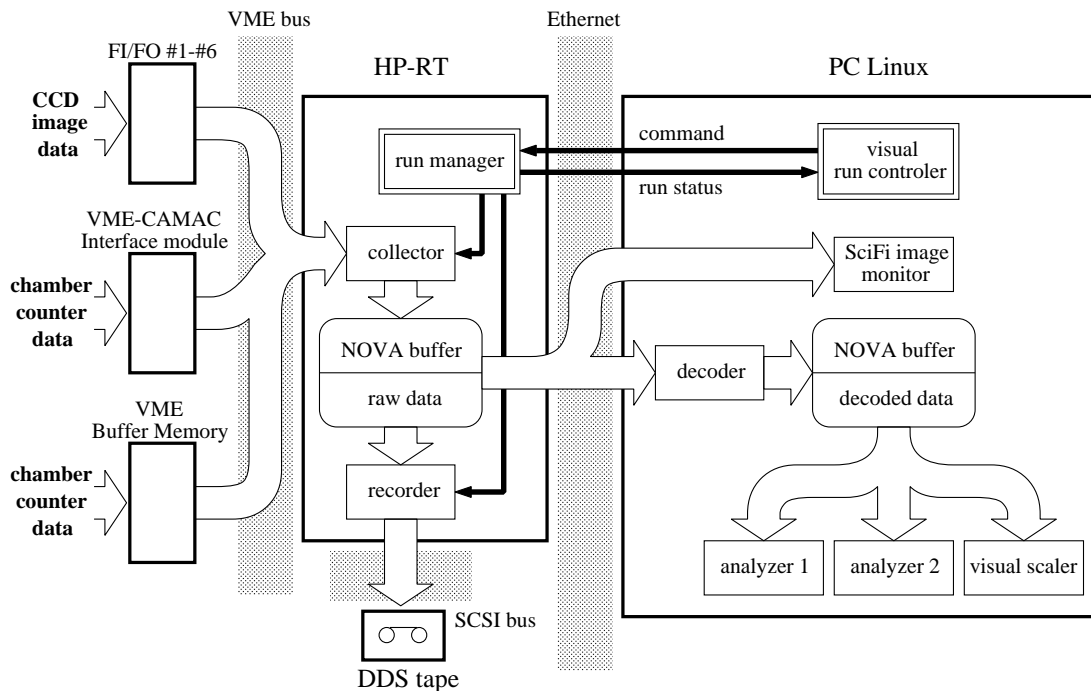Figure 2.24: Logic scheme of the momentum-selection trigger.

Figure 2.25: Schematic diagram of the data flow during the data acquisition and on-line monitoring. See text for detail.

2.8 Data acquisition and monitoring

The data flow during the data acquisition is illustrated by Fig. 2.25. The data acquisition was operated by a HP-RT 2.2 operating system on a VME on-board computer, Hewlett-Packard Model 743. The data of scintillation and Čerenkov counters and wire chambers as well as some trigger flags were acquired by a "collector" from CAMAC memory modules via a CAMAC-VME interface, and from a VME buffer memory module. The digitized CCD images were also acquired by the collector from six first-in-first-out (FI/FO) memory modules. The collected data were managed by a NOVA buffer manager, and recorded in a Digital Data Storage (DDS) tape by a "recorder". In order to monitor the data during the data acquisition, some on-line analyzers were executed on a personal computer operated by a Linux 2.0 operating system. A "decoder" took the raw data from the HP-RT via Ethernet, and decoded it for "analyzers". Some analyzers received it via a Linux-local NOVA buffer manager. An "analyzer" made histograms of ADC/TDC data of counters and hit patterns of wire chambers and hodoscopes. Another "analyzer" tracked the scattered particles and reconstructed their masses. A "visual scaler" counted the scaler values and displayed them together with the current coordinates of the emulsion mover. Especially, K^-/beam ratio was monitored by the visual scaler. The CCD images were sent to an on-line monitoring software directly from the HP-RT buffer manager, and
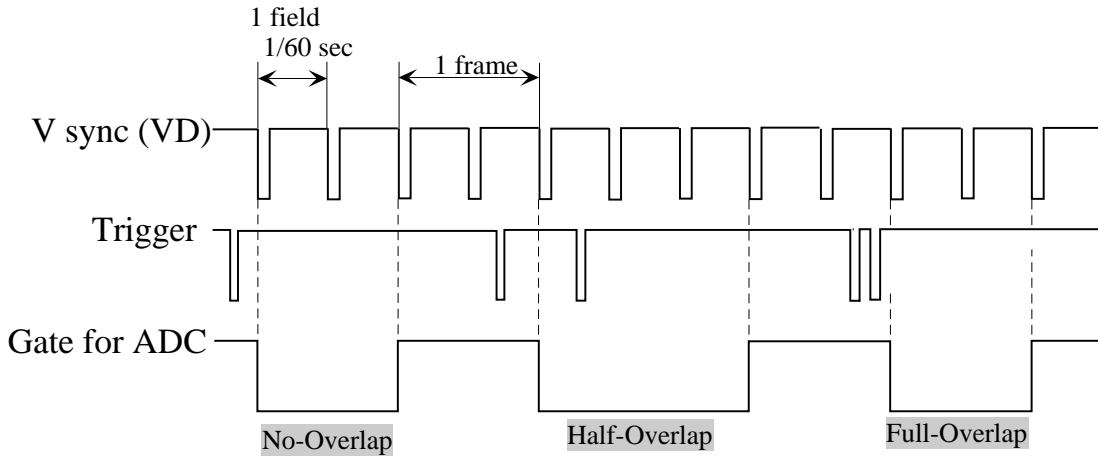
Figure 2.26: Timing chart of the data acquisition of the CCD images. When two triggers are fired in two fields timing, the images of the two events are half-overlapped. If two triggers are fired in one field timing, the images are fully overlapped.

monitored by human eyes. The run control (start, stop, pause, or resume) was carried out from the Linux PC via Ethernet.

The acquisition of images from the CCD cameras was performed with three kinds of modules, a clock-and-coordinate generator (CCG) module, flash ADC (FADC) modules and FI/FO modules. The CCG module provided a common clock (14 MHz) to synchronize the whole system, and generated two-dimensional coordinates of each CCD pixel (H:10-bit, V:10-bit). It initiated a sequence of digitization when the second-level trigger was fired. The FADC modules digitized the pulse height of the video signals into 8-bit brightness data for each pixel. For those pixels having brightness above some threshold, the write-strobe signals to the corresponding FI/FO module were generated. Then, the data on the brightness, the coordinates, and the 4-bit event number were stored in the memory of the FI/FO module. Each of the FI/FO modules had four FIFO chips, IDT-7207 for the SciFi-Bundle and the U-Block and IDT-7208 for the D-Block. The total memory size of a module was 128 kB (IDT-7207 $\times$ 4) or 256 kB (IDT-7208 $\times$ 4).

The timing chart of the sequence is shown in Fig. 2.26. In the NTSC format, the video signal of one frame consists of two parts, namely, the even-field and odd-field. The two fields were read out alternately triggered by the vertical synchronization signal (VD). As shown in Fig. 2.26, tracks of two or more successive triggered events can be appeared in one image, depending on the timings of triggers. When two triggers were fired in two fields timing, three fields data were acquired. The tracks of the first event appeared in the first two fields, and those of the second event in the last two fields. Therefore, only the middle field had the images of the two events. Such an image is referred to as "half-overlap". On the other hand, when two triggers were fired in one field timing, both two

fields had the images of the two events. Such an image is called as "full-overlap". Depending on how the triggers are inhibited during the image data acquisition, there are three types of acquisition mode;

1. half-overlap mode

   If the triggers are forbidden while acquiring one field, the images can be half-overlapped to those of the next or previous triggered event. Although this mode enlarges the dead time, it is reduced to 7.5 ms in average, one third shorter than that in the no-overlap mode. The images belonging to the next or previous triggered event can be erased by an off-line analysis (see Appendix A for details). This mode was used in 2000 run, because the trigger rate was reduced by use of the momentum-selection trigger.

2. full-overlap mode

   If triggers are not inhibited while acquiring the image data, tracks of two or more successive triggered events can appear in one half-overlap or full-overlap image. A full-overlap image cannot be resolved even by an off-line analysis. In the '98 run, the data acquisition was performed in this mode in order to avoid the much dead time.

3. no-overlap mode

   By inhibiting the trigger signals during the whole acquisition of two fields of the images, CCD images without overlapping each other can be acquired. However, the dead time of the data acquisition is significantly increased, because it takes 22.5 ms in average to take two fields of image. This mode was used mainly for the calibration run, such as for obtaining range-energy relation in the SciFi-Block detectors and for gain tuning of the IIT chains.

Chapter 3

Data Analysis

The data analysis was performed as follows. First, the (K^-, K^+) reaction events were selected with the data of the spectrometer system. Next, the events without a thick track detected in the SciFi-Bundle detector were rejected by using the brightness information of the Bundle. The survived events were scanned by human eyes and only events suitable for emulsion analysis were accumulated. The predictions of the positions and angles of Ξ^- hyperon candidate tracks were obtained from the track data of the SciFi-Bundle. Then, the tracks of the Ξ^- hyperon candidates were searched for and traced in emulsion with newly-developed automatic scanning systems.

In this chapter, the event selection is described in detail together with the performance of the SciFi detectors and the range-energy calibration of emulsion.

3.1   Selection of (K^-, K^+) reaction

3.1.1   Identification of incident K^- mesons

The species of beam particles were identified by measuring the time-of-flight (TOF) between the T1 and T2 counters. The TOF spectrum of incident particles is presented in Fig. 3.1. Typical TOF resolution was about 75 ps after the correction using the ADC informations. The dominant peak corresponds to K^- mesons, and we have set the window for K^- mesons as indicated by the arrows in the figure. The contamination of π^- mesons in the K^- beam was 0.20 %.

3.1.2   Identification of outgoing K^+ mesons

The identification of outgoing particles was performed by measuring their momenta and velocities. Their momenta were analyzed with the KURAMA magnetic spectrometer, the wire chambers, and the scintillator hodoscopes. The tracks upstream of the KURAMA magnet were reconstructed by the VH and CH hodoscopes and the DC1 chamber, and downstream tracks were measured
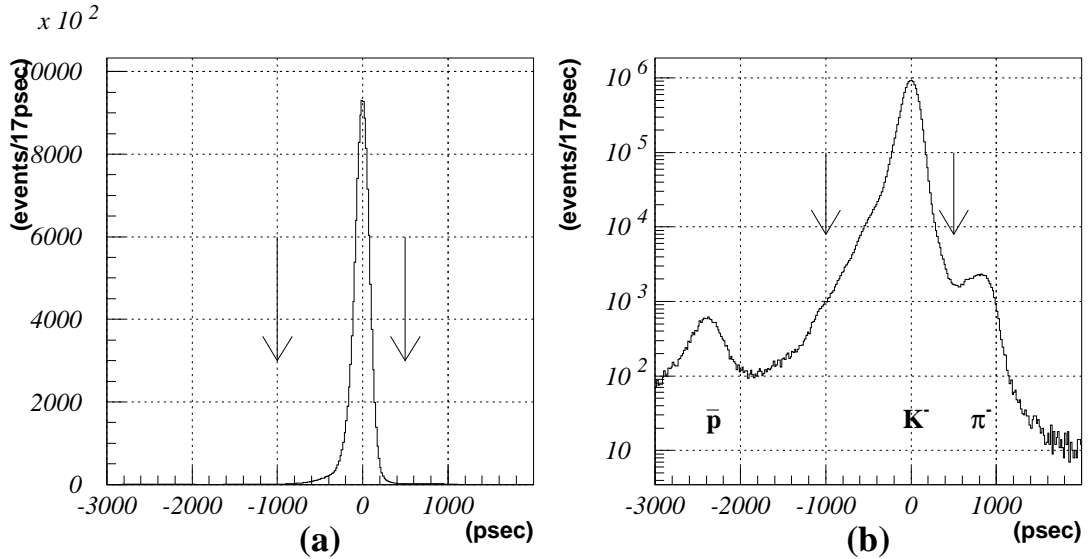
Figure 3.1: TOF spectrum of incident particles (a) in a linear scale and (b) in a logarithmic scale. The arrows indicate the selection window for K^- mesons.

by the DC2, DC3, and LST chambers. The velocities of scattered particles were obtained by measuring the TOF from the T2 counter to the FTOF array.

First, the data of the DC2, DC3, and LST were fitted to a straight line in each of xz plane and yz plane to reconstruct the track downstream of the KURAMA. It was required that the hit channel of the FTOF wall matched with the track reconstructed with the wire chambers. The vertical hit position of the FTOF can be obtained by measuring the time difference between the signal from the top-side PMT and that from the bottom-side one, and was required to match the reconstructed track within 65 mm. Next, the data of the DC1, VH, and CH were fitted to a straight line in each of xz plane and yz plane for the track reconstruction upstream of the KURAMA. The bending angle of the scattered particle in xz plane was derived from the fitted straight tracks. The bending point was determined as the closest point of the tracks, and was required to be near the center of the pole gap of the KURAMA. If the distance of the tracks at the bending point was more than 115 mm, the event was cut off. The deviation of the vertical position at the DC1 y plane between the tracks needed to be less than 36 mm. The χ^2 cut parameters for the tracking were set widely, as shown in Fig. 3.2. The typical tracking efficiency was 67 % for triggered events.

The velocity β of the scattered particle was calculated from the flight length obtained from the reconstructed tracks and the TOF between the T2 and FTOF counters. In order to avoid the deterioration of the timing resolution due to the nuclear interaction in the scintillator, the FTOF hit with the ADC overflowed was rejected. The TOF resolution was typically 130 ps after the ADC correction.

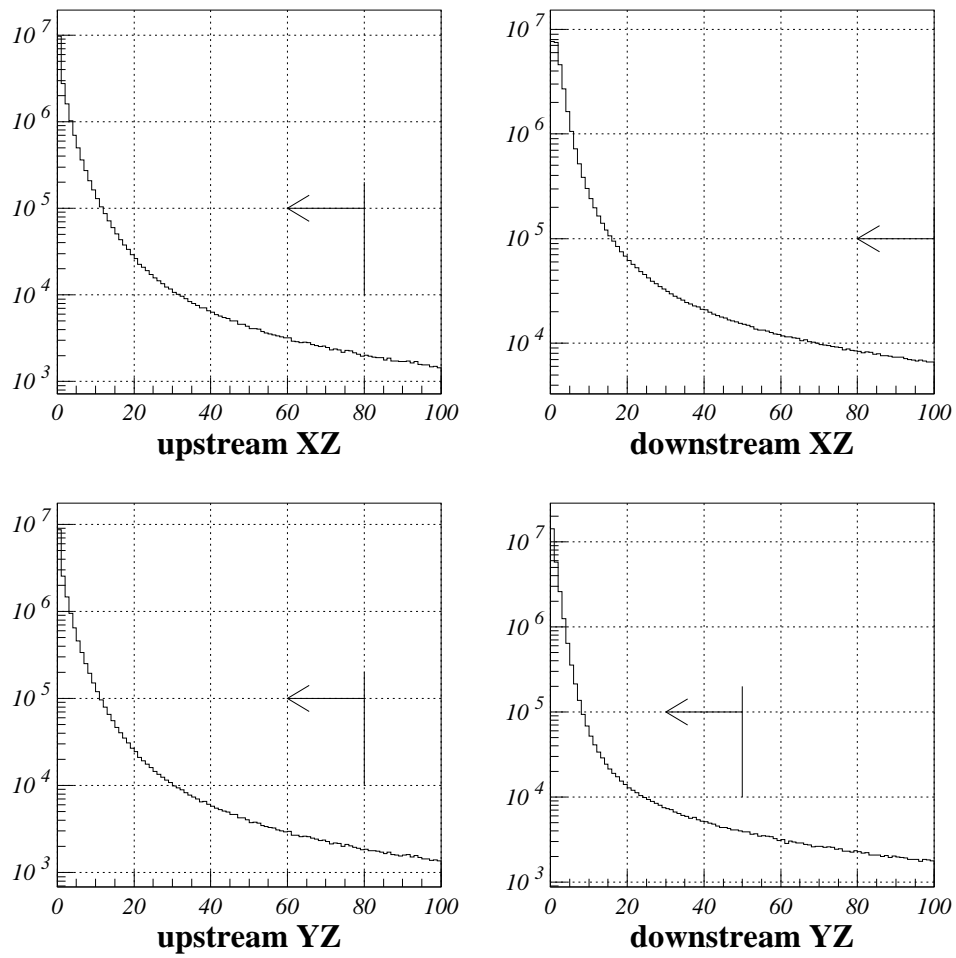For the quasi-free (K^-, K^+) reaction events, the K^+ meson momentum was

Figure 3.2: χ^2 distributions of the track fitting upstream and downstream of the KURAMA spectrometer.
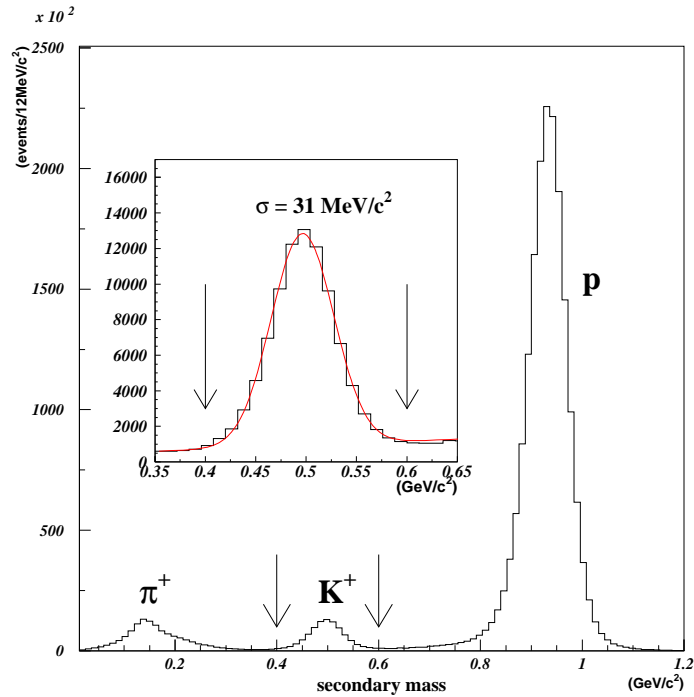
Figure 3.3: Mass spectrum of the scattered particles. The arrows indicate the window for K^+ meson selection.
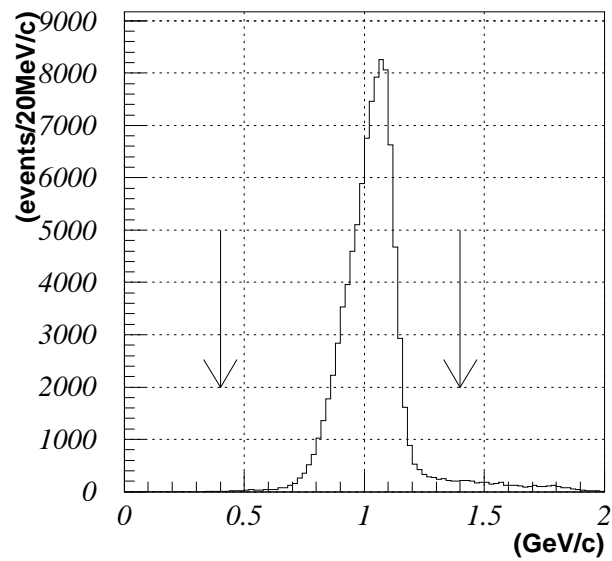

Figure 3.4: Momentum spectrum of the outgoing K^+ mesons. The arrows indicate the selection window.
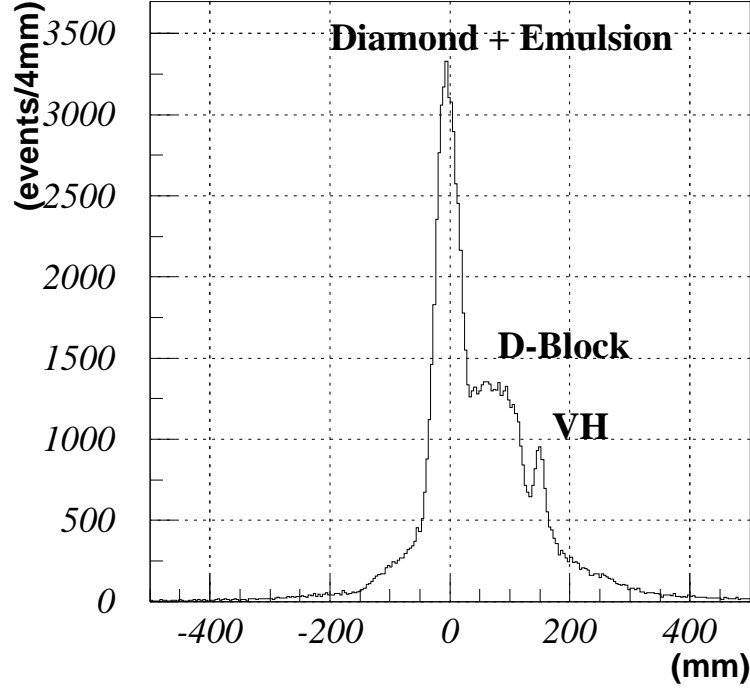
Figure 3.5: Position distribution of the (K^-, K^+) reaction vertex along the beam direction.

expected to be distributed from 0.8 GeV/c to 1.2 GeV/c. Therefore, scattered particles having a momentum between 0.4 GeV/c and 1.4 GeV/c were selected. Figure 3.3 shows the reconstructed mass spectrum of the scattered particles. Three peaks corresponding to π^+, K^+ mesons, and proton are clearly seen. The particles with the mass between 0.4 GeV/c and 0.6 GeV/c were selected as K^+ mesons, as indicated in the figure. The mass resolution was 31 MeV/c^2 in r.m.s. for the K^+ mesons. The momentum spectrum of the outgoing K^+ mesons is presented in Fig. 3.4.

The (K^-, K^+) reaction vertex was obtained to be the closest point of the track of the incident K^- meson and that of scattered K^+ meson upstream of the KURAMA magnet. The incident beam tracks were reconstructed by the wire chambers of BPC3, 4, and 5. The x and y positions of the vertex were required to be within ± 50 mm around the center of the diamond target. The z position cut was not applied because the z position resolution was not enough, especially for the events accompanied with forward scattering. Figure 3.5 shows the reconstructed vertex position along the beam direction. The dominant peak corresponds to the diamond target and the emulsion stack, and the bump downstream of it corresponds to the D-Block. The small peak appearing downstream of the bump corresponds to the VH hodoscope.

Figure 3.6 (a) shows the missing-mass spectrum of the $p(K^-, K^+)X$ reaction for the events selected as the (K^-, K^+) reaction event. The clear peak corre-
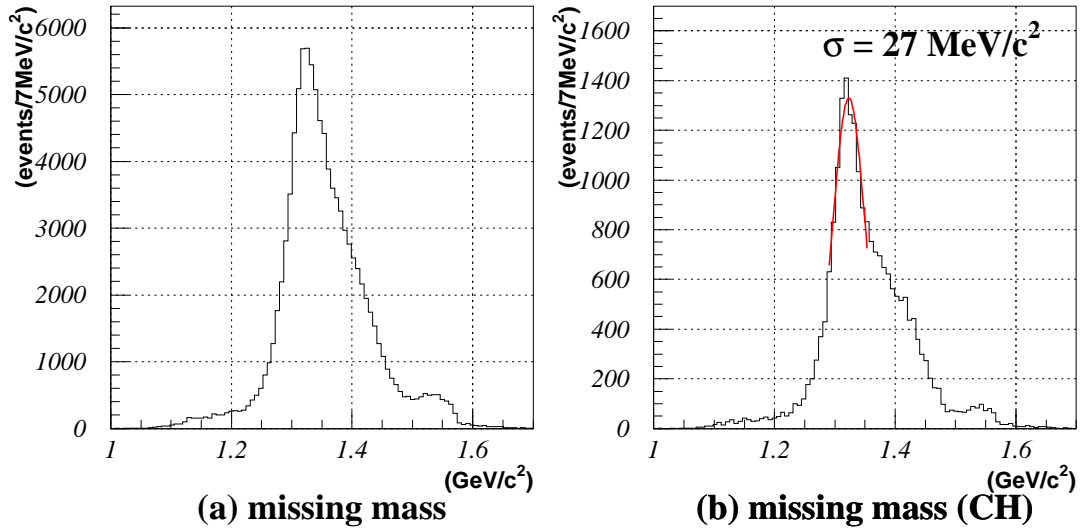
Figure 3.6: Missing-mass spectrum of the $p(K^-, K^+)X$ reaction (a) for all (K^-, K^+) reaction events, and (b) for events the reaction occurred in the D-Block.

sponds to Ξ^- hyperons, and were broaden due to the Fermi momentum in the nuclei. The spectrum only for the events with the z position of the reaction vertex in the D-Block is given in Fig. 3.6 (b). Since there were free protons in the scintillating fibers of the D-Block, the narrower peak at 1.32 GeV/c^2 can be considered to correspond to the free $p(K^-, K^+)$ reaction events. The missing-mass resolution was obtained from this peak to be 27 MeV/c^2.

Then, out of 1.3×10^7 triggered events, 9.0×10^4 events were selected as those associated with the (K^-, K^+) reaction.

3.2 Reconstruction of SciFi image

Images are distorted mainly due to the pin-hole distortion caused by the electrostatic lenses of IITs. The distortion can be expressed as:

$$\begin{pmatrix} X' \\ Y' \end{pmatrix} = (a_0 + a_1 r + a_2 r^3 + a_3 r^5 + \cdots) \begin{pmatrix} X \\ Y \end{pmatrix}, \qquad (3.1)$$

where (X, Y) and (X', Y') represent original coordinates and distorted ones, respectively, and r is equal to $\sqrt{X^2 + Y^2}$. The coefficients a_i are correction parameters. Since these SciFi-Block systems were installed very close to the spectrometer, their images were also distorted by the magnetic field (about 0.01 or 0.02 T), although we minimized the distortion by covering each IIT chain with a double magnetic shield made of iron and μ-metal. Therefore, the pin-hole distortions as well as the effect due to the remaining magnetic field were corrected

Table 3.1: Position precision and resolution (r.m.s.) for straight tracks of minimum-ionizing particles.

	cluster residual	track width
U-Block	290 μm	350 μm
D-Block	250 μm	290 μm

with following expression:

$$\begin{cases} X' = b_0 + b_1 X + b_2 Y + b_3 X^2 + b_4 XY + b_5 Y^2 + b_6 X^3 + b_7 X^2 Y + b_8 XY^2 + b_9 Y^3 \\ Y' = c_0 + c_1 X + c_2 Y + c_3 X^2 + c_4 XY + c_5 Y^2 + c_6 X^3 + c_7 X^2 Y + c_8 XY^2 + c_9 Y^3 \end{cases}$$
$$(3.2)$$

The correction parameters, b_i and c_i, were determined using the images of a plate with a grid-pattern holes, which was attached to the input window of each IIT and illuminated by a LED. Figure 3.7 (a) presents the grid image viewed by the IIT of the U-Block, and Fig. 3.7 (b) shows that after the correction using the equation 3.2. The error of the correction was estimated from the differences between the corrected positions of the grid points and their real positions. The standard deviation of the differences was 130 μm for the U-Block and 145 μm for the D-Block.

After this correction image reconstruction was performed. Figure 3.8 shows an example of a reconstructed image, where the decay of a Ξ^- hyperon can be clearly seen. Details of the image reconstruction are presented in Appendix A.

3.3   Performance of the SciFi detectors

We employed low-energy proton and pion beams as well as minimum-ionizing beams for calibrating the SciFi-Blocks. A K^- beam of about 1.66 GeV/c was used to evaluate the position resolution. For calibrating the range-energy relation, data with a proton beam of about 600 MeV/c and a π^- of about 400 MeV/c were analyzed. The capability of the separation of stopped-π^-/stopped-proton was also evaluated with the data of the low-momentum beams.

3.3.1   Position resolution

The position precision and resolution of the SciFi-Blocks were evaluated with the values of "cluster residual" and "track width", respectively. The cluster residual is defined as the distribution of the length from a fitted straight-line to the center of each photon cluster. The track width is the distribution of the distance from one track to each pixel weighted by the brightness of the pixel. The results are summarized in Table 3.1.

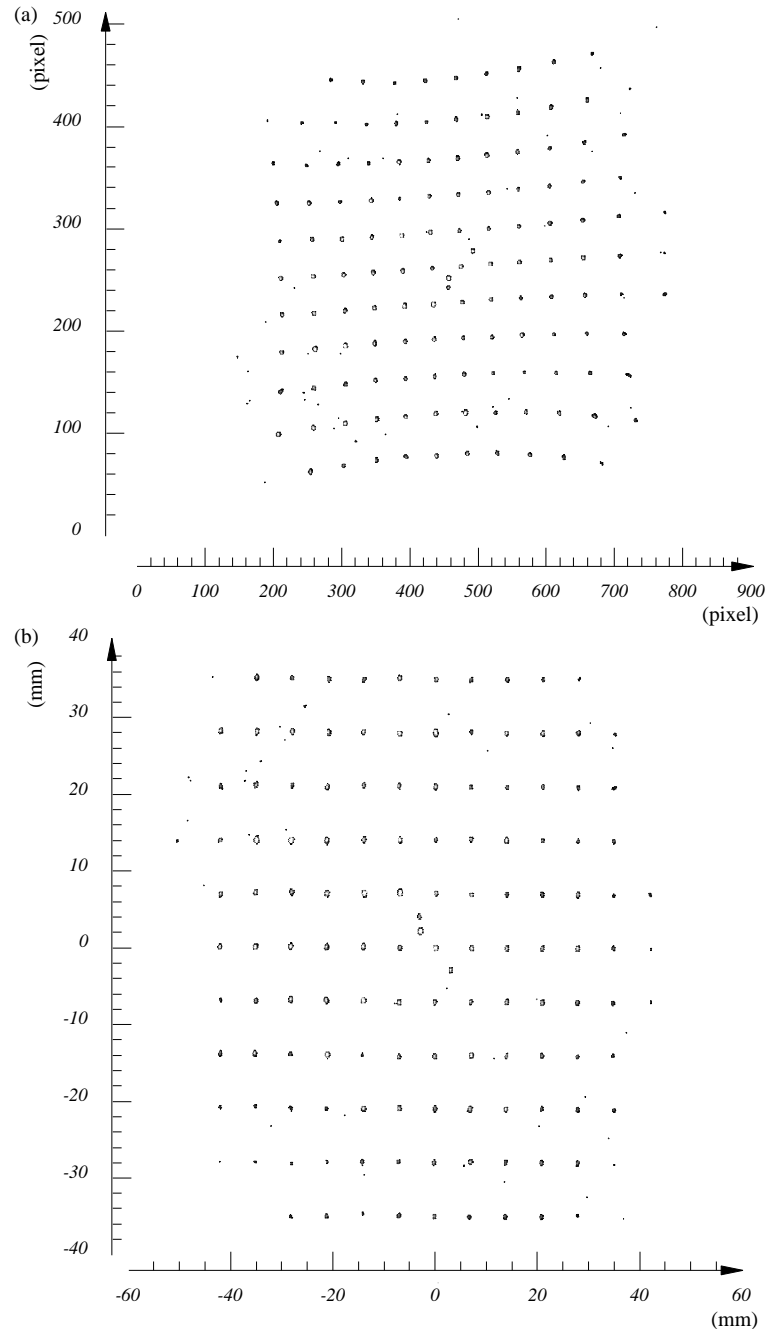Figure 3.7: The grid image viewed by the IIT of the U-Block (a) before and (b) after the correction.
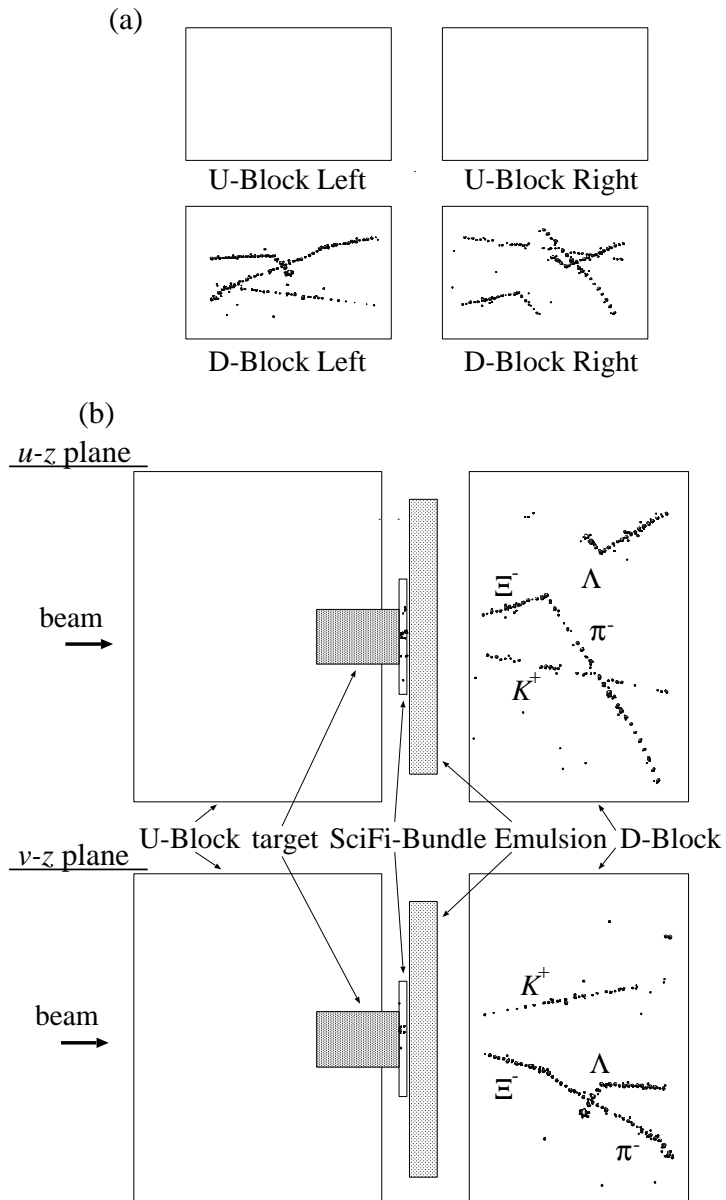
Figure 3.8: Example of image reconstruction. (a) Images before reconstruction (after calibration) and (b) those after reconstruction. A Ξ^- hyperon decaying in the D-Block can be clearly seen. The incident K^- meson was not observed because it had passed through the center hole of the U-Block.
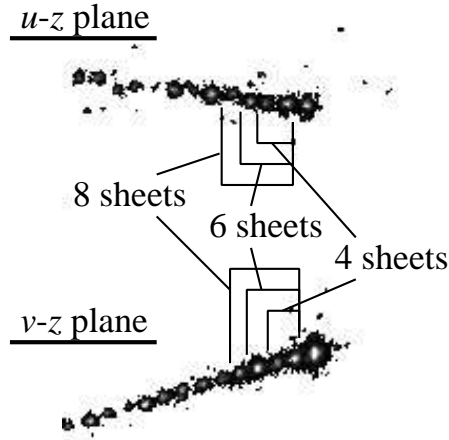
Figure 3.9: Image near the stopping point of a π^-. Since the brightness of the stopping point of a π^- can be very high, the brightnesses of the stopping tracks of π^- mesons and protons are compared without including the stopping points.

The worse resolution of the U-Block comes from the difficulty of packing the fiber sheets because of its complicated structure. Taking into account the precision of the packing, these results were consistent with the expected values, which were calculated based on the size of the fibers, the distortion of the images, the resolution of the CCDs and the cluster size of one photon.

3.3.2 Stopped-π^-/stopped-proton separation

It is important to distinguish whether a decay daughter of a hypernucleus is a pion or not in order to determine the decay mode of the hypernucleus, i.e., mesonic decay or non-mesonic decay. Furthermore, when a π^- meson comes to rest in a material, it is absorbed by a nucleus, and then some evaporated particles are emitted. In the case of an event which shows a kink track in the SciFi-Blocks, it is necessary to distinguish whether the track is a scattered π^- meson or an evaporated particle from the stopping point of a π^- meson in order to determine the stopping position of the π^- meson for its range measurement.

The separation capability was studied using the low-momentum π^- mesons and protons. Identification of the beam particles was made based on the TOF through the beam line. The peaks of the TOF for π^-, μ^- and e$^-$ particles were clearly separated.

Figure 3.9 shows an example of an image of a stopped π^- meson. Since the brightness of light emitted from a fiber is proportional to the energy loss of a particle in the fiber, the brightness distribution varies depending on the particle species, like the "Bragg curve". It is possible to distinguish π^- mesons from
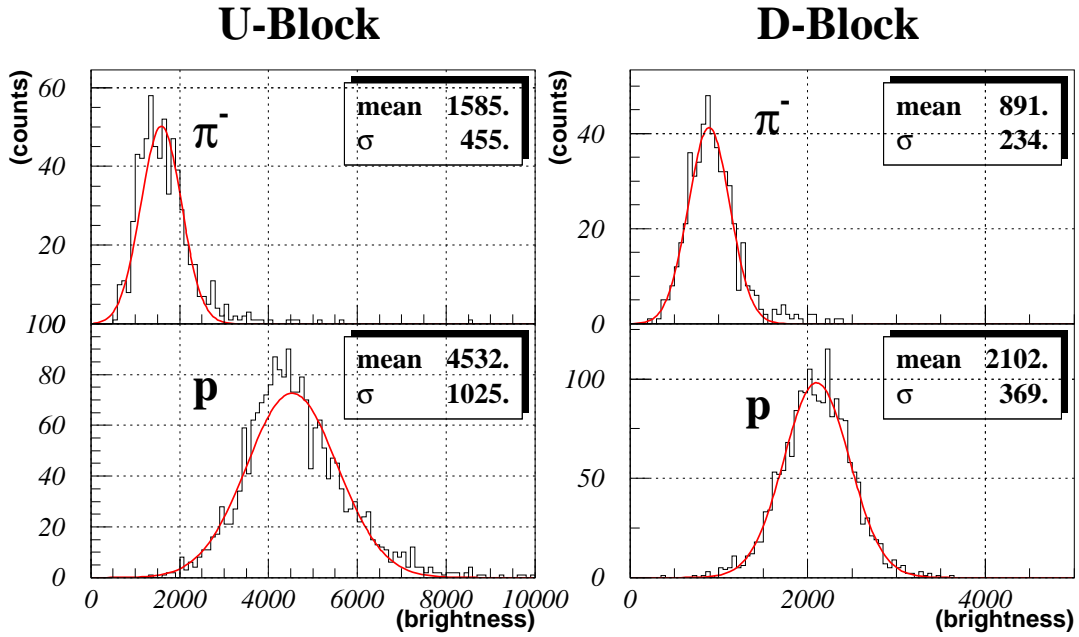
Figure 3.10: Mean brightness (per mm) near the stopping points of π^- mesons and protons calculated from eight fiber sheets.

protons by comparing the mean brightness per track length near the stopping point. Because the brightness of the stopping point of a π^- meson can be very high due to the short-range particles from evaporation, the brightnesses of tracks of stopping π^- mesons and protons were compared without including the stopping points. Since the gains of the IITs are different from each other, the brightness was obtained by calibrating the ADC value using the track of minimum-ionizing particles.

Figure 3.10 shows the result in which the mean brightness was obtained using 8 fiber sheets. The threshold brightness to separate π^- mesons from protons, T, was determined as a point of interior division between the peaks of π^- mesons and protons:

$$T = \frac{\sigma_\pi \mu_p + \sigma_p \mu_\pi}{\sigma_\pi + \sigma_p},$$

where σ_π and μ_π are the standard deviation and the mean of the brightness distribution of the π^- mesons, respectively; σ_p and μ_p denote those for protons. For the U-Block, the distance from the threshold T to the π^- mesons peak was 2.0 σ_π and that to the peak of protons was 2.0 σ_p. This means that 97.7% of the π^- mesons or protons were distributed below/above the threshold. In the case of the D-Block the distance between the brightness peak and a threshold was also 2.0 σ_π for the π^- mesons and 2.0 σ_p for the protons.

The distances of the peaks and the ratio of the distribution are summarized in Table 3.2. Even using only 4 fiber sheets, more than 94% of the π^- mesons

Table 3.2: Distances from the peaks of the mean brightness of π^- mesons and protons to the threshold values, and the ratio of the distribution.

total number	U-Block		D-Block	
of fiber sheets	distance	ratio	distance	ratio
4	1.8 σ	96.2 %	1.6 σ	94.0 %
6	1.9 σ	97.3 %	1.8 σ	96.4 %
8	2.0 σ	97.7 %	2.0 σ	97.7 %

and protons were distributed below and above the threshold, respectively.

3.3.3   Range resolution

As mentioned in Sec. 2.6, the main purpose of the SciFi-Blocks is to measure the energy of a particle from its range in the blocks. The range resolution of the SciFi-Blocks is very important for precise measurements of the masses of hypernuclei.

An analysis for the range resolution was made for the U-Block. The incident energy at the SciFi-Block as well as particle identification was determined from the TOF. The relation between the TOF and the incident energy, and the error of the incident energy were estimated with a simulation. Only those events which included a simple straight track in the image were selected. Each proton track was fitted to a straight line and its range was determined by automatic tracking software. For π^- mesons, however, all the events were scanned by human eyes because the event topology might be more complicated.

The results are shown in Fig. 3.11. The curves on the plots are the results of the fitting to the well-known relation between range R and energy T,

$$R = a \times T^b,$$

where a and b are the fitting parameters.

The range resolution was estimated from the distance from the fitted curve to each data point and from the error of the incident energy. It was 1.1 mm for 37 MeV π^- mesons and 0.57 mm for 47 MeV protons. These values are almost same as the results of a simulation which included the effect of range straggling. The values from the simulation were 1.1 mm and 0.55 mm, respectively. These range resolutions are equivalent to the energy resolutions of 0.86 MeV for 37 MeV π^- mesons and 1.4 MeV for 47 MeV protons.

Finally, we have reconstructed the mass of Λ hyperons which decayed to π^- mesons and protons in the SciFi-Blocks using the obtained range-energy relation. Figure 3.12 shows the mass distribution for Λ hyperons reconstructed from the ranges of the π^- mesons and protons, both of which stopped in the SciFi-Block.
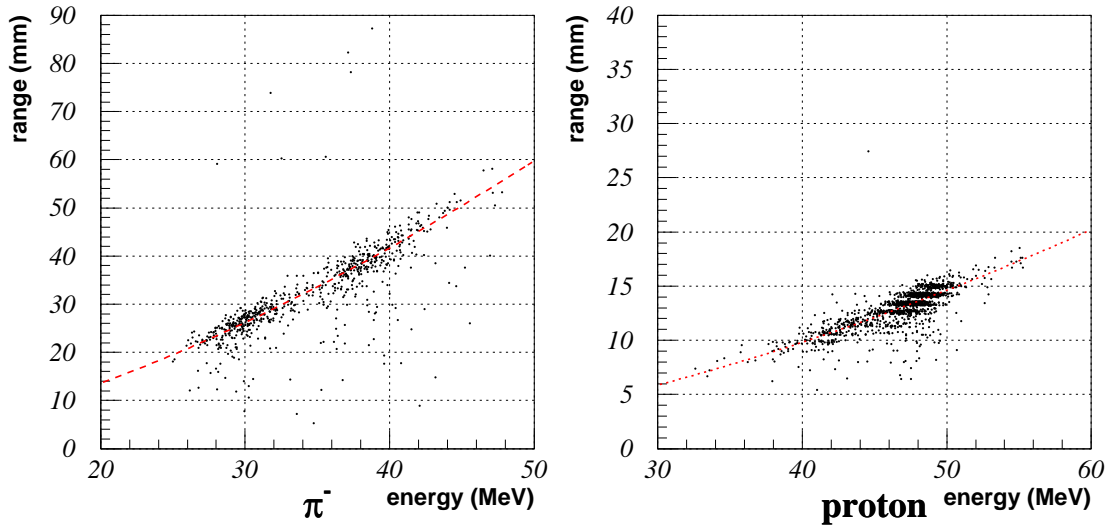
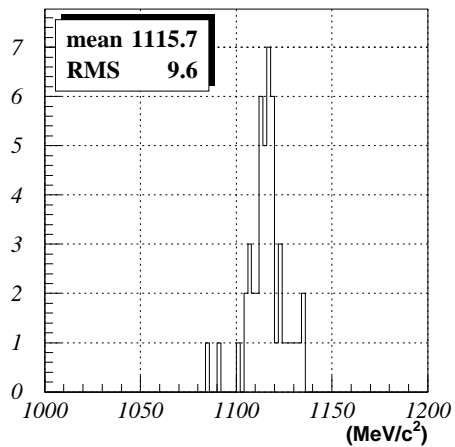Figure 3.11: Range-Energy curve for π^- and proton.

Figure 3.12: The mass distribution of Λ hyperons calculated from the range and the angle of the tracks of π^- and proton.

(a) Brigtness sum
for Fiber-bundle-L

(b) Brightness sum
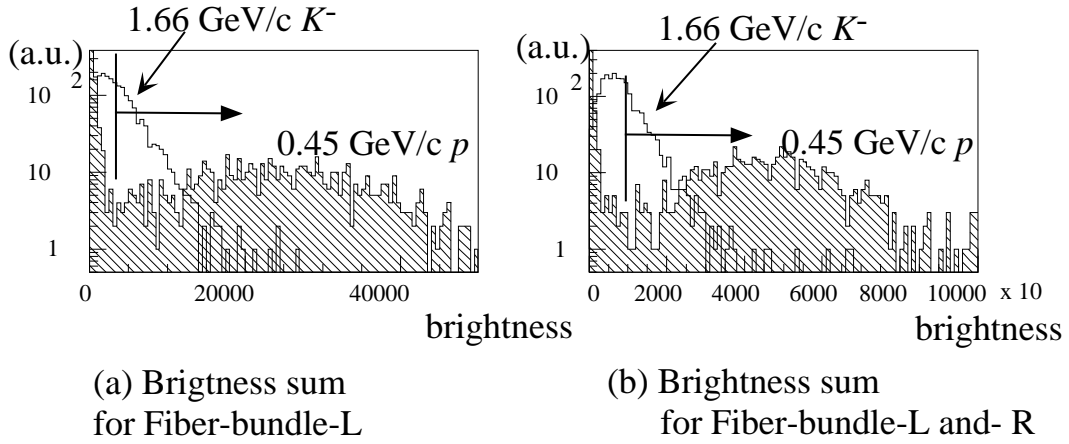for Fiber-bundle-L and- R

Figure 3.13: Brightness distribution of the SciFi-Bundle for 1.66 GeV/c K^- mesons (white histograms) and 0.45 GeV/c protons (hatched histograms). (a) The summed brightness of images from the left IIT. (b) Sum of those from the both IITs.

The mean value of the mass was 1115.7 ± 1.4 MeV/c^2, which demonstrates the validity of our range-energy relations.

3.4 Ξ^- tracks scanning in the SciFi detectors

The positions and angles of Ξ^- hyperons, produced via the (K^-, K^+) reaction, on the surface of the emulsion stack were measured by scanning the images of the SciFi-Bundle detector.

Among (K^-, K^+) reaction events tagged by the spectrometer analysis, events accompanied with tracks of highly ionizing particles detected in the SciFi-Bundle were selected by using the brightness information of the SciFi-Bundle. The 8-bit pulse heights of all pixels in an image read from a IIT were summed up for each (K^-, K^+) reaction event. If either the image brightness from the left IIT or that from the right IIT was less than threshold or the sum of them was less than another threshold, the event was rejected. The thresholds were determined using 1.66 GeV/c K^- meson and 0.55 GeV/c proton beams. The 0.55 GeV/c protons were degraded to about 0.45 GeV/c in the diamond target, which is an expected momentum of a Ξ^- hyperon brought to rest in the emulsion stack. Figure 3.13 shows the distribution of the brightness sum of the images from the left IIT and that of the sums of images from the both IITs. The white histograms are for 1.66 GeV/c K^- mesons and the hatched ones for 0.45 GeV/c protons. The thresholds for the brightness sum of an image from one IIT and for that of images from two IITs were set as indicated in the figures.

After the brightness cut of the SciFi-Bundle, the images from the all SciFi detectors were scanned by human eyes. First of all, the type of the event was
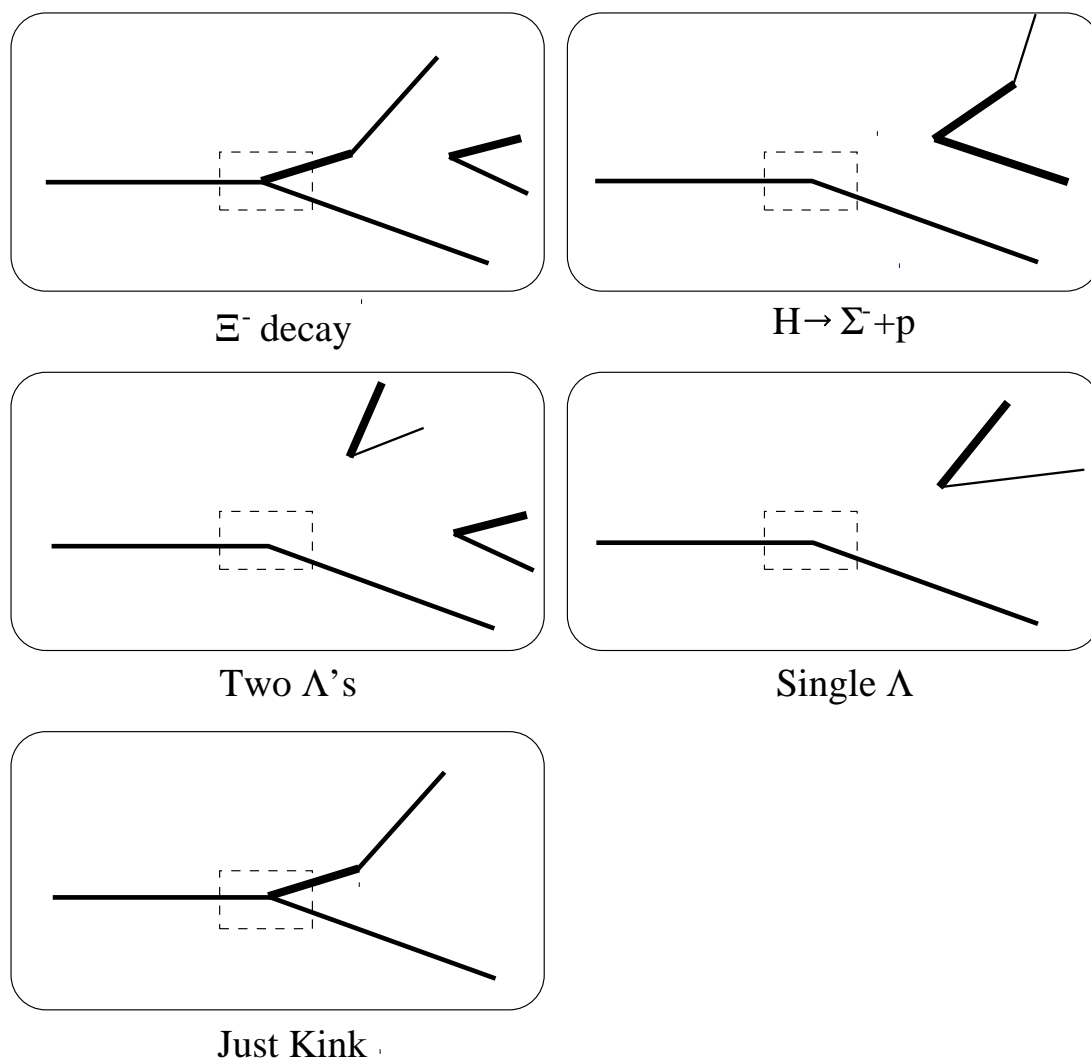
Figure 3.14: Categories of event topology.

Table 3.3: Result of the event selection using the image data from the SciFi detectors.

(K^-, K^+) reaction events	32618
after the brightness cut of the SciFi-Bundle	14177
after the vertex cut	9711
Events with Ξ^- hyperon track candidates	5096

Table 3.4: Result of the categorization of event topology among events surviving the SciFi-Bundle's brightness cut.

Ξ^- decay	2.2 %
$H \to \Sigma^- p$	0.8 %
two Λ's	0.1 %
single Λ	8.1 %
just kink	4.2 %
other	84.6 %

classified according to its topology into one of the categories, "Ξ^- decay", "$H \to \Sigma^- p$", "two Λ's", "single Λ", "just kink", or "other". The event topologies of the categories are listed in Fig. 3.14. The topology of "just kink" mainly corresponds to the decay of a Ξ^- hyperon accompanied with the invisible decay of $\Lambda \to n\pi^0$ or a Λ hyperon decaying outside the SciFi detectors. Events categorized to "Ξ^- decay" were rejected from the candidate events with a stopped Ξ^- hyperon in the emulsion. Second, we cut off events having the (K^-, K^+) reaction vertex downstream of the emulsion stack, by using track information viewed by the SciFi detectors as well as that measured by the spectrometer system. Then, each track other than those of kaons detected in the SciFi-Bundle was fitted in a straight line with the weight of brightness of each pixel. The fitting region was specified by a mouse pointer of a PC. If the fitted track clearly penetrated the emulsion, it was rejected.

The predictions of the positions and the angles of Ξ^- hyperons at entrance to the emulsion stack were made from the fitted track informations. Figure 3.15 shows an example of the eye-scanning and tracking in the SciFi detectors.

The result of the event selection using the image data from the SciFi detectors are given in Table 3.3. Figure 3.16 presents spectra of the z position of the (K^-, K^+) reaction, K^+ momentum, and missing mass and missing momentum of the $p(K^-, K^+)X$ reaction for events with Ξ^- hyperon candidate tracks detected in the SciFi-Bundle. The z vertex distribution shows that (K^-, K^+) reaction events occurred in the D-Block were rejected clearly. The result of the event categorization for events surviving the brightness cut of the SciFi-Bundle is listed
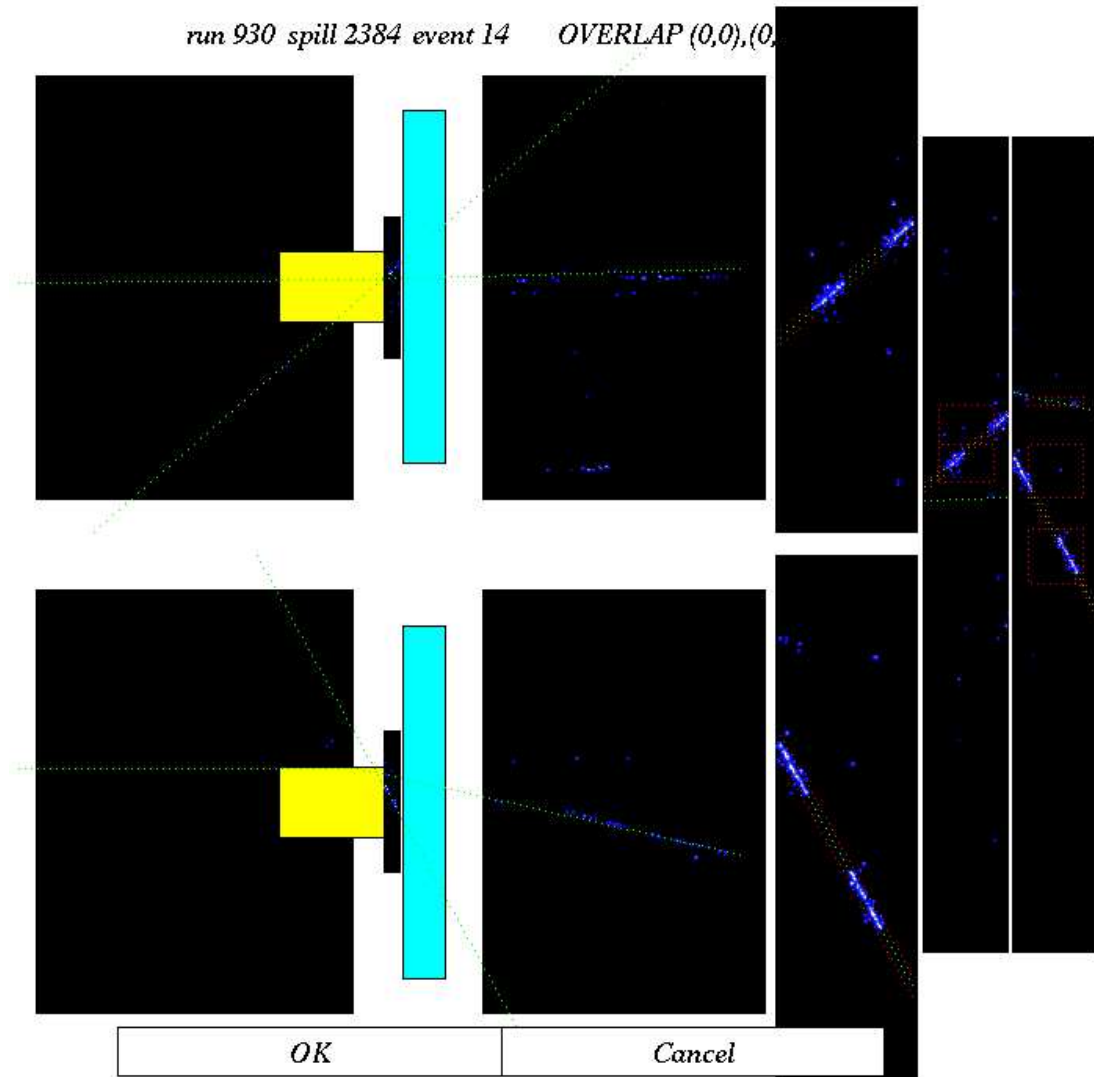
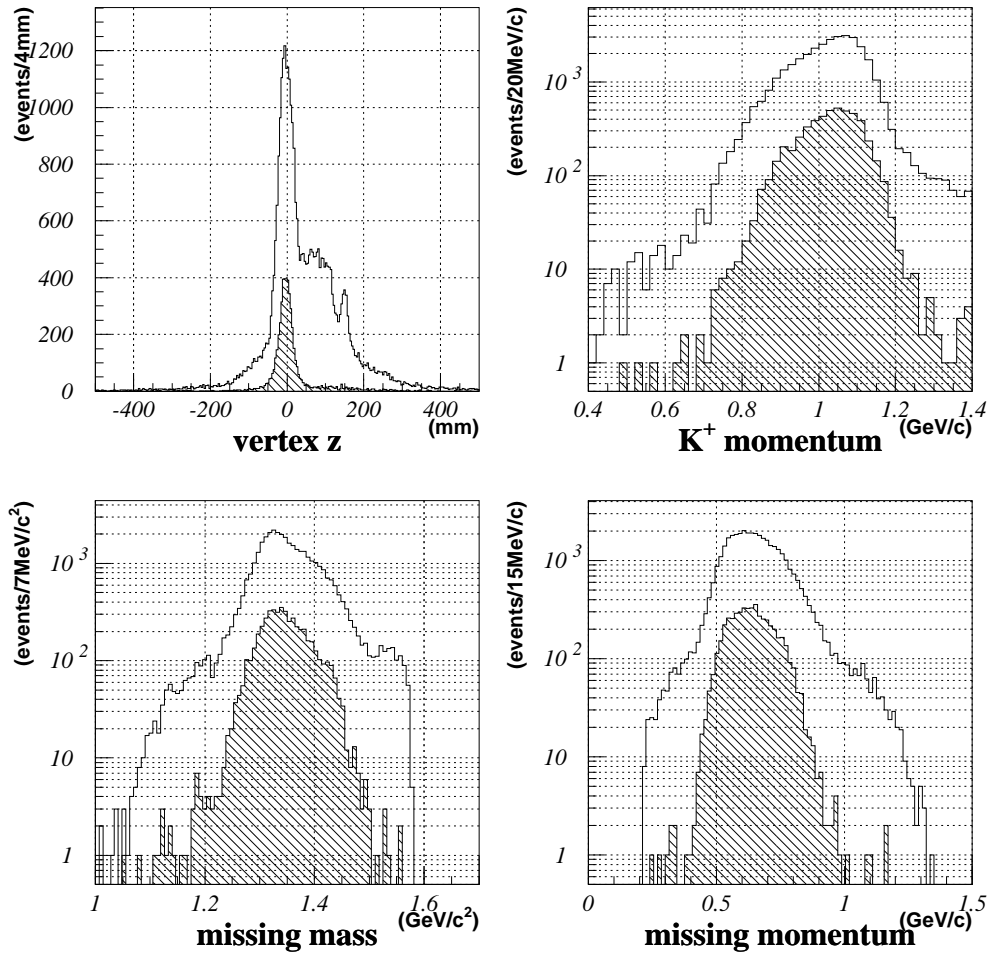Figure 3.15: Example of the SciFi event display for the eye-scanning and the tracking.

Figure 3.16: Spectra of the z position of the (K^-, K^+) reaction vertex, K^+ momentum, and missing mass and missing momentum of the $p(K^-, K^+)X$ reaction. The white and hatched area correspond to those before and after the event selection using the image data, respectively.

in Table 3.4. If the (K^-, K^+) reactions occurred in the diamond target or the emulsion, tracks near the vertices cannot be seen on the SciFi event display. Therefore, the category of "other" includes many Ξ^- hyperon decay events. The "$H \to \Sigma^- p$" events involves mis-identifications of the $\Lambda \to p\pi^-$ decay, where either the proton or pion scattered before stopping, or a particle was evaporated at the stopping point of the π^- meson. The number of events categorized to "two Λ's" was smaller than that obtained in the E224 experiment [60], because in events surviving the SciFi-Bundle's brightness cut, most of the (K^-, K^+) reactions occurred in the diamond target. The events, where a Ξ^- hyperon stopped in the emulsion and a Λ hyperon was detected in the SciFi detectors simultaneously, were candidates of the $\Lambda\Lambda \to \Lambda N$ decays of double-hypernuclei, and discussed in Chapter 5.

3.5   Automatic emulsion scanning

The emulsion analysis was carried out using a newly developed automatic-scanning system. Detailed description for the automatic-scanning system is presented in Ref. [61, 62].

3.5.1   System configuration

The system was controlled by a personal computer equipped with an image-processing board, motor-control board, parallel I/O board, and D/A board. The photograph and schematic configuration of the system are shown in Fig. 3.17. A microscope (NIKON L-mic NK35-2) has a stage which can move horizontally within a 350×350-mm^2 area with stepping motors (VEXTA UFK566B). The optical tube with object lenses is driven by a stepping motor (VEXTA UFK543B) in the vertical (focusing) direction. The stepping motors are controlled via motor drivers operated by a motor-control board (ADTEK aISA-M59) on the PC. The position is measured by linear encoders (HEIDENHAIN LS703/704). The signals from the encoders are digitized by HEIDENHAIN EXE602E/610C, and read by a parallel I/O board (ADTEK a ISA-P54W) on the PC. The pictures from a CCD camera (HAMAMATSU C3077) are digitized in 8-bit depth by a image-processing board (HITACHI IP5000). An object lens with the magnification of 50 (TIYODA) is mainly used for track scanning. The voltage of a power supply of a light source is controlled by the analog signal output from a D/A board (JDS ACL-6128).

3.5.2   Position calibration

Distortion of emulsion plate

An emulsion plate is shrunk and distorted during the development process. The shrinkage factor in the vertical (focusing) direction can be estimated from the
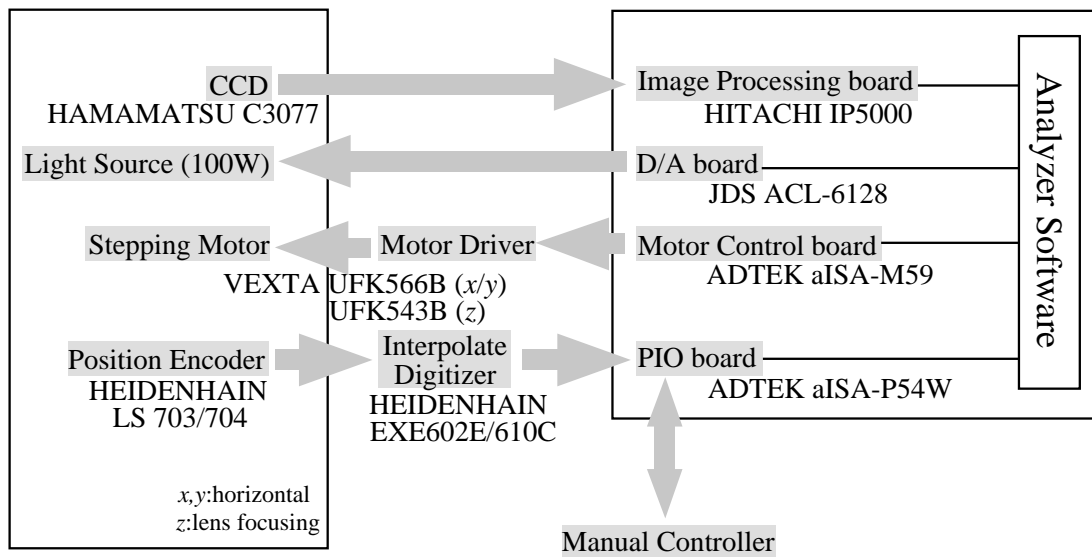
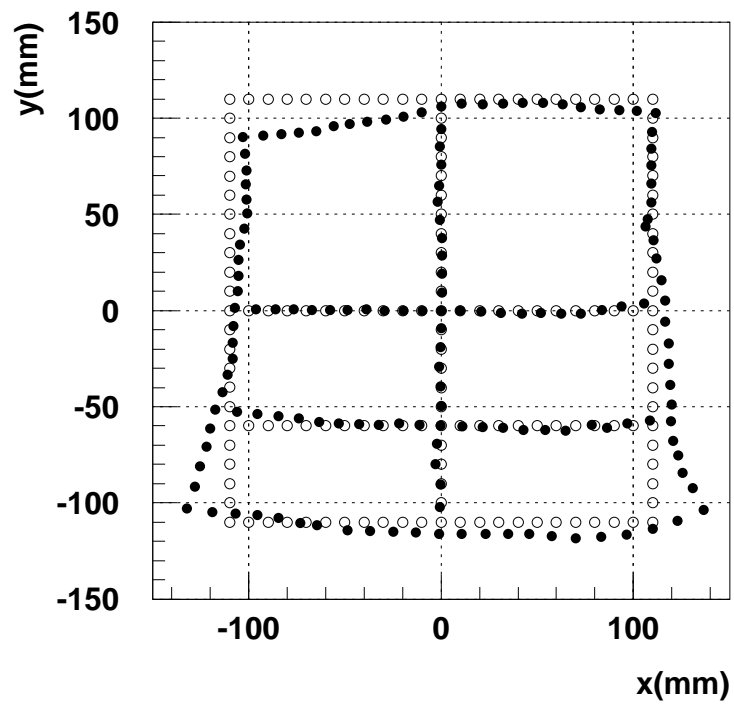Figure 3.17: Photograph and schematic configuration of the microscope system.

Figure 3.18: Distortion of a thick-type emulsion plate. The white circles indicate original positions of the grid pattern, and black circles present those after the development of emulsion. The displacements from the original positions are scaled by 100 times so that they can be seen clearly.

thickness of the plate at the exposure time and that at the measurement time. The distortion in the horizontal direction is corrected by measuring the positions of grid marks of about 60 $\mu\mathrm{m}^\phi$, which are printed in grid pattern with 10 mm pitch after the beam exposure. Figure 3.18 shows how an emulsion plate was distorted after the development. Before scanning each track, its horizontal position was corrected by measuring the position of the nearest grid mark.

Position relative to the SciFi-Bundle

It is a key point for the E373 experiment to connect tracks of Ξ^- hyperons from the SciFi-Bundle to the emulsion plate correctly. In order to correct relative positions of the emulsion stack and the SciFi-Bundle, X-ray was irradiated through the SciFi-Bundle to each emulsion stack. The X-ray from a generator of 70 kV and 15 mA was irradiated for 0.15 seconds at four corners of the emulsion stack. It was collimated with a tungsten plate with three 200-$\mu\mathrm{m}^\phi$ holes at 5-mm horizontal intervals. In '98 run, X-ray was applied once at each corner of the emulsion stack, while in 2000 run, irradiated at two positions of each corner, i.e., totally at eight positions.

In the off-line analysis, the position of the central mark of the three collimated X-ray marks was measured at each corner of the emulsion plate. Correction parameters, such as a center position, a rotation angle, and a shrinkage factor, the relative positions of the grid marks on the emulsion plate and the SciFi-Bundle detector were determined from the measurements on the emulsion plate and the SciFi-Bundle.

Detailed description about the precision of the connection from the SciFi-Bundle to the emulsion is presented in Sec. 3.5.3.

Relative positions of two plates

As for the first and second emulsion plates, their relative positions were also determined using the X-ray marks at four corners. Since the X-ray was totally absorbed up to the second plate, the positions of further downstream plates were corrected using straight tracks of charged particles passing through both of the two plates.

The correction was made by specifying some "reference tracks" manually on an upstream plate and searching for them automatically on the downstream plate. First, three tracks were searched at each of four corners of an upstream plate manually. Then, the reference tracks were searched for on the next plate at four corners automatically, where the position relation of the three tracks were used to identify the reference track among candidates.

3.5.3 Automatic scanning in thin emulsion

Tracks of Ξ^- hyperons were searched for in the thin-type emulsion plates automatically, using the positions and angles predicted by the SciFi-Bundle detector.

Take pictures at different z(focusing) position.
(z : pependicular to the emulsion plate)

emulsion bulk

images

shift each image by ($-\Delta x$, $-\Delta y$)

$$\Delta x = \frac{dx}{dz} \times \Delta z$$

$$\Delta y = \frac{dy}{dz} \times \Delta z$$

$\frac{dx}{dz}, \frac{dy}{dz}$: predicted angles

Δz : step size of z position

Δz

Δy
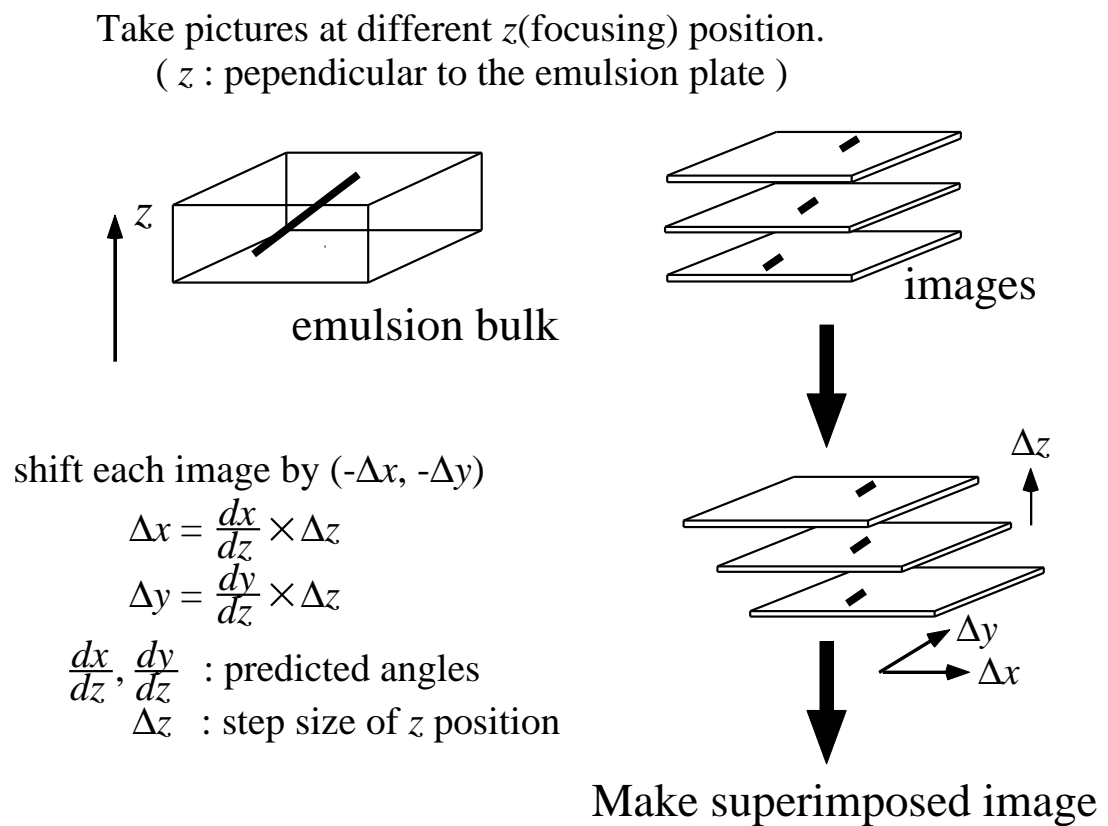
Δx

Make superimposed image

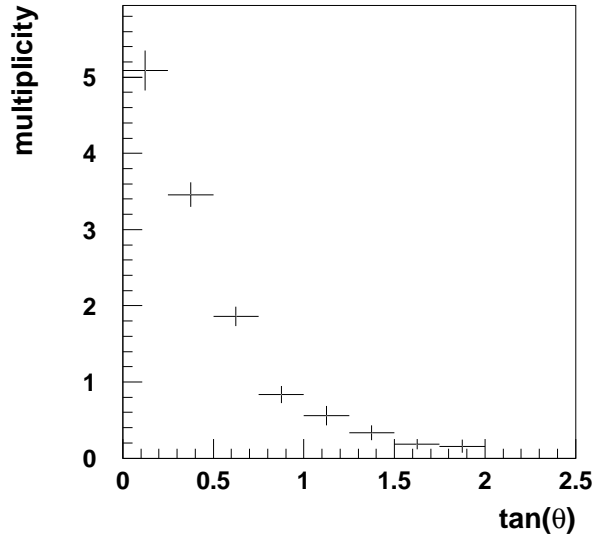Figure 3.19: Basic idea of the automatic track-finding.

Figure 3.20: Multiplicity distribution of candidate tracks found in the thin-type emulsion plates.

The algorithm for finding tracks is basically same to that proposed by Nagoya group [63]. Figure 3.19 illustrates the algorithm. Since the focusing depth of the microscope is about 3 μm, only a currently focused tomogram of about 3 μm in thickness of an emulsion plate can be obtained as a picture from the microscope. Tomographic pictures at eight different depths of the emulsion plate are taken by changing the focal plane of the object lens. When those pictures are shifted by some offset values (Δx and Δy) to keep the image of the track at the same position, and they are integrated to an accumulated image, only tracks with a same angle as predicted make sharp peaks in the accumulated image. Here, the offset values for each tomographic picture are calculated from the predicted angle and its depth in the emulsion. The track having the predicted angle can be found by searching for such peaks.

A Ξ^- hyperon track was searched for in 900 $\times$ 900-μm^2 area typically around the predicted position in the thin-type emulsion plate. The searched area was slightly changed depending on the track angle. It was divided into regions with the size of the field of view of the microscope ($\sim$ 110 $\times$ 90 μm^2). The predicted angle was corrected with the position of the searching region as follows;

$$\left(\frac{dx}{dz}\big|_{pred} + \frac{x_0 - x_{pred}}{L}, \quad \frac{dy}{dz}\big|_{pred} + \frac{y_0 - y_{pred}}{L} \right). \qquad (3.3)$$

Here (x_{pred}, y_{pred}) and ($\frac{dx}{dz}\big|_{pred}$, $\frac{dy}{dz}\big|_{pred}$) denote the positions and angles predicted from the data of the SciFi-Bundle, respectively, and (x_0, y_0) represent the center position of the searching region. The parameter L is the distance between the SciFi-Bundle and the thin-type emulsion plate, and is 2.2 mm for '98 run and 3.1

mm for 2000 run. The searching angle region ($\tan\theta$) was ± 0.1 around the above angle. Tracks having the predicted angle were searched for in the emulsion gel of the upstream side of the plate at each region with the automatic track-finding method. Once a track was found in the upstream gel, a track with a same angle was searched for at the corresponding position in the downstream-side gel. If a track was found both in the upstream-side gel and in the downstream-side gel, it was accepted as a track candidate. More than one candidate track can be found for each prediction by the SciFi-Bundle. The multiplicity of track candidates for various prediction angles is presented in Fig. 3.20. All of the candidate tracks were traced in the thick-type emulsion plates semi-automatically.

The condition of the search, such as searched area and angle region, was determined by connecting sample tracks from the SciFi-Bundle to the emulsion. For 2000 run, the connection between the SciFi-Bundle and the emulsion was studied with module#60, which was exposed to K^- beam with the lower track density than those of the other stacks. Events with only one thick track detected in the SciFi-Bundle with the angle of $0.4 < \tan\theta < 1.0$ were selected by eye scanning as samples for the connection study. The overlap of the SciFi images was not a matter for the study, because the images were acquired in half-overlap mode in 2000 run, and the overlap could be resolved by the off-line analysis. The 51 track samples were searched for in the thin-type emulsion of module#60 in the manner described above. In order to estimate the background, "dummy scan" was performed where the searched positions were shifted from the predictions by 3 mm. Figure 3.21 shows the results of the scanning for the sample tracks as well as the dummy scan. Figure 3.22 shows the position differences corrected with the angle differences ($\Delta\frac{dx}{dz}$, $\Delta\frac{dy}{dz}$),

$$\left(\Delta x - L \times \Delta\frac{dx}{dz}, \ \ \Delta y - L \times \Delta\frac{dy}{dz} \right), \tag{3.4}$$

which represents the predicted positions are shifted due to the error of the angle prediction. The large enhancements are clearly seen above the background distribution. The number of the tracks found in the emulsion was 80, whereas for the dummy scan the track number was 35.

The study of the connection for 1998 run was reported in Ref. [61].

3.5.4   Semi-automatic scanning in thick emulsion

Since tracks of low-momentum Ξ^- hyperons are deflected by the multiple scattering, the efficiency of the automatic track-finding system is not sufficiently high in thick-type emulsion plates. The scanning result was, therefore, checked individually by human eyes. Thus, we called the scanning method for thick-type emulsion as "semi-automatic".

In tracing a track in thick-type emulsion plates, each side gel was divided to two or three layers, depending on the track angle. A track having a same angle was searched for at the corresponding position in each of the layers. The
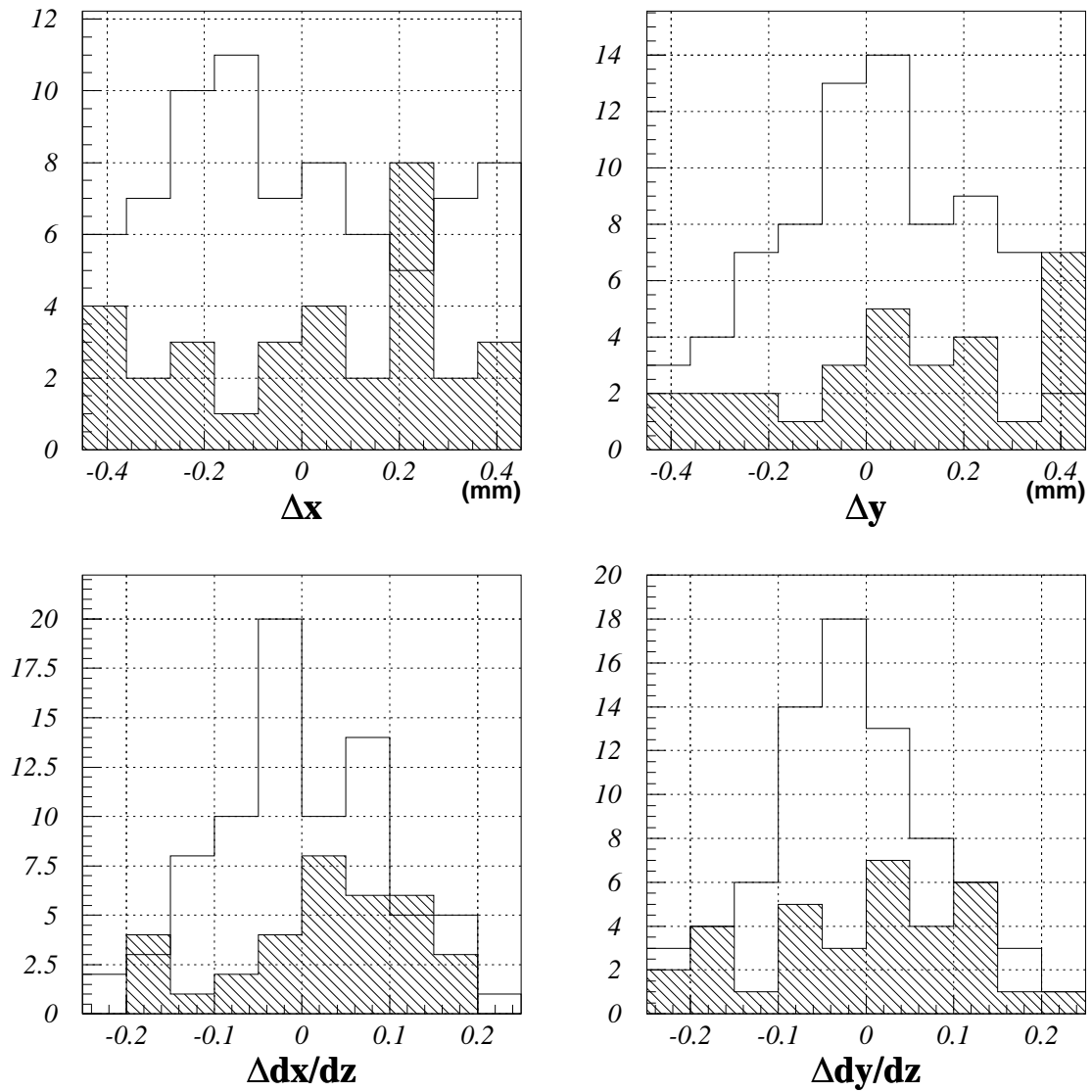
Figure 3.21: Differences of positions (Δx, Δy) and angles ($\Delta \frac{dx}{dz}$, $\Delta \frac{dy}{dz}$) between the found tracks and the prediction. Hatched areas correspond to those obtained from the dummy scan.
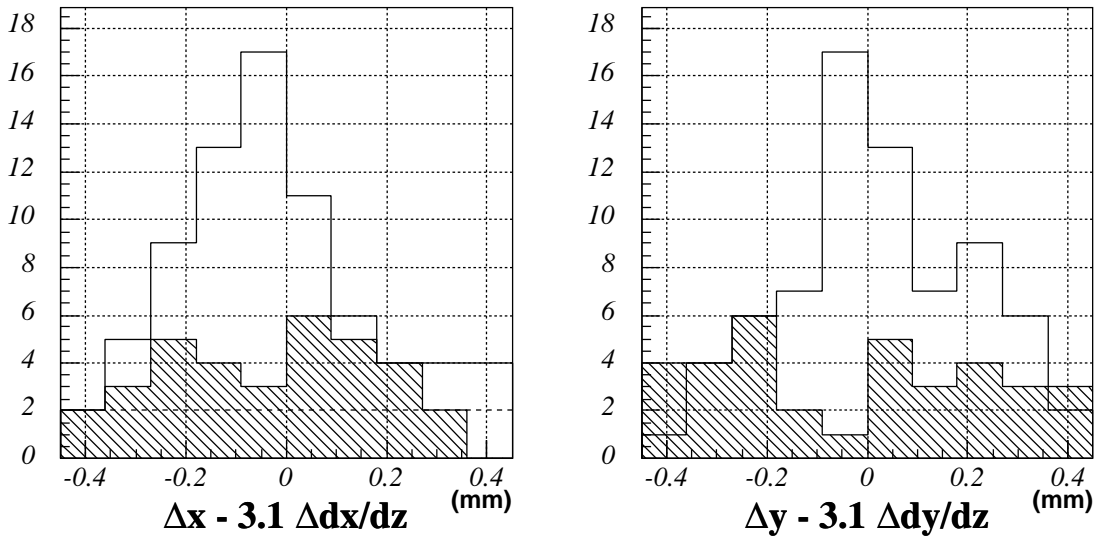
Figure 3.22: Corrected position differences of the found tracks from the prediction. Hatched areas correspond to those obtained from the dummy scan.

search was performed in 100×100-μm^2 area around the expected position and angle region ($\tan \theta$) of ± 0.06 around previously measured. The efficiency of the automatic track finding at each layer was 90 % on average. The result of the scanning in each layer was checked by human eyes, and in case it failed, the track position was specified manually.

3.5.5   Event categorization

After a track was traced to a vertex or the last plate of the emulsion stack, it was categorized to one of the following types according to its topology.

- σ-stop : The particle of the traced track comes to rest, from which at least one charged-particle track (prong) is emitted. Whether the particle has stopped or interacted in-flight is discriminated by the thickness and deflection of the track near the vertex, because multiple scattering of a particle becomes larger near stopping.

- ρ-stop : No evaporation track from the stopping point. This is also a candidate for Ξ^- hyperon capture event, but it cannot be distinguished from a stopped proton if no Auger electron is emitted from the stopping point.

- decay : The particle of the traced track decays into a thin track (π^-) and a invisible neutral particle.

- beam interaction : A beam particle interacts with emulsion nuclei. A beam track can be recognized as a thin track almost perpendicular to the emulsion

Table 3.5: Result of the categorization of the vertices found in emulsion.

event	5096
predicted track	7340
track found in emulsion	11512
σ-stop	329
ρ-stop	4752
decay	275
secondary interaction	694
beam interaction	1262
other	46
through	3671
clean σ-stop	237
clean σ-stop (thick)	204
clean decay	245
hyperfragment candidate	51

plate. If such a thin track is observed upstream of the reaction vertex but not downstream of it, the event is interpreted as "beam interaction".

- secondary interaction : If a straight track reaches the reaction vertex which has no beam track upstream, the event is categorized to "secondary interaction", in-flight interaction with emulsion nuclei. If a thick and deflected track accompanies the vertex, it could be σ-stop of a Ξ^- hyperon produced via the (K^-, K^+) reaction in the emulsion stack. In that case, the traced track is one of the fragment emitted from the Ξ^- hyperon capture point or decay of hypernuclei.

- other : Other than above categories. For example, if a traced track scattered upstream, it cannot be scanned further automatically.

- through : The traced track escaped from the emulsion stack without interacting or decaying in the emulsion.

The result of the scanning of about 32 % of total emulsion is summarized in Table 3.5. In current stage of the analysis, one event may be categorized to more than one type if its vertex type was not clearly determined. The events uniquely identified as σ-stop are referred to as "clean σ-stop" in the table, and those uniquely identified as decay are denoted by "clean decay". The small yield of the decay events does not mean the small number of Ξ^- hyperons production, because the events accompanied with a low-momentum Ξ^- hyperon were enhanced via the event selection using the SciFi detectors. The category of "clean σ-stop" includes the backgrounds due to stopped π^- mesons. The item of "clean σ-stop

(thick)" represents the number of thick tracks among the "clean σ-stop" events. From a Monte-Carlo simulation, the expected number of stopped-Ξ^- events for the scanned emulsion is about 320. According to the result of E176 [64], the ratio of σ-stop / ρ-stop of Ξ^- hyperon captures at rest is about 2/3. Therefore, the expected number of the events accompanied with σ-stop of a Ξ^- hyperon is 213, which is consistent with the number of the events of "clean σ-stop (thick)". The number of Ξ^- hyperon capture events and their background are discussed in detail in Chapter 5. In the E176 experiment, 11 hyperfragment events were found among the 78 stopped-Ξ^--hyperon events [64]. The number of "hyperfragment candidate" events is consistent with the E176 result.

Among the "hyperfragment candidate" events, two twin-hypernuclei events and three double-hypernucleus events have been found. The first double-hypernucleus event found in E373 was described in Ref. [61, 65], and the detailed description for the second is presented in Chapter 4. The analysis of the third double-hypernucleus is now in progress. One of the two twin-hypernuclei events was reported in Ref. [66, 61], and the other is described in detail in Appendix B.

3.6   Range-energy relation in emulsion

Event reconstruction in emulsion is based on the conservation laws of energy and momentum, and the masses of hypernuclei are calculated from the energies of their decay daughters. Since the kinetic energy of a charged particle is obtained by measuring its range, the range-energy relation in emulsion is quite important for emulsion analysis.

3.6.1   Calculation of range-energy relation

Energies of charged particles were calculated with SRIM2000 [67] from their ranges in the emulsion, except for pions which are not supported in SRIM2000.

Energies of pions were obtained from a traditionally-used range-energy formula in emulsion [68], where a range, R, of a particle with charge of Z and mass of M in units of the proton mass is expressed as

$$R = R_{obs} - R_c = \rho \left[\frac{M}{Z^2} \cdot \lambda(\beta) + R_{ext} \right]. \tag{3.5}$$

Here R_{obs} denotes a measured range, and R_c is a range correction of track end and usually taken to be a half of mean diameter of developed grains. The quantity ρ is a factor required to adjust the ranges measured in emulsion to their equivalents in standard emulsion (Ilford G5 emulsion with density of 3.815 g/cm^3). R_{ext} stands for the effect of electrons captured by the positive charged ions, and is given by

$$R_{ext} = M Z^{2/3} C_Z (\beta/Z), \tag{3.6}$$

where C_Z is a unique function of β/Z, independent of the species of the incident particle [68]. $\lambda(\beta)$ represents the range of a proton at velocity β, and is expressed

as [69]

$$\frac{\lambda_s}{\lambda} = \frac{rd - 1}{rd_s - 1} + \frac{r(d_s - d)}{rd_s - 1} \cdot \frac{\lambda_s}{\lambda_w},\tag{3.7}$$

where d is the emulsion density, d_s denotes the density of standard emulsion, λ_s and λ_w are the proton range in standard emulsion and water, respectively. The factor r stands for the ratio of the volume increment in cubic centimeters to the weight increment in grams brought by the addition of moisture to emulsion, and was set to 1.0 in our analysis.

3.6.2 Calibration of range-energy relation

The range-energy relation was calibrated using the alpha decays of thorium series and uranium series in the emulsion. The decay chains of thorium series and uranium series are shown in Fig. 3.23 and Fig. 3.24, respectively. Since the time between the pouring and the development of the emulsion was in the range from several months to a year, five alpha decays from ^{228}Th were observed in the decay chain of thorium series. Among the five α particles, the α from ^{212}Po has a separately higher energy than the others, and, therefore, has a longer range. The α from ^{228}Th is observed in a little distance from the others, because ^{224}Ra may move thermically in its life time of 3.66 days. Hence, the five alpha decays from thorium series are observed in emulsion as a 5-prong star in which one track is longer than the others and another one is distant from the others, as shown in Fig. 3.25 (a). The α particles from ^{212}Po and ^{228}Th, therefore, can be identified and were used for the calibration of the range-energy relation. On the other hand, a 4-prong star can be observed from the decay chain of uranium series, as presented in Fig. 3.25 (b). Among the four tracks of α particles, an α track from ^{214}Po is longer than the others because of its relatively high energy, and another one from ^{226}Ra is distant from the others due to the relatively long life time of ^{222}Rn. Thus, the α particles from ^{214}Po and ^{226}Ra can be also identified and were used for the range-energy calibration.

Figure 3.26 shows the range distribution of α particles from the decay of ^{212}Po in the plate#12 of stack#17, where a double-hypernucleus event, mentioned in detail in the next chapter, was found. It is expressed as the squared length in the focusing direction, Δz^2, versus the squared length in the direction perpendicular to it, $\Delta x^2 + \Delta y^2$. The range of the α particles, R, is given by

$$R = \sqrt{\Delta x^2 + \Delta y^2 + (s \cdot \Delta z)^2},\tag{3.8}$$

where s represents the shrinkage factor in the focusing direction of the emulsion plate, defined as the ratio of the thickness of the gel at exposure time and that at measurement. By fitting the data points in Fig. 3.26 with a straight line, we obtained the range of α particles as well as the shrinkage factor. For instance, in the emulsion in which the double-hypernucleus event described in the next chapter was observed, the range of α particles from ^{228}Th was 22.9 ± 0.3 μm. Using the
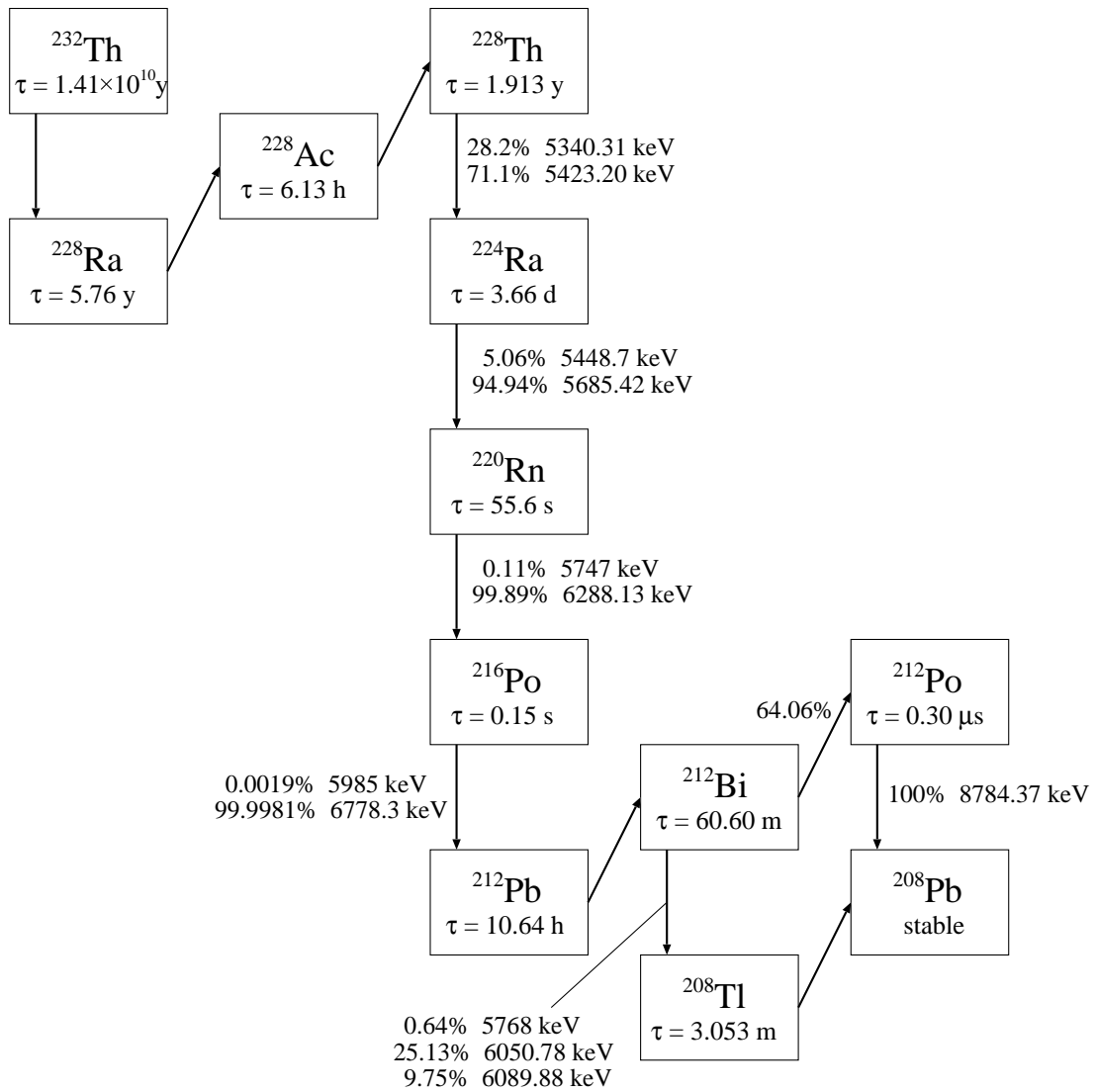
Figure 3.23: Decay chain of thorium series.

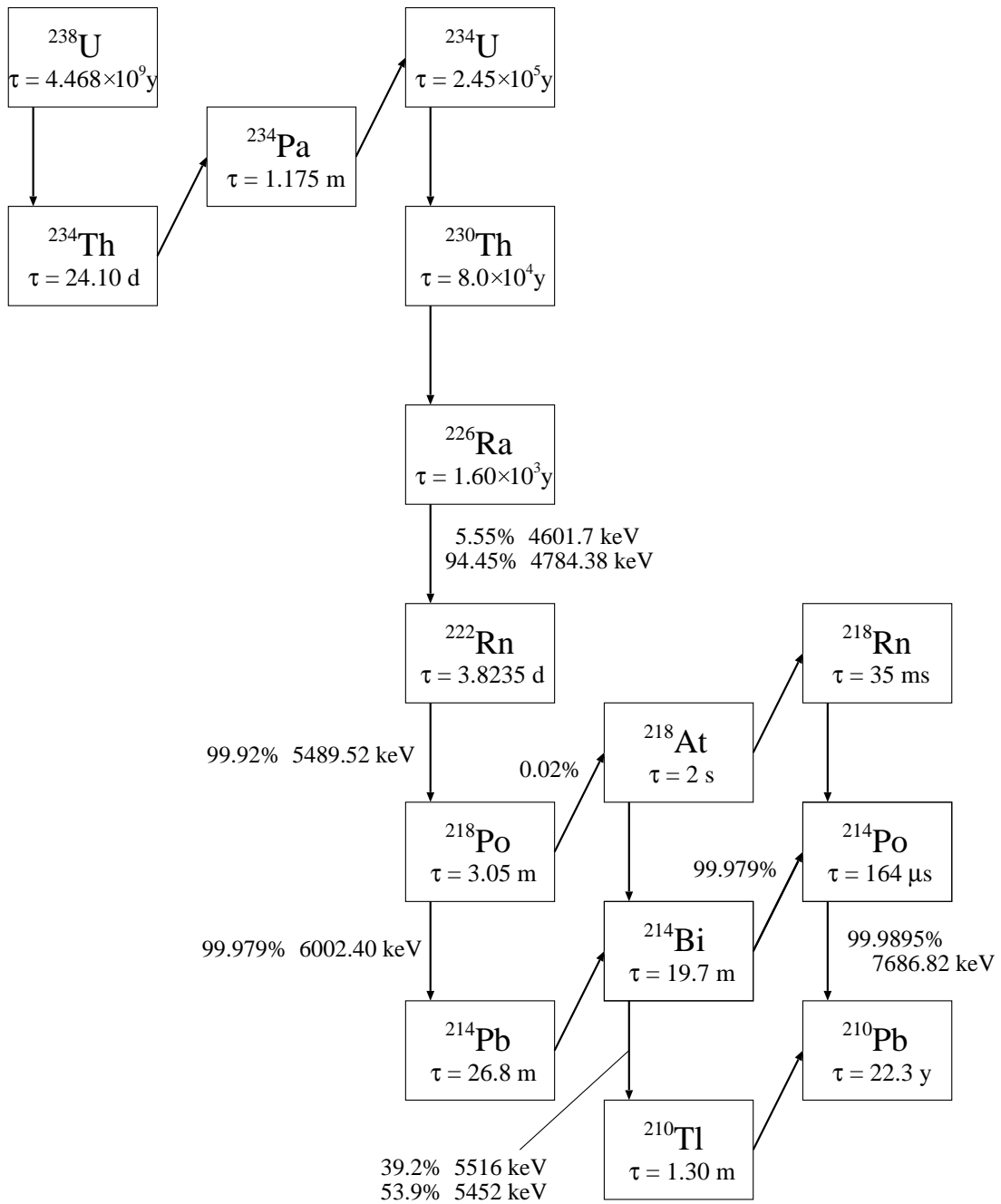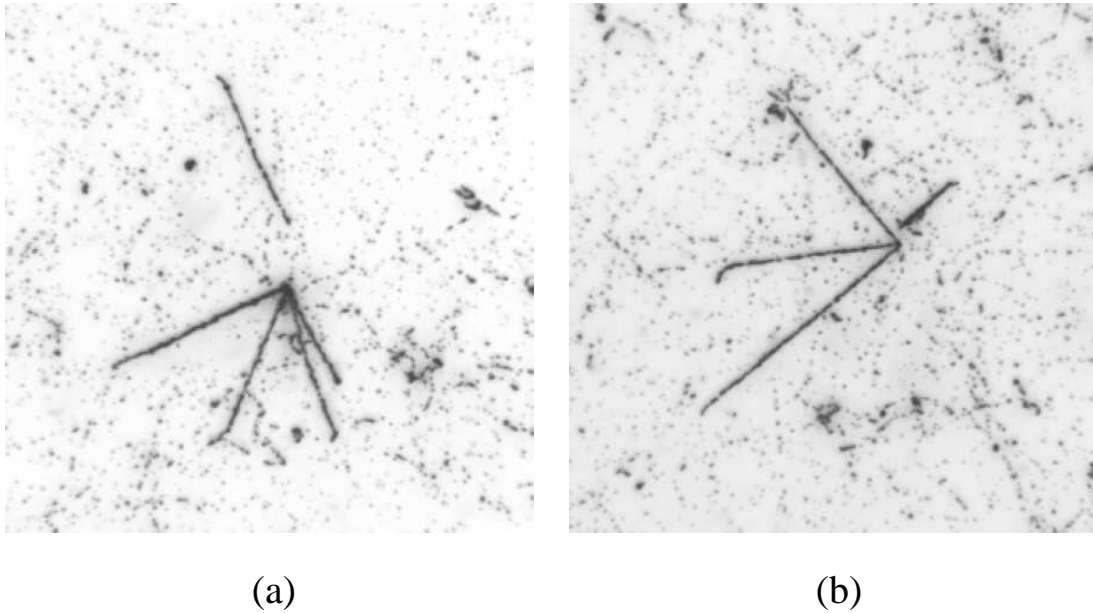Figure 3.24: Decay chain of uranium series.

(a)   (b)

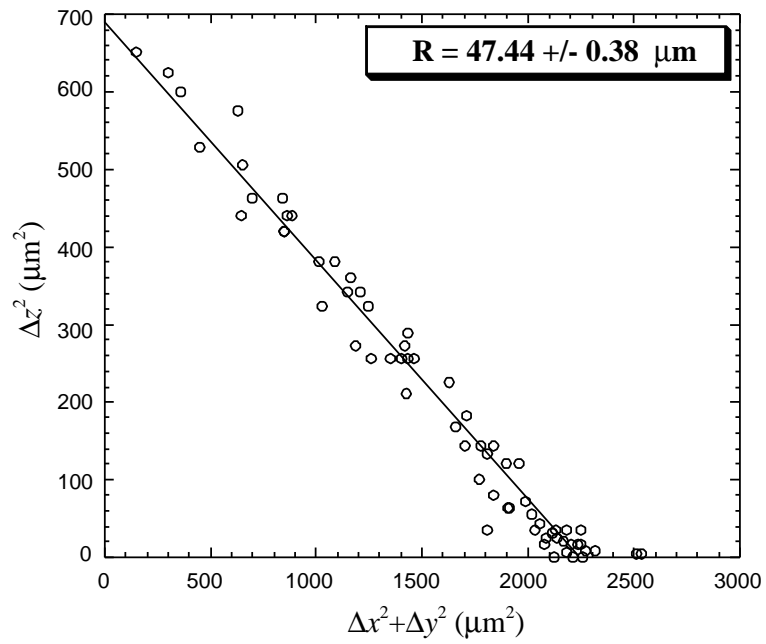Figure 3.25: Photographs of alpha decays of (a) thorium series and (b) uranium series.

Figure 3.26: Range distribution of α particles from the decay of ^{212}Po.

average kinetic energy of α particles from ^{228}Th of 5.400 MeV, the density of the emulsion was calculated with SRIM2000 to be 3.624 ± 0.048 g/cm^3. That from ^{212}Po was obtained as 47.4 ± 0.4 μm, giving the emulsion density of 3.615 ± 0.034 g/cm^3. The density of the emulsion gel on the plate was determined as the mean of them, 3.619 ± 0.025 g/cm^3. This is consistent with the measurement value of 3.660 ± 0.149 g/cm^3, which was obtained from the measured weight and thickness of the emulsion plate. The detailed description of the method to estimate the emulsion density from its weight and thickness is given in Ref. [70].

3.6.3 Energy error

The error of the kinetic energy calculated from the range comes from the errors in the range measurement, the range-energy relation, and the range straggling.

The measurement error of one position was estimated by measuring the position of a same grain many times. It was found that the r.m.s. error of one position measurement is 0.25 μm in the horizontal direction. In the vertical (focusing) direction, since the minimum step of the movement is 0.5 μm, the r.m.s. error of $0.5/\sqrt{12}$ μm was taken additional to the error of 0.25 μm. If more than two charged fragments are emitted from a vertex, the position of the vertex can be determined more precisely by fitting the tracks of the fragments. The measurement error of the range of a track was calculated from these positioning errors. In the vertical direction, the error of the shrinkage factor also contributes to the range error. The shrinkage factor was obtained from the ratio of the thicknesses of the plate at the exposure time and that at the measurement. The r.m.s. error on the shrinkage factor was 1.7 % due to the error on the thickness measurement.

The contribution by the error on the range-energy relation was less than 1 % in energy after the calibration described above.

The range straggling, ΔR, of a particle was calculated using the relation [71, 72],

$$\Delta R(T) = \frac{\sqrt{M}}{Z^2} \cdot \Delta R_p \left(\frac{T}{M} \right) \tag{3.9}$$

where Z, M, and T denote a charge, a mass in units of the proton mass, and a kinetic energy of the particle, respectively. ΔR_p represents the range straggling of proton, and its percentage to the proton range in emulsion was calculated by W.H. Barkas *et al.* [72] using the following relativistic formula;

$$(\Delta R)^2 = 4\pi n_e Z^2 e^4 \int_0^T \frac{(1 - \beta^2/2)}{(1 - \beta^2)\langle dE/dR \rangle^3} dE, \tag{3.10}$$

where n_e is the electron density in the stopping material, $\langle dE/dR \rangle$ is the mean rate of energy loss, and e is the elementary charge.

Chapter 4

Observation of Lambpha

Although we have analyzed only 32 % of the total emulsion, we have found three examples of a sequentially decaying double-hypernucleus and two events accompanied with twin hypernuclei emission from a Ξ^- hyperon capture at rest. In this chapter, the detail of the analysis of the second double-hypernucleus event was presented together with the comparison of the result with the past experiments. The description and analysis of the first double-hypernucleus event and the first twin hypernuclei event were given in Ref. [65, 61] and in Ref. [66, 61], respectively. The analysis of the third double-hypernucleus event is now under way. The second twin hypernuclei event is described in Appendix B.

4.1 Event description

A photograph and schematic drawing of the event are shown in Fig. 4.1. We named this event "Nagara". A Ξ^- hyperon came to rest at point A, from which three charged particles (track#1, #3, and #4) were emitted. One of them decayed into a π^- meson (track#6) and two other charged particles (track#2, #5) at point B. The particle of track#2 decayed again to two charged particles (track#7, #8) at point C.

The measured lengths and emission angles of these tracks are summarized in Table 4.1. The event was detected in the most downstream plate (#12) of the emulsion stack. The particle of track#7 left the emulsion stack and entered the D-Block. Track#5 ended in a 50-μm-thick acrylic base film. The particle of track#8 was scattered by about 90 degree in plate#10 and stopped in plate#11. When we define the coplanarity of three tracks from point A, c_A, as

$$c_A = (\boldsymbol{v_3} \times \boldsymbol{v_4}) \cdot \boldsymbol{v_1},$$

where $\boldsymbol{v_1}$, $\boldsymbol{v_3}$, and $\boldsymbol{v_4}$ are the unit direction vectors of track#1, #3, and #4, respectively, the value of c_A is -0.005 ± 0.028. This means that three tracks emitted from point A are coplanar within the error. For the coplanarity of three tracks from point B, c_B, defined as

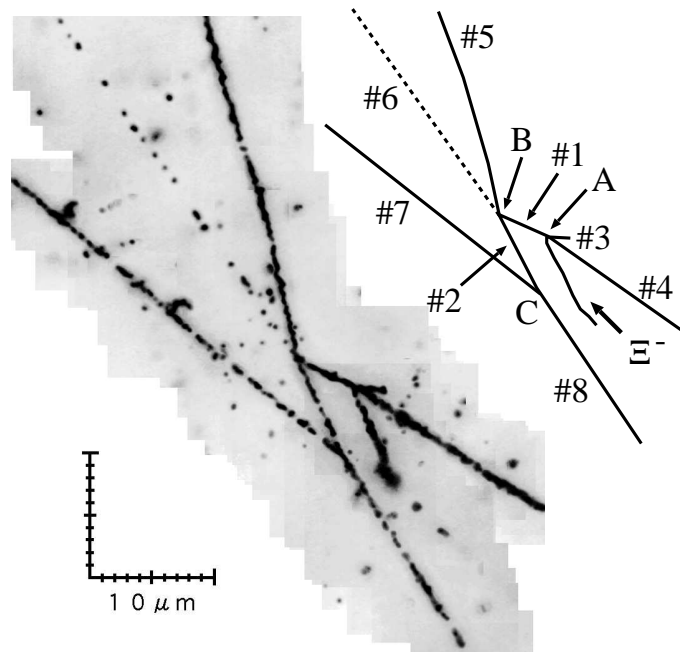$$c_B = (\boldsymbol{v_5} \times \boldsymbol{v_6}) \cdot \boldsymbol{v_2},$$

Figure 4.1: Photograph and schematic drawing of Nagara event. See text for detailed explanation.

the value is 0.0002 ± 0.0137. Therefore, three tracks from point B are also coplanar.

Figure 4.2 shows the image of the SciFi-Block detectors. The track of the incident K^- meson cannot be seen because it passed through the center hole of the U-Block and reached the diamond target. It is clearly recognized that one charged particle was emitted from the emulsion and stopped in the D-Block. The position and direction of this track was well consistent with the measurement of the track#7 in the emulsion plate. This image was overlapped with that of the previous triggered event, and then additional one track of the previous event was found in the D-Block. (This was confirmed using the spectrometer data of the previous event.) The range of track#7 in the D-Block was 13.1 mm. The mean brightness near the stopping point of track#7 is 2100. Comparing with the brightness distribution of stopping pions and protons in the D-Block (Fig. 3.10), the particle of track#7 cannot be interpreted as a π^- meson. If the particle of track#7 is assumed to be a proton, its kinetic energy is 47.3 ± 1.4 MeV.

4.2 Event reconstructon

The single-hypernucleus (track#2) was identified from event reconstruction of its decay at point C. Mesonic decay modes of single-hypernuclei were rejected because their Q-values are too small. The decay mode of the single-hypernucleus
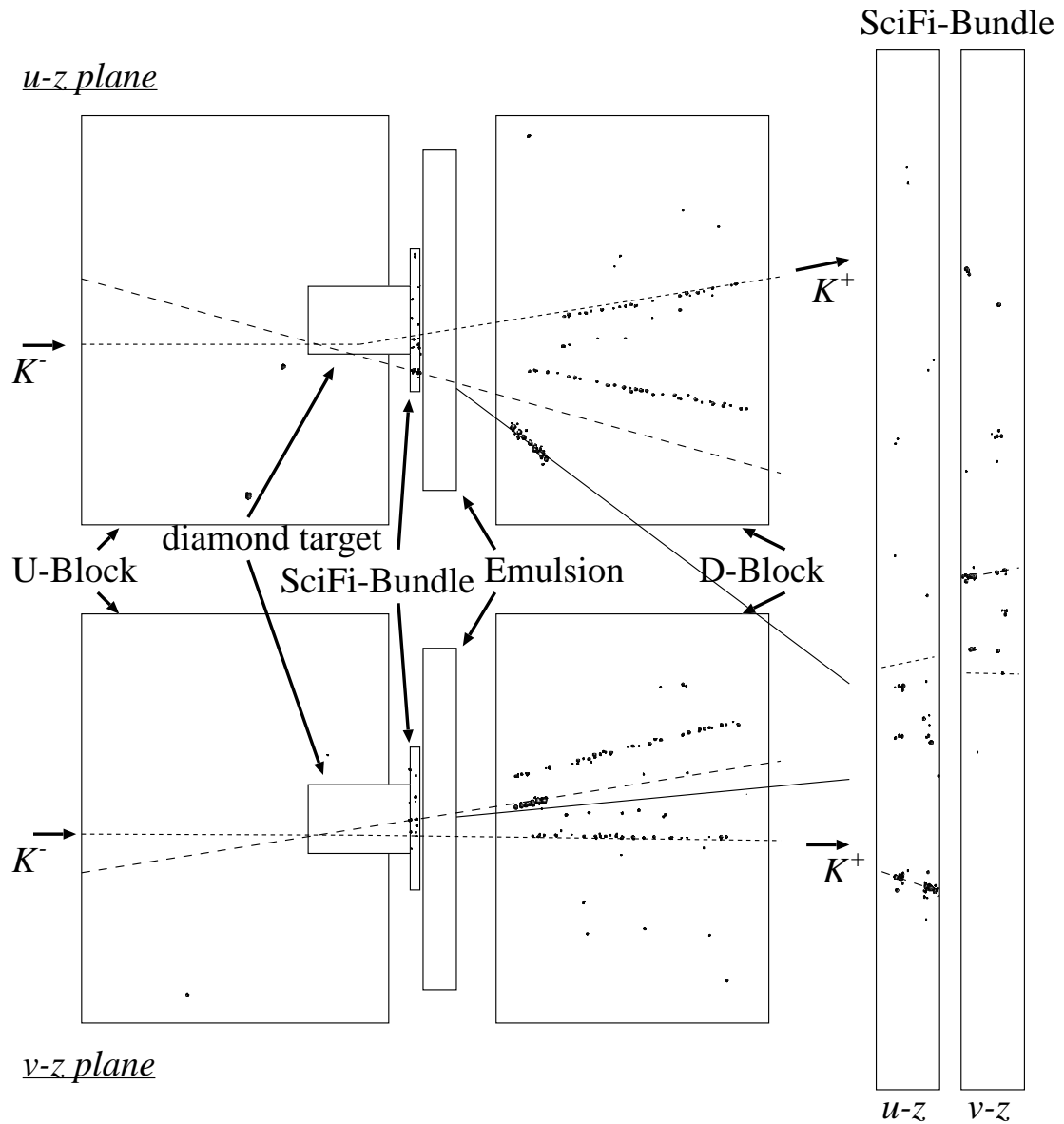
Figure 4.2: Image of the SciFi detectors of the Nagara event. The dot line indicates the tracks of the incident K^- and scattered K^+ mesons measured with the spectrometer system. The dashed line is the Ξ^- hyperon track measured with the SciFi-Bundle detector. The solid line is the extrapolated line using the position and angle information of track#7 in the emulsion stack.

Table 4.1: Lengths and emission angles of the tracks. Angles are expressed by a zenith angle (θ) with respect to the direction perpendicular to the plate and an azimuthal angle (ϕ). The indicated errors are the measurement errors only. For track#4, #6, #7, and #8, the ranges in an acrylic base were converted to those in emulsion. The lengths of track#5 and #7 are the visible ones in the emulsion only. The length of track#7 inside the D-Block is 13.1 mm.

point	track#	length [μm]	θ [degree]	ϕ [degree]	
A	#1	8.1 ± 0.3	44.9 ± 2.0	337.5 ± 1.8	double-hypernucleus
	#3	3.2 ± 0.4	57.7 ± 5.2	174.9 ± 2.9	
	#4	88.3 ± 0.5	156.2 ± 0.5	143.0 ± 1.0	
B	#2	9.1 ± 0.3	77.7 ± 1.6	115.9 ± 0.8	single-hypernucleus
	#5	82.1 ± 0.6	122.8 ± 1.0	284.2 ± 0.7	stopped in base
	#6	13697	81.1 ± 0.8	305.5 ± 0.1	π^-
C	#7	742.6 ± 0.6	138.5 ± 0.2	322.1 ± 0.3	stopped in D-Block
	#8	5868 ± 20	52.2 ± 1.2	123.7 ± 0.7	scattered before stopping

is non-mesonic with neutron emission. If either track#7 or #8 has more than unit charge, the total kinetic energy of the two charged particles is much larger than the Q-value of any possible decay mode because of the long ranges of track#7 and #8. Therefore, both track#7 and #8 are singly charged, and only $_\Lambda$He isotopes are acceptable for the single-hypernucleus.

The kinematics of all possible decay modes of the double-hypernucleus (track#1) which decays into $_\Lambda$He (track#2) and π^- (track#6) were checked, and $B_{\Lambda\Lambda}$ and $\Delta B_{\Lambda\Lambda}$ were calculated. Since track#5 ended in the base film, only the lower limit of the kinetic energy can be determined. For the decay modes without neutron emission, the range of the particle of track#5 was increased to minimize the missing momentum. If the sum of the momenta of the three charged particles (track#2, #5, and #6) deviated from zero by more than 3 standard deviations even after the range of track#5 was increased from the missing momentum, that decay mode was rejected. For the decay modes with neutron emission, the upper limits of $B_{\Lambda\Lambda}$ and $\Delta B_{\Lambda\Lambda}$ were obtained. Only the results for $\Delta B_{\Lambda\Lambda} > -20$ MeV are listed in Table 4.2. The cases of double-hypernuclei with more than two units of charge are not given because their values of $\Delta B_{\Lambda\Lambda}$ were less than -20 MeV.

Kinematical analysis of the production reaction was made by assuming the Ξ^- hyperon was captured by a light nucleus in the emulsion (^{12}C, ^{14}N, or ^{16}O). This assumption is reasonable, taking into account the existence of the short track#3 and the Coulomb barrier of the target nucleus. For each of the modes without neutron emission, if the sum of momenta deviated from zero by more than 3 standard deviations, the mode was rejected. For the modes with one neutron emission, the momentum of the neutron was assigned to the missing

Table 4.2: Possible decay modes of the double-hypernucleus which include $_\Lambda$He as a decay daughter. The errors on $B_{\Lambda\Lambda}$ and $\Delta B_{\Lambda\Lambda}$ do not include those of the binding energies of single-hypernuclei. Only the cases of $\Delta B_{\Lambda\Lambda} > -20$ MeV are listed.

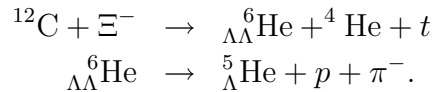| double-hyp.	#2	#5	#6		$B_{\Lambda\Lambda}$ [MeV]	$\Delta B_{\Lambda\Lambda}$ [MeV]
$_{\Lambda\Lambda}^{5}$He	$_{\Lambda}^{4}$He	p	π^-		7.1 ± 0.5	2.4 ± 0.5
$_{\Lambda\Lambda}^{6}$He	$_{\Lambda}^{5}$He	p	π^-		6.9 ± 0.6	0.6 ± 0.6
$_{\Lambda\Lambda}^{7}$He	$_{\Lambda}^{5}$He	p	π^-	$1n$	< 8.6	< 0.3
$_{\Lambda\Lambda}^{7}$He	$_{\Lambda}^{6}$He	p	π^-		6.3 ± 0.7	-2.0 ± 0.7
$_{\Lambda\Lambda}^{8}$He	$_{\Lambda}^{5}$He	p	π^-	$2n$	< 6.8	< -7.2
$_{\Lambda\Lambda}^{8}$He	$_{\Lambda}^{5}$He	d	π^-	$1n$	< 7.4	< -6.6
$_{\Lambda\Lambda}^{8}$He	$_{\Lambda}^{6}$He	p	π^-	$1n$	< 6.6	< -7.4
$_{\Lambda\Lambda}^{8}$He	$_{\Lambda}^{7}$He†	p	π^-		7.7 ± 0.8	-6.3 ± 0.8
$_{\Lambda\Lambda}^{9}$He	$_{\Lambda}^{5}$He	p	π^-	$3n$	< 7.2	< -7.1
$_{\Lambda\Lambda}^{9}$He	$_{\Lambda}^{5}$He	d	π^-	$2n$	< 8.2	< -6.1
$_{\Lambda\Lambda}^{9}$He	$_{\Lambda}^{5}$He	t	π^-	$1n$	< 11.2	< -3.1
$_{\Lambda\Lambda}^{9}$He	$_{\Lambda}^{6}$He	p	π^-	$2n$	< 7.2	< -7.1
$_{\Lambda\Lambda}^{9}$He	$_{\Lambda}^{6}$He	d	π^-	$1n$	< 8.4	< -5.9
$_{\Lambda\Lambda}^{9}$He	$_{\Lambda}^{7}$He†	p	π^-	$1n$	< 11.2	< -3.1
$_{\Lambda\Lambda}^{9}$He	$_{\Lambda}^{7}$He†	d	π^-		13.4 ± 0.5	-0.9 ± 0.5
$_{\Lambda\Lambda}^{9}$He	$_{\Lambda}^{8}$He	p	π^-		6.4 ± 0.8	-7.9 ± 0.8

† We took the value of 7.0 MeV for the upper limit of the Λ hyperon binding energy in $_{\Lambda}^{7}$He, because it has not yet been averaged [73].

Table 4.3: Possible production modes of the double-hypernucleus. The errors on the mass of Ξ^- hyperon and the binding energies of single-hypernuclei are not included in the errors on $B_{\Lambda\Lambda}$ and $\Delta B_{\Lambda\Lambda}$. Only the cases of $\Delta B_{\Lambda\Lambda} < 20$ MeV are listed.

Target	#1	#3	#4		$B_{\Lambda\Lambda}$ [MeV]	$\Delta B_{\Lambda\Lambda}$ [MeV]
^{12}C	$_{\Lambda\Lambda}^{6}$He	^{4}He	p	$2n$	> 16.9	> 10.6
^{12}C	$_{\Lambda\Lambda}^{6}$He	^{4}He	d	$1n$	14.5 ± 0.7	8.2 ± 0.7
^{12}C	$_{\Lambda\Lambda}^{6}$He	^{4}He	t		7.3 ± 0.2	1.1 ± 0.2
^{12}C	$_{\Lambda\Lambda}^{7}$He	^{4}He	p	$1n$	21.6 ± 1.3	13.3 ± 1.3
^{14}N	$_{\Lambda\Lambda}^{6}$He	^{7}Li	p	$1n$	24.4 ± 2.1	18.2 ± 2.1
^{14}N	$_{\Lambda\Lambda}^{6}$He	^{6}Li	d	$1n$	25.8 ± 1.3	19.6 ± 1.3
^{14}N	$_{\Lambda\Lambda}^{6}$He	^{4}He	^{4}He	$1n$	17.9 ± 1.5	11.7 ± 1.5
^{14}N	$_{\Lambda\Lambda}^{7}$Li	^{4}He	t	$1n$	26.2 ± 0.9	17.2 ± 0.9
^{14}N	$_{\Lambda\Lambda}^{9}$Li	p	^{4}He	$1n$	31.5 ± 1.8	17.9 ± 1.8
^{16}O	$_{\Lambda\Lambda}^{8}$Li	^{4}He	^{4}He	$1n$	31.1 ± 0.9	19.9 ± 0.9

momentum of the three charged particles (track#1, #3, and #4). For the modes with more than one neutron emission, the lower limits of the total kinetic energy of the neutrons were calculated from the missing momentum. The results for $\Delta B_{\Lambda\Lambda} < 20$ MeV are presented in Table 4.3. The values of $B_{\Lambda\Lambda}$ and $\Delta B_{\Lambda\Lambda}$ were calculated with the Ξ^- hyperon binding energy B_{Ξ^-} set to zero. Hence these values are lower limits of $B_{\Lambda\Lambda}$ and $\Delta B_{\Lambda\Lambda}$, and their true values are larger, depending on the actual value of B_{Ξ^-}.

A comparison of the values of $B_{\Lambda\Lambda}$ and $\Delta B_{\Lambda\Lambda}$ obtained from both point A and B was made. After rejecting the modes which have inconsistent values, only one interpretation remained,

$$
\begin{aligned}
^{12}\text{C} + \Xi^- &\rightarrow {}_{\Lambda\Lambda}^{6}\text{He} + {}^4\text{He} + t \\
{}_{\Lambda\Lambda}^{6}\text{He} &\rightarrow {}_{\Lambda}^{5}\text{He} + p + \pi^-.
\end{aligned}
$$

The fact that the tracks of the reaction products were coplanar at both points A and B also suggests that no neutrons were emitted from either vertex. The decay mode of $_{\Lambda}^{5}$He is non-mesonic but not uniquely determined.

The possibilities that the double-hypernucleus or the single-hypernucleus was produced in an excited state can be rejected for the following reasons. If the double-hypernucleus or the other fragments emitted from the Ξ^- stopping point had been produced in an excited state, the value of $\Delta B_{\Lambda\Lambda}$ calculated at the production point A would be increased by the excitation energy. On the other hand, if the single-hypernucleus or the residual particles emitted from the decay of the double-hypernucleus had been created in an excited state, the value of $\Delta B_{\Lambda\Lambda}$ calculated at the decay point B would be decreased by the excitation energy. In both cases, the difference between $\Delta B_{\Lambda\Lambda}$ calculated at point A and

at point B would be enlarged and the consistency of the values of $\Delta B_{\Lambda\Lambda}$ would not be satisfied. Hence, our event, Nagara, has been interpreted uniquely as the sequential weak decay of $_{\Lambda\Lambda}^{6}\mathrm{He}$. Moreover, in the production and decay of $_{\Lambda\Lambda}^{6}\mathrm{He}$, no particle-stable excited states are known or expected for any of the reaction products. Therefore, there are no ambiguities arising from excited states.

The $_{\Lambda\Lambda}^{6}\mathrm{He}$ hypernucleus constitutes the lightest closed shell by p, n, and Λ baryons. H. Bando *et al.* indicated its importance in a multi-hypernuclear cluster system, and proposed the name "Lambpha $(\widehat{\alpha})$" for $_{\Lambda\Lambda}^{6}\mathrm{He}$ from the analogue of the α particle [74, 75].

4.3 Λ-Λ interaction

The value of $\Delta B_{\Lambda\Lambda}$ was obtained as 0.62 ± 0.61 MeV from the decay vertex B of the double-hypernucleus, while its lower limit was determined as 1.08 ± 0.22 MeV from the production point A. These errors also include the uncertainties in the values of the mass of the Ξ^- hyperon (0.13 MeV) [76] and the binding energy of $_{\Lambda}^{5}\mathrm{He}$ (0.02 MeV) [73]. A kinematic fit was applied at each vertex independently using the kinematic constraints of conservation of momentum and energy. The kinematic constraints are expressed by the following equations;

$$
\begin{aligned}
C_1^A &= \sqrt{m_1^2 + p_1^2} + \sqrt{m_3^2 + p_3^2} + \sqrt{m_4^2 + p_4^2} - (m_{^{12}\mathrm{C}} + m_{\Xi^-} - B_{\Xi^-}) \\
C_2^A &= p_1 \sin\theta_1 \cos\phi_1 + p_3 \sin\theta_3 \cos\phi_3 + p_4 \sin\theta_4 \cos\phi_4 \\
C_3^A &= p_1 \sin\theta_1 \sin\phi_1 + p_3 \sin\theta_3 \sin\phi_3 + p_4 \sin\theta_4 \sin\phi_4 \\
C_4^A &= p_1 \cos\theta_1 + p_3 \cos\theta_3 + p_4 \cos\theta_4 \\
C_1^B &= \sqrt{m_2^2 + p_2^2} + \sqrt{m_5^2 + p_5^2} + \sqrt{m_6^2 + p_6^2} - m_1 \\
C_2^B &= p_2 \sin\theta_2 \cos\phi_2 + p_5 \sin\theta_5 \cos\phi_5 + p_6 \sin\theta_6 \cos\phi_6 \\
C_3^B &= p_2 \sin\theta_2 \sin\phi_2 + p_5 \sin\theta_5 \sin\phi_5 + p_6 \sin\theta_6 \sin\phi_6 \\
C_4^B &= p_2 \cos\theta_2 + p_5 \cos\theta_5 + p_6 \cos\theta_6,
\end{aligned}
$$

where m_i and p_i is the mass and the momentum of the particle of track#i and θ_i and ϕ_i are the azimuthal and zenith angles of the particle, respectively. The mass of a $^{12}\mathrm{C}$ nucleus and a Ξ^- hyperon are denoted as $m_{^{12}\mathrm{C}}$ and m_{Ξ^-}, respectively, and B_{Ξ^-} is the binding energy of a Ξ^- hyperon. In the fit at vertex B the momentum of the proton (track#5) was constrained to have a value consistent with the particle entering the acrylic base film but not emerging from it, whereas the mass of the double-hypernucleus was a free parameter in both the fit at vertex A and the fit at B. By minimizing the χ^2, we obtained $\Delta B_{\Lambda\Lambda} = 0.69 \pm 0.54$ MeV from the decay vertex B, and $\Delta B_{\Lambda\Lambda} - B_{\Xi^-} = 0.92 \pm 0.21$ MeV from the production point A. The value of B_{Ξ^-} was obtained experimentally from these values as -0.24 ± 0.58 MeV. The fitted momentum of the proton (track#5) was 87.9 ± 3.0 MeV/c and the corresponding range was 127 ± 15 μm, which agrees with the fact that the proton entered but did not emerge from the base film.
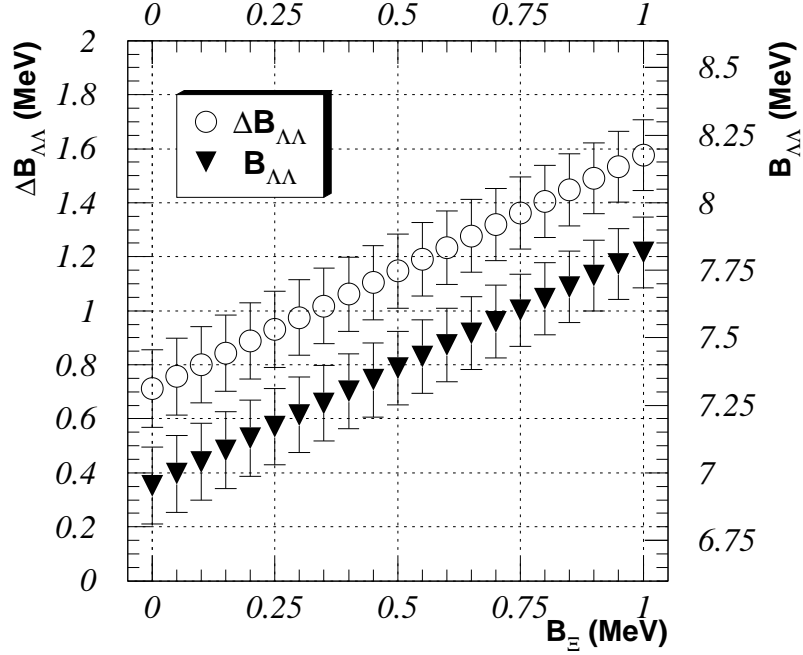
Figure 4.3: Plot of $\Delta B_{\Lambda\Lambda}$ against B_{Ξ^-}.

The values of $B_{\Lambda\Lambda}$ and $\Delta B_{\Lambda\Lambda}$ were determined uniquely from vertex B with large errors, whereas the values obtained from vertex A were more precise but depend on B_{Ξ^-}. In order to obtain their most probable values, we combined the two independent determinations for several fixed values of the Ξ^- hyperon binding energy B_{Ξ^-}. The results are presented in Fig. 4.3. They can be expressed as a function of B_{Ξ^-} (MeV);

$$B_{\Lambda\Lambda} = 7.13 + 0.87\ B_{\Xi^-}\ (\pm 0.19)\ \text{MeV}, \tag{4.1}$$

$$\Delta B_{\Lambda\Lambda} = 0.89 + 0.87\ B_{\Xi^-}\ (\pm 0.20)\ \text{MeV}. \tag{4.2}$$

According to theoretical calculations for the nuclear absorption rate of Ξ^- hyperons [77, 78, 79], Ξ^- hyperon capture from an atomic $3D$ state in ^{12}C is dominant, but capture from a $4F$ or $2P$ state is not negligible. The value of B_{Ξ^-} of the $2P$ state varies with the Ξ^- hyperon-nucleus potential well depth, whereas the energy level of the $3D$ state is more relieably calculated because it depends overwhelmingly on the Coulomb interaction rather than the Ξ^- hyperon-nucleus strong interaction. The value of B_{Ξ^-} of the $3D$ state is 0.13 MeV, which is consistent with the present experimental result of -0.24 ± 0.58 MeV. Adopting the value $B_{\Xi^-} = 0.13$ MeV as the most probable value, the weighted mean values are $B_{\Lambda\Lambda} = 7.25 \pm 0.19\ ^{+0.18}_{-0.11}$ MeV and $\Delta B_{\Lambda\Lambda} = 1.01 \pm 0.20\ ^{+0.18}_{-0.11}$ MeV, where the systematic errors are determined from the fact that the value of B_{Ξ^-} is uncertain in the range from 0 to 0.34 MeV in our measurement.

Figure 4.4 shows the past results of $\Delta B_{\Lambda\Lambda}$ measurements as well as the present
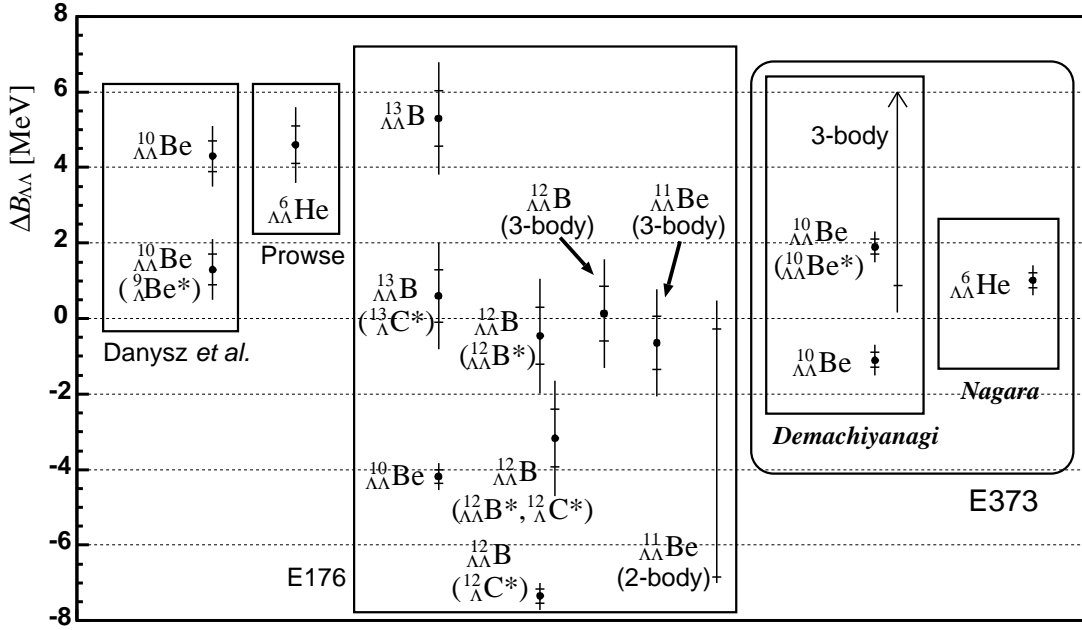
Figure 4.4: Comparison with past results of $\Delta B_{\Lambda\Lambda}$ measurements. The indicated error bars do not include the uncertainty of the Ξ^- hyperon binding energy.

result. The items in the same square are the possible interpretations for the same observed event. The event named "Demachiyanagi" is the first double-hypernucleus event found in E373. In the case of two-body fragmentation at the Ξ^- hyperon capture point, the species was uniquely interpreted as $^{10}_{\Lambda\Lambda}$Be, but the values of $\Delta B_{\Lambda\Lambda}$ depends on whether the $^{10}_{\Lambda\Lambda}$Be had been produced in the ground state or in the excited state. It leads $B_{\Lambda\Lambda} = 12.3 \pm 0.2\ ^{+0.3}_{-0.1}$ MeV and $\Delta B_{\Lambda\Lambda} = -1.1 \pm 0.2\ ^{+0.3}_{-0.1}$ MeV if produced in the ground state, whereas it gives values for the ground state as $B_{\Lambda\Lambda} = 15.3 \pm 0.2\ ^{+0.3}_{-0.1}$ MeV and $\Delta B_{\Lambda\Lambda} = 1.9 \pm 0.2\ ^{+0.3}_{-0.1}$ MeV if created in the excited state, where the excitation energy of $^{10}_{\Lambda\Lambda}$Be is assumed to be same as those of ^{8}Be and $^9_\Lambda$Be, 3.0 MeV [80]. In the three-body fragmentation case, the species could not be identified uniquely and only the lower limit of the value of $\Delta B_{\Lambda\Lambda}$ was obtained. The example reported by Danysz $et\ al.$ [28, 29] gave a value of $\Delta B_{\Lambda\Lambda}$ to be about 4.5 MeV. As mentioned in Chapter 1, there remains the possibility that the single-hypernuclei was produced in excited states. In such a case, $\Delta B_{\Lambda\Lambda}$ would be about 1 MeV and not in contradiction with our result. We have reanalyzed the double-hypernucleus event found by E176 [32, 33] with the possibility of the production in excited states taken into account. The result are also presented in the figure. The detail of the reanalysis of the E176 event is presented in Appendix C. The violent disagreement between our result for $\Delta B_{\Lambda\Lambda}$ and that reported by Prowse [30] confirms the doubts on the authenticity of the previous event.

4.4 Recent progress of theory

The present result has established that the Λ-Λ interaction is attractive but considerably weaker than that widely claimed. A number of theoretical calculations have been made since the result of the Nagara event was published. I. N. Filikhin and A. Gal performed new Faddeev-Yakubovsky calculations for light double-hypernuclei and demonstrated the Nijimegen soft-core model NSC97 simulation is close to reproducing our $^{6}_{\Lambda\Lambda}$He binding energy [81]. E. Hiyama *et al.* calculated the binding energies for $A = 7$-10 double-hypernuclei based on the $\alpha + x + \Lambda + \Lambda$ four-body cluster model with $x = n$, p, d, t, ^{3}He, and α, and argued that the A-dependence of $\Delta B_{\Lambda\Lambda}$ originates mainly from the nuclear shrinkage caused by attached Λ hyperons [82]. Thier calculation well reconstracted the $B_{\Lambda\Lambda}$ of the Demachiyanagi event, and they claimed the event can be interpreted most probably as the $^{10}_{\Lambda\Lambda}$Be double-hypernuclear production in the 2^{+} excited state with the excitation energy of 2.86 MeV. Myint *et al.* investigated the Pauli suppresion effect due to the $\Lambda\Lambda$-ΞN coupling, and the effect in $^{6}_{\Lambda\Lambda}$He was as large as 0.43 MeV for the NSC97e coupling strength [83]. They pointed out that the attractive effect of the coupling is enhanced in $^{5}_{\Lambda\Lambda}$He and $^{5}_{\Lambda\Lambda}$H by the formation of an α particle in core nuclei, and predicted $\Delta B_{\Lambda\Lambda}$ of $^{5}_{\Lambda\Lambda}$He is about 0.27 MeV larger than that of $^{6}_{\Lambda\Lambda}$He. Fujiwara *et al.* recently proposed a new quark-cluster model, named fss2. In this model, they upgraded their previous model for the nucleon-nucleon and hyperon-nucleon interactions by incorporating more complete effective meson-exchange potentials. They predicted the baryon-baryon interactions in the strangeness $S = -2$, -3, and -4 sectors, and pointed out the roughly-estimated value of $\Delta B_{\Lambda\Lambda}$ for $^{6}_{\Lambda\Lambda}$He is about 1 MeV [84]. Takatsuka *et al.* had argued the observed surface temperatures of neutron stars could be explained by introducing the hyperon superfluidity in neutron star cores [25, 27]. Recently they reported that the influence of the new value of $\Delta B_{\Lambda\Lambda}$ was small for the hyperon-mixing problem in nuetron stars, but the hyperon-superfluidity problem would be significantly affected. Their recalculation using the new Λ-Λ interaction strength resulted in that the existence of the Λ superfluidity is less likely, but the possibilities of those for other hyperons still remain [85, 86].

It is necessary to observe various double-hypernuclear isotopes for the systematic understanding of the baryon-baryon interactions with $S = -2$ sectors and the structures of double-hypernuclei. Further analysis of the remaining emulsion of E373 will provide new examples of double-hypernuclei. Moreover, a new hybrid-emulsion experiment (E964) is now prepared at BNL-AGS, which aims to observe double-hypernuclei with ten times as high statistics as that in E373.

4.5 Lower limit of the H mass

From the relation eq. (1.5), the E176 experiment presented a lower limit on the mass of the H dibaryon as 2203.7 ± 0.7 MeV/c^2 [32]. Several counter experiments

have put the upper limits on the production rate of the H dibaryon [42, 87, 88], which were below the theoretical calculation [89] in the mass region below 2200 MeV/c^2, and indicate the nonexistence of a deeply bound H dibaryon. Using the present result of $B_{\Lambda\Lambda}$ from the decay vertex, the lower limit of the H mass was found to be

$$M_H > 2223.7 \ \ \text{MeV}/c^2 \tag{4.3}$$

at a 90% confidence level, which is much closer to the two-Λ threshold.

Even though the mass limit has been obtained, there still remains the possibility of the existence of the very loosely bound H dibaryon or the resonance state decaying into two Λ hyperons strongly. Recently, the E224 experiment reported the enhancement of the two-Λ invariant mass near its threshold produced via the (K^-, K^+) reaction, which can be interpreted as the H resonance state [60]. A new experiment E522 has been carried out at KEK-PS more recently aiming to confirm the existence of the resonance [90], and the analysis is now under way.

Chapter 5

Hyperon-Induced Weak Decay of Double-Hypernuclei

The study of the weak decay modes of double-hypernuclei draw great interest because it is not important only for the weak interaction between hyperons but also for the structures of double-hypernuclei. In addition to the same decay modes as those of single-hypernuclei, i.e. π-mesonic decay and nucleon-induced non-mesonic decay, double-hypernuclei are expected to have hyperon-induced non-mesonic decay modes;

$$\Lambda\Lambda \rightarrow \Lambda N,$$
$$\Lambda\Lambda \rightarrow \Sigma N.$$

According to theoretical calculations without the H dibaryon, branching ratios of these decay modes are expected to be very small, as listed in Table 5.1. On the other hand, theoretical calculation indicated the free H dibaryon decays into $\Sigma^- p$, $\Sigma^0 n$, and Λn with a branching ratio of 5 : 3 : 2 for the H mass of 2150 MeV/c^2 [1], and the $\Sigma^- p$ mode was expected to be dominant for the heavier H dibaryon. If these branching ratios are measured to be much larger, the ground state of double-hypernuclei can have a large component of H-nuclei rather than that of double-Λ nuclei.

Table 5.1: Theoretical calculations of the branching ratios of the weak decay modes of double-hypernuclei. The results of the calculation by Parreño *et al.* are the ratios against the total width of non-mesonic decay modes.

	Itonaga *et al.* [91]	Parreño *et al.* [92]
mesonic decay	54 %	-
$\Lambda N \rightarrow NN$	44 %	-
$\Lambda\Lambda \rightarrow \Lambda N$	1.5 %	3.8 %
$\Lambda\Lambda \rightarrow \Sigma N$	0.3 %	0.4 %

Table 5.2: Number of prongs observed in σ-stop events.

# of prongs	1	2	3	4	> 5
σ-stop	150 (46 %)	92 (28 %)	42 (13 %)	23 (7 %)	22 (7 %)
clean σ-stop	79 (33 %)	77 (32 %)	42 (18 %)	22 (9 %)	17 (7 %)
E176	13 (25 %)	19 (37 %)	4 (8 %)	11 (21 %)	5 (10 %)

The experimental search for these decays were carried out for the first time using both emulsion and scintillating-fiber detectors.

5.1 Number of Ξ^- capture events

Until now, we analyzed about 32 % of the total emulsion. Among them, we found 236 events where the vertex topology in the emulsion was uniquely categorized to "σ-stop", as mentioned in Sec. 3.5.5.

Table 5.2 presents the distribution of the number of prongs emitted from σ-stop points together with that observed in E176 [64]. There is a large discrepancy between the number of 1-prong events in the σ-stop category and that in the "clean σ-stop" because many 1-prong events were categorized both to ρ-stop and to σ-stop. Considering the statistical fluctuation, the prong number distribution of the clean σ-stop events are consistent with that in E176.

Figure 5.1 shows spectra of mass and momentum of scattered particles, and missing momentum and missing mass of the $p(K^-, K^+)X$ reaction. The white spectra are for all events, the hatched ones for those after event selection by the eye-scanning of the SciFi images, and the doubly hatched ones for the "clean σ-stop" events. Note that the momentum for all σ-stop events were distributed between 0.8 GeV/c and 1.3 GeV/c. About 89 % of the σ-stop events were included in the momentum region above 0.95 GeV/c, where the quasi-free $'p'(K^-, K^+)\Xi^-$ reaction is dominant.

The main backgrounds in the "clean σ-stop" events are π^- meson and Σ^- hyperon captures at rest in emulsion. Since the energy loss dE/dx of Ξ^- hyperons in emulsion is more than twice that of π^- mesons at same distance from stopping points, the contamination of stopped π^- mesons can be discriminated by using the thickness information of the tracks in the emulsion. The thickness of each track was categorized by eye-scanning to four grades, "thin", "gray", "black", and "thick". By requiring the track was categorized to "thick", the number of "clean σ-stop" events was reduced to 204.

The mis-identification of incident and scattered π/K mesons causes the Σ^- backgrounds via the (π^-, K^+) and (K^-, π^+) reactions, respectively. The contamination of π^- mesons in the incident K^- mesons was estimated to be 0.20 % from the TOF spectrum of the beam particles. Since the forward angle cross section of
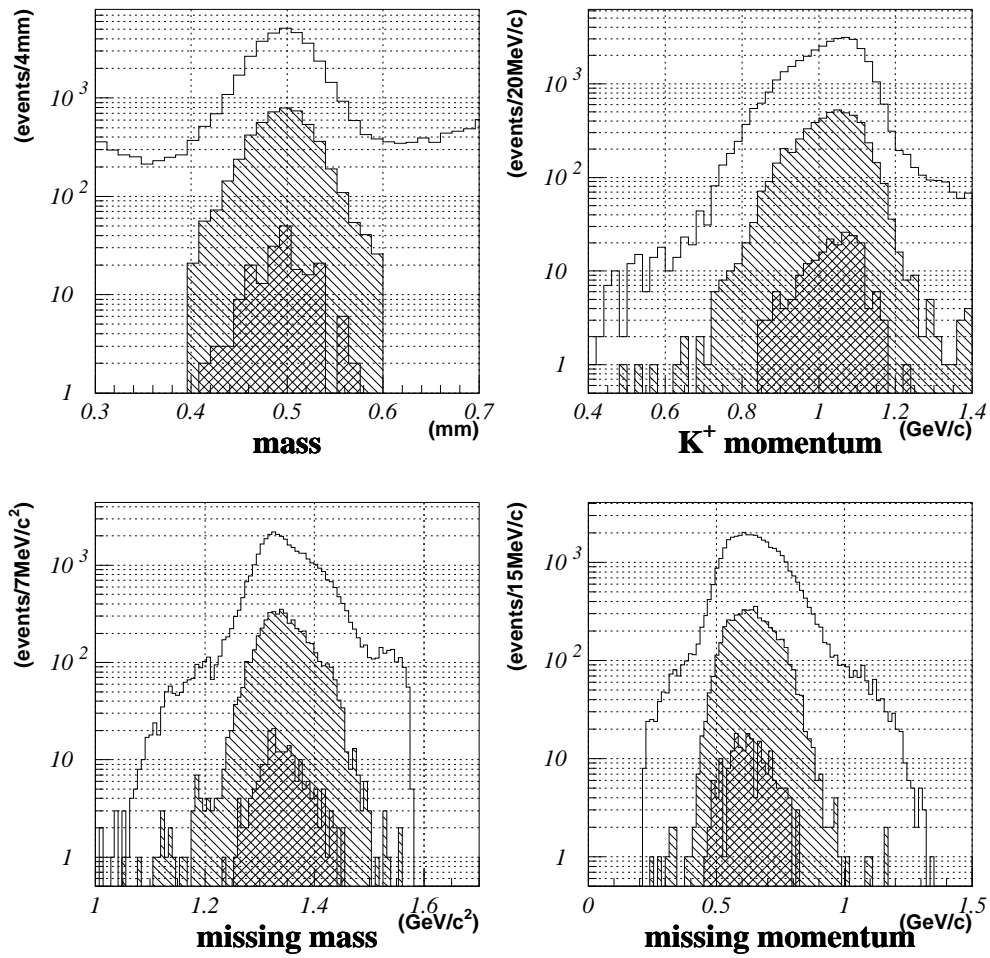
Figure 5.1: Spectra of mass and momentum of secondary particles, and missing mass and missing momentum of the $p(K^-, K^+)X$ reaction. The white spectra show those of all events, the hatched ones those after event selection by the eye-scanning of the SciFi images, and the doubly hatched ones those of the σ-stop events.
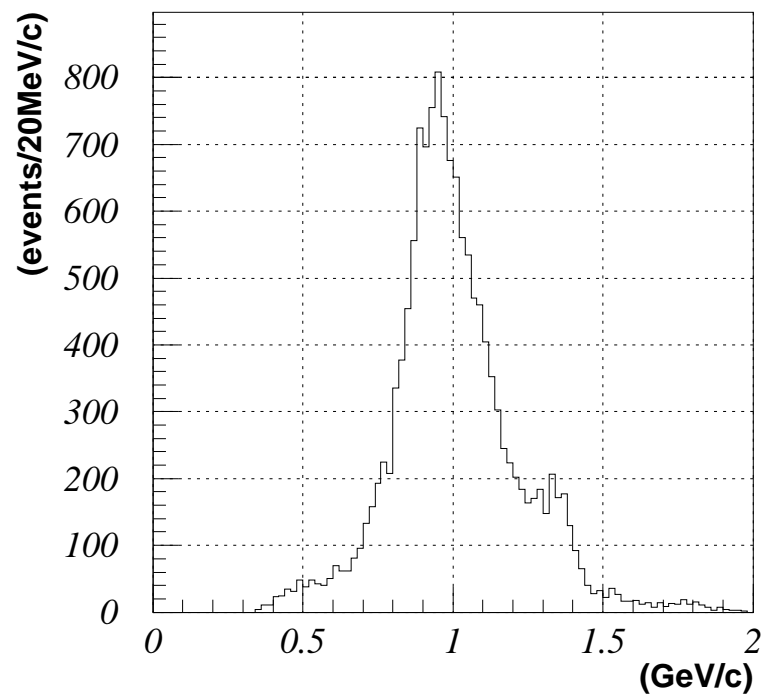
Figure 5.2: Momentum distribution of the scattered particles in the mass region from 0.2 GeV/c^2 to 0.4 GeV/c^2.

the $'p'(\pi^-, K^+)\Sigma^-$ reaction is almost same as that of the $'p'(K^-, K^+)\Xi^-$ reaction, the number of the Σ^- backgrounds from the $'p'(\pi^-, K^+)\Sigma^-$ reaction was set to 0.20 %. On the other hand, the contamination of π^+ mesons in the scattered K^+ mesons was obtained to be 1.1 % from the mass spectrum of the secondary particles. Figure 5.2 shows the momentum distribution of the scattered particles of the mass region between 0.2 GeV/c^2 and 0.4 GeV/c^2. The small bump around 1.35 GeV/c is associated with the production of Σ^- and $\Sigma(1385)^-$ hyperons. The dominant peak around 0.9 GeV/c came from the $K_s^0 \to \pi^-\pi^+$ decays. The π^+ mesons produced via the (K^-, π^+) reaction are expected to have a momentum around 1.45 GeV/c and 1.2 GeV/c for the Σ^- and $\Sigma(1385)^-$ hyperons production, respectively. Considering the mis-identified π^+ mesons with a momentum between 1.05 GeV/c and 1.3 GeV/c are associated with the $\Sigma(1385)^-$ production, the mass spectrum of the scattered particles in the momentum range from 1.05 GeV/c to 1.3 GeV/c were reconstructed. From the mass spectrum shape, the contamination of π^+ mesons accompanied with the $\Sigma(1385)^-$ production was estimated to be 0.66 %. Adopting the branching ratio of $\Sigma(1385)^- \to \Sigma^-\pi^0$ decay of 6 %, the Σ^- hyperon contamination due to the mis-identified π^+ mesons was determined as 0.04 % for the K^+ momentum region between 0.8 GeV/c and 1.3 GeV/c.

Σ^- hyperons can be also produced via the two-step ^{12}C$(K^-, K^+\Lambda\Sigma^-)X$ reaction. The E224 experiment reported that seven events of the ^{12}C$(K^-, K^+\Lambda\Sigma^-)X$ reaction were found among 793 (K^-, K^+) reaction events with low K^+ momenta ($p_{K+} < 950$ MeV/c), while no such event observed among 1355 events in the high K^+ momentum region [93]. From this data, the number of $(K^-, K^+\Lambda\Sigma^-)$ backgrounds in the σ-stop events was estimated to be $0.15 \pm 0.06 \, {}^{+0.05}_{-0.00}$ %.

In 184 events out of the 204 clean σ-stop events, two or more candidate tracks were found in the first emulsion plate by the full-automatic scanning system. Among them, there were eight events where more than one candidate track was categorized to σ-stop uniquely. Therefore, probability that a track with same position and same direction accidentally shows a topology of σ-stop was estimated to be $4.3 \, {}^{+1.8}_{-1.5}$ %.

Hence, we have estimated the number of σ-stopped Ξ^- hyperons to be $194.4 \, {}^{+3.1}_{-3.7}$ in our data samples. By adopting the σ-stop/ρ-stop ratio obtained in E176, the number of Ξ^- hyperon captures at rest is $290.1 \, {}^{+4.6}_{-5.6}$. We have searched for the hyperon-induced weak decays of double-hypernuclei using these clean σ-stop event samples. Until now, 166 events out of the 204 σ-stop events have been analyzed to search for the $\Lambda\Lambda \to \Sigma^-p$ decay, and all the 204 events have been analyzed for the $\Lambda\Lambda \to \Lambda n$ decay search.

5.2 $\Lambda\Lambda \to \Sigma^- p$

The search for $\Lambda\Lambda \to \Sigma^-p$ decays of double-hypernuclei was performed by tracing all charged particles emitted from Ξ^- hyperon capture points in the emulsion.
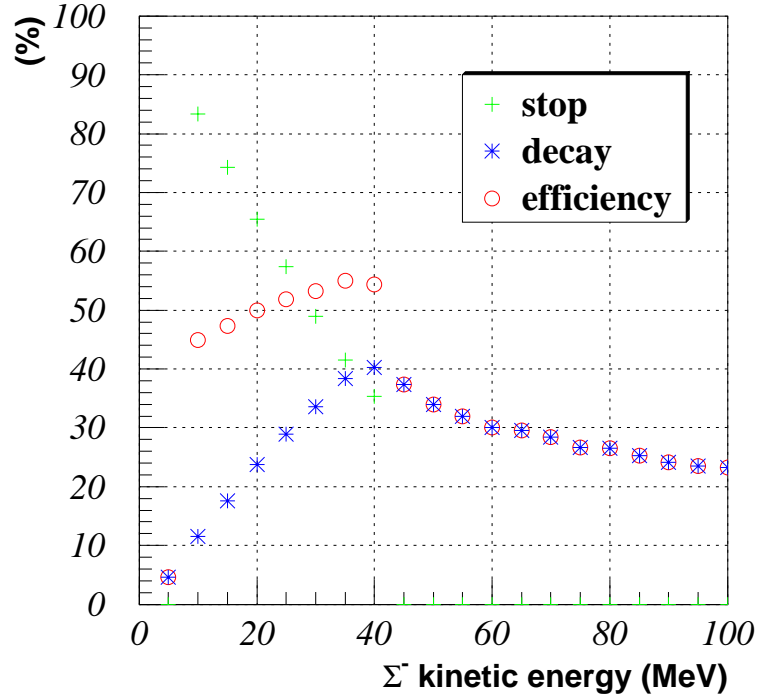
Figure 5.3: Probability that decay-daughter Σ^- hyperons come to rest or decay in the emulsion as a function of Σ^- hyperon kinetic energy. The asterisk and plus marks indicate the probability of Σ^- hyperons to decay and come to rest in the emulsion, respectively. The circle marks are their sums multiplied by the σ-stop/ρ-stop ratio of Σ^- hyperons, and represent the efficiency to detect Σ^- hyperon in the emulsion. The gap between below and above 40 MeV is due to the limit of the searched region of 6 mm.

The decay mode can be identified by detecting in the emulsion the decays or the captures of Σ^- hyperons emitted from Ξ^- hyperon captures. Since the range of Σ^- hyperons having a half momentum of $Q - B_{\Lambda\Lambda}(^6_{\Lambda\Lambda}\text{He})$ was calculated to be 5.3 mm, we searched for the Σ^- hyperon decays and captures up to 6 mm far from the Ξ^- hyperon stopping points. On the other hand, if the range of a Σ^- hyperon to stop is too short, it cannot be distinguished from the decay of a single-hypernucleus. The longest range of single-hypernuclei observed in the E176 experiment was 0.29 mm [64]. Therefore, we cut off the candidate events of Σ^- hyperon captures with the range less than 0.3 mm, which corresponds to the Σ^- hyperon kinetic energy of 7.4 MeV.

The probabilities to detect Σ^- hyperon decays and captures in the searching volume were estimated by GEANT3 simulation, where the Σ^- hyperons were generated at the measured positions of the Ξ^- hyperon capture vertices. The result is shown in Fig. 5.3. The efficiency of the Σ^- detection in the SciFi-Blocks was less than 1 %. As for the case of Σ^- hyperon captures, it cannot

be discriminated from a stopped proton if no charged particle is emitted from the capture point. The efficiencies plotted in the figure include the probability that one or more prongs are emitted from the Σ^- hyperon captures (about 40 % [94]). The binding energies of Λ hyperon B_Λ in ^{89}Y and ^{204}La were measured to be 23.0 MeV and 23.8 MeV, respectively [73, 95]. If we assume the value of $\Delta B_{\Lambda\Lambda}$ is almost constant against the mass number, the value of $B_{\Lambda\Lambda}$ for heavy double-hypernuclei is expected to be about 47 MeV. When a decay-daughter Σ^- hyperon is emitted having a half momentum of $Q - B_{\Lambda\Lambda}$, its kinetic energy is 21 MeV. For light double hypernuclei such as $^6_{\Lambda\Lambda}$He, the mean Σ^- hyperon kinetic energy is 39 MeV. By taking the average of the detection efficiency in the range of the Σ^- kinetic energy between 20 MeV and 40 MeV, we set the overall efficiency as 53 %.

We searched for the Σ^- hyperon captures and decays among 166 samples of the Ξ^- hyperon capture events. No such event was observed. From this result, we derived the upper limit of the product of the probability of double-hypernuclear production from a Ξ^- hyperon capture at rest in emulsion, $P(\Xi^-_{stop} \rightarrow {}_{\Lambda\Lambda}Z)$, and the branching ratio of the decay mode, $Br(\Lambda\Lambda \rightarrow \Sigma^- p)$. Taking into account the σ-stop/ρ-stop ratio of Ξ^- hyperons, the upper limit was obtained to be

$$P(\Xi^-_{stop} \rightarrow {}_{\Lambda\Lambda}Z) \cdot Br(\Lambda\Lambda \rightarrow \Sigma^- p) < 2 \text{ \%} \tag{5.1}$$

at 90 % confidence level, where the kinetic energy of Σ^- hyperons was assumed to be between 20 MeV and 40 MeV.

In the previous experiment E176, one light double-hypernucleus and three heavy ones were found among $77.6 \pm 5.1 \ ^{+0.0}_{-12.2}$ events of Ξ^- hyperon capture at rest in emulsion [64]*. As for the heavy double-hypernuclei, their identifications were made by observing two fast protons having the kinetic energy more than 30 MeV emitted from the Ξ^- capture points as well as the larger energy release than the Q-value of the $\Lambda N \rightarrow NN$ decay, because their production and decay vertices can not be separated even with the spatial resolution of emulsion. Assuming the Γ_n/Γ_p ratio equal to 1 [97, 98]†, where Γ_n and Γ_p represent the partial decay width of the $\Lambda n \rightarrow nn$ and $\Lambda p \rightarrow np$ decays of hypernuclei, respectively, the number of heavy double-hypernuclei produced in E176 is expected to be four times as large as the observed number. Using this assumption, the production probability of double-hypernuclei via the Ξ^- hyperon captures in emulsion can be roughly estimated as 17 %. By combining present result and the E176 result, the branching ratio of $\Lambda\Lambda \rightarrow \Sigma^- p$ decay is less than 12 %. Note that these values of the production probability and the branching ratio are conservative, because the probability to emit a fast proton following a hypernuclear decay is less than $\Gamma_p/(\Gamma_n + \Gamma_p)$ ($= 1/2$ if $\Gamma_n/\Gamma_p = 1$ assumed).

---

*They found one more candidate of a light double-hypernucleus, called "Kariya" event [96], but it was interpreted much likely as the production of twin hypernuclei as mentioned in Appendix C.2.

†The values of the Γ_n/Γ_p ratios given in these references were modified using the recent recalculation of decay neutron and proton spectra [99]. The ratio for $^{56}_\Lambda$Fe, for instance, was to be around 1.0 [100].

It should be stressed that the upper limit currently obtained was deduced from only 25 % of total data of E373. We expect to accumulate one thousand Ξ^- hyperon captures at rest in emulsion, including ρ-stopped Ξ^- hyperons. Then, our sensitivity for the product $P(\Xi_{stop}^- \to {}_{\Lambda\Lambda}Z) \cdot Br(\Lambda\Lambda \to \Sigma^- p)$ is 0.5 %, which corresponds to the sensitivity for the branching ratio of 3 %. The next hybrid-emulsion experiment, BNL-AGS E964, aims to obtain ten-times as large statistics as that of E373. The sensitivity for the branching ratio of the $\Lambda\Lambda \to \Sigma^- p$ decay is expected to be less than 0.3 % in the E964 experiment.

5.3 $\Lambda\Lambda \to \Lambda n$

Compared to the $\Lambda\Lambda \to \Sigma^- p$ decay search, it is much more difficult to search in emulsion for the $\Lambda\Lambda \to \Lambda n$ decay, because both of the final-state particles are invisible, and a Λ hyperon can be emitted via the other processes. The Q-value of $\Lambda\Lambda \to \Lambda N$ decays are 176 MeV, much larger than that of the $\Xi^- p \to \Lambda\Lambda$ reaction following the Ξ^- hyperon capture (28 MeV). It is, therefore, possible to distinguish the emission point of each Λ hyperon, whether a Ξ^--hyperon capture point or a decay point of a double-hypernucleus, by measuring the energy of the Λ hyperon. The Λ hyperons with such high momenta were observed in the E224 experiment [43]. However, the non-mesonic $\Lambda N \to NN$ decay also have the Q-value of 176 MeV. Although the residual Λ hyperon in the $\Lambda\Lambda \to \Lambda N$ decay is expected to have about half momentum of the Q-value, the contamination of the $\Lambda N \to NN$ decay cannot be ignored. Furthermore, even if we use the SciFi-Block detectors to detect the $p\pi^-$ decays of Λ hyperons, the detection efficiency is low due to the distance between the emulsion stack and the SciFi-Block. The efficiencies to detect the Λ hyperons in the SciFi-Blocks for various momenta of Λ hyperons were estimated by the GEANT simulation, and are presented in Fig. 5.4.

We have scanned again the SciFi images of 204 clean σ-stop event samples. We found five events accompanied with a Λ hyperon detected in the D-Block, but no event in the U-Block. Since the D-Block was located at forward angle, some background events accompanied with a high-momentum Λ hyperon are expected. For example, in the case of accidental σ-stop events mentioned in Sec. 5.1, the Ξ^- hyperon produced via the tagged (K^-, K^+) reaction most probably decayed in-flight into $\Lambda\pi^-$, and the Λ hyperon was emitted forward having a high momentum. As for the U-Block placed backward, there is almost no background other than Σ^- stop, which can be accompanied with a Λ hyperon having a rather high momentum due to the Q-value of $\Sigma^- p \to \Lambda n$ (80 MeV).

By assuming the double-hypernuclear production probability $P(\Xi_{stop}^- \to {}_{\Lambda\Lambda}Z)$ is about 17 %, the expected number of the Λ hyperons detected in the U-Block and the D-Block is less than 3, respectively, even if a Λ hyperon is emitted having a half momentum of the Q-value from the decay of double-hypernuclei with a probability of 100 %. The fact that no events were found in the U-Block
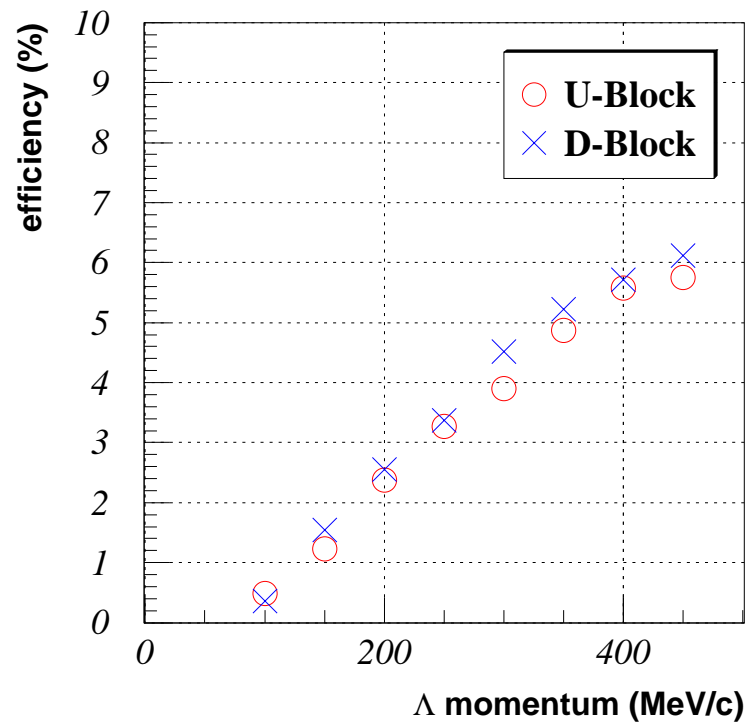
Figure 5.4: Efficiency to detect Λ hyperons in the U-Block (circle) and the D-Block (cross).

is consistent with this estimation, and five events found in the D-Block should be considered as background.

With one thousand Ξ^- hyperon capture events we expect, the sensitivity for the product $P(\Xi^-_{stop} \to \ _{\Lambda\Lambda}Z) \cdot Br(\Lambda\Lambda \to \Lambda n)$ will be 5 %, assuming all Λ hyperon emissions are associated with the $\Lambda\Lambda \to \Lambda n$ decay of double-hypernuclei. Adopting $P(\Xi^-_{stop} \to \ _{\Lambda\Lambda}Z) \sim 17$ %, the sensitivity for the branching ratio is 30 %. Even in E964, the sensitivity for $Br(\Lambda\Lambda \to \Lambda n)$ is 3 % if the similar set-up around the emulsion stack is used. In order to confirm the detection of the $\Lambda\Lambda \to \Lambda N$ decays of double-hypernuclei, we have to perform the coincidence method with Λ hyperon detectors and neutron counters covering large solid angle. Such a counter experiment needs a very high statistics and, therefore, very-high-intensity separated K^- meson beam, and will be able to be carried out after the construction of the JHF.

Chapter 6

Summary

A hybrid-emulsion experiment E373 has been carried out at the KEK 12 GeV proton synchrotron using a 1.66 GeV/c K^- meson beam. The purpose of this experiment is to study double-strangeness nuclei produced via Ξ^- hyperon captures at rest with ten times as large statistics as past experiments. Totally 69 l of nuclear emulsion was exposed to $1.4 \times 10^1 0$ K^- mesons. The Ξ^- hyperons were produced in a diamond target via the quasi-free (K^-, K^+) reaction and were brought to rest in the emulsion. The (K^-, K^+) reaction was tagged by a spectrometer system. Scintillating-fiber detectors were used both to measure the Ξ^- hyperon track and to select events to be analyzed in the emulsion. Tracks of the Ξ^- candidates were searched for and traced in the emulsion by a newly-developed automatic track scanning system.

Until now, about 32 % of the total emulsion has been analyzed. Among them, we have successfully detected three events of the sequential weak decay of a double-Λ hypernucleus, and two events of twin single-Λ hypernuclei. The first two double-hypernucleus events were named "Demachiyanagi" and "Nagara", respectively, and the third one is now under analysis.

The Nagara event is interpreted uniquely as the sequential decay of $_{\Lambda\Lambda}^{6}\mathrm{He}$ ("Lambpha", $\hat{\alpha}$) emitted from a Ξ^- hyperon nuclear capture at rest. The mass has been measured, and the binding energy of the two Λ hyperons, $B_{\Lambda\Lambda}$, and the Λ-Λ interaction energy, $\Delta B_{\Lambda\Lambda}$, have been determined for the first time without the ambiguities arising from a possible production of excited states. The value of $\Delta B_{\Lambda\Lambda}$ obtained from the decay kinematics is 0.69 ± 0.54 MeV. By using both the production and decay kinematics, we obtained $B_{\Lambda\Lambda} = 7.25 \pm 0.19 \, ^{+0.18}_{-0.11}$ MeV and $\Delta B_{\Lambda\Lambda} = 1.01 \pm 0.20 \, ^{+0.18}_{-0.11}$ MeV, where the Ξ^- binding energy, B_{Ξ^-}, of an atomic $3D$ state in $^{12}\mathrm{C}$, 0.13 MeV, is used as the most probable value, and the systematic error is determined from the error of the B_{Ξ^-} obtained from this event. It established that the Λ-Λ interaction energy is attractive but considerably smaller than that previously claimed experimentally. In addition, the lower limit of the mass of the H dibaryon has been obtained as 2223.7 MeV/c^2 at a 90% confidence level.

The first experimental study of the branching ratios of weak decay modes

of double-hypernuclei has been performed. We have searched for $\Lambda\Lambda \rightarrow \Sigma^- p$ decays of double-hypernuclei by observing Σ^- hyperon captures or decays in the emulsion. We have observed no such event among 166 samples of the Ξ^- capture events. This result provided the upper limit of the product of the probability of double-hypernuclear production from a Ξ^- hyperon capture at rest in emulsion, $P(\Xi^-_{stop} \rightarrow {}_{\Lambda\Lambda}\mathrm{Z})$, and the branching ratio of the decay mode, $Br(\Lambda\Lambda \rightarrow \Sigma^- p)$, as $P(\Xi^-_{stop} \rightarrow {}_{\Lambda\Lambda}\mathrm{Z}) \cdot Br(\Lambda\Lambda \rightarrow \Sigma^- p) < 2$ % at a 90 % confidence level. The production probability was roughly estimated to be 17 % from the result of the E176 experiment. By using this value, the branching ratio was derived to be $Br(\Lambda\Lambda \rightarrow \Sigma^- p) < 12$ %.

The analysis of remaining emulsion is now in progress. We expect to accumulate about 1000 Ξ^- hyperon captures at rest in near future. We expect to obtain more double-hypernucleus events, which will provide us not only the confirmation of the result of the Nagara event but also the nuclide dependence of $\Delta B_{\Lambda\Lambda}$ and the excitation energies of double-hypernuclei. We can also derive important informations from the rich samples of stopped Ξ^- hyperons, such as the production probability of double-hypernuclei, the branching ratios of their decay modes, the binding energies of Ξ^- hyperons, and so on.

Acknowledgments

I have completed this work with a support of a number of people. I wish to make a grateful acknowledgement to all those who helped me for their collaboration, advice, support, and encouragement.

First of all, I mould like to express my sincere gratitude to my supervisor, Prof. Ken'ichi Imai. He guided me to the exciting world of the experimental nuclear physics when I was in the third grade of the undergraduate school. He gave me usable advices and helps whenever I had a problem. Discussion with him was always fruitful and interesting, and swelled my interest to physics.

I am deeply grateful to all the collaborators of the KEK-PS E373 experiment. I cordially thank the spokesperson, Prof. Kazuma Nakazawa for his continuous support throughout this work. His tireless zeal for the experiment always encouraged me. I wish to show Dr. Atsuko Kondo-Ichikawa my deep appreciation for her great efforts for the experiment, and for her valuable advice, support, encouragement, and patience. I learned so many things from her experiences on the experiment and her attitude to physics research. I also learned a lot of things from Dr. Yasuhiro Kondo and Mr. Hisayuki Torii, and I wish to acknowledge them. I am grateful to Mr. Choong-Jae Yoon for his contribution for setting up and running the experiment and the analysis. I wish to express my thank to Mr. Hideyuki Tanaka, Mr. Young-Suk Ra, Ms. Hyo-Min Park, Mr. Yukihiro Iwata, Mr. Yousuke Iwata, Mr. Masayoshi Mitsuhara, and Ms. Yuki Nagase for their tireless efforts in the preparation, development, and analysis of emulsion. I appreciate Mr. Hisashi Akikawa for his sizable contribution during the beam time and valuable help on the analysis. I am grateful to Prof. Jung-Keun Ahn and Dr. Kazuhiro Yamamoto for their useful discussion on the analysis. I deeply acknowledge Prof. Takuo Yoshida for his valuable help on GEANT3 simulation. I am thankful to Prof. Mamoru Kawasaki for his efforts in the analysis of the Nagara event. I appreciate the contribution of Dr. Dave Alburger by fabricating a diamond target. His diamond target provided the statistical improvement of our experiment.

I am appreciative of all stuffs of the "Experimental Nuclear and Hadronic Physics (NH)" group, and the former "Experimental Nuclear Physics (NE)" and "Particle and Nuclei (PN)" group in Kyoto University. I am heartily grateful to Prof. Harutaka Sakaguchi, Prof. Naohito Saito, Dr.Masanobu Nakamura, Dr. Kiyohiko Takimoto for their useful discussion, advice, and encouragement. I am thankful to Mr. Masaru Yosoi for his collaboration during the beam time.

Appendix A

Image Reconstruction of the SciFi Detectors

As described in Sec. 2.6, the scintillating-fiber-block detectors (SciFi-Blocks) have very complicated structure, and two images were viewed by one IIT chain. For the image of the U-Block, uz- and vz-planes were overlapped to one image, and the upper part and lower part of the image of the D-Block were overlapped to one image. It is very difficult to scan tracks in such raw images. Therefore, it is necessary to separate an image into each fiber sheet after the correction of the image distortion, and reconstruct the track position in the sensitive volume.

A.1   SciFi-Bundle detector

As for the SciFi-Bunlde detector, each sheet was divided into four or five parts, and they were piled up at the input window of the IIT chain. In order to distinguish the position of each division, thousands of calibrated images were integrated. As shown in Fig. A.1(a), the shape of each fiber bundle is clearly seen on the integrated image. By dividing the image into each fiber-bundle sheet and realigning them, the original image in the detection area was obtained. Figure A.1(b) presents the integrated image after the reconstruction.

A.2   SciFi-Block detectors

A.2.1   Determination of the fiber-sheets positions

In order to obtain the position of each fiber sheet, hundreds of images were integrated and then projected to a horizontal axis. As a result, the peaks of brightness corresponding to the fiber sheets appeared as shown in Fig. A.2. By fitting each of them with a Gaussian, the positions of the fiber sheets and the bordering between two sheets were determined.
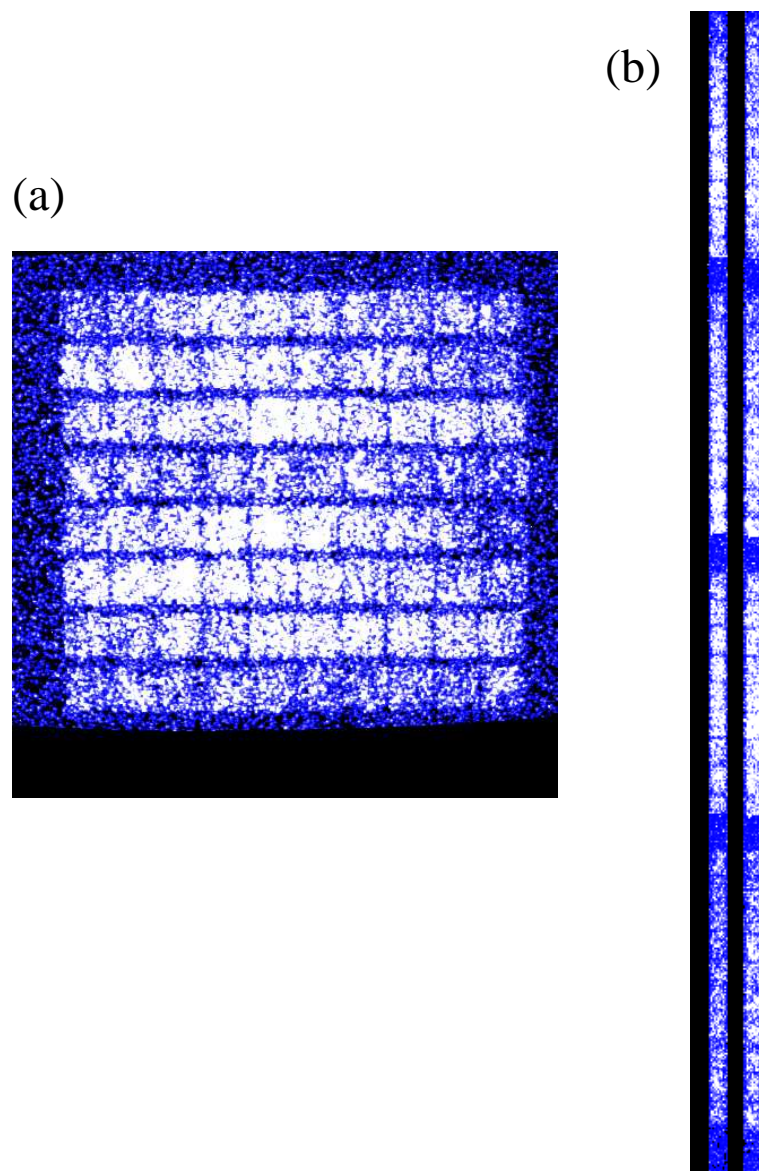
Figure A.1: Reconstruction of the SciFi-Bundle detector. (a) Integrated image of the left channel of the SciFi-Bundle. (b) Image after the reconstruction.
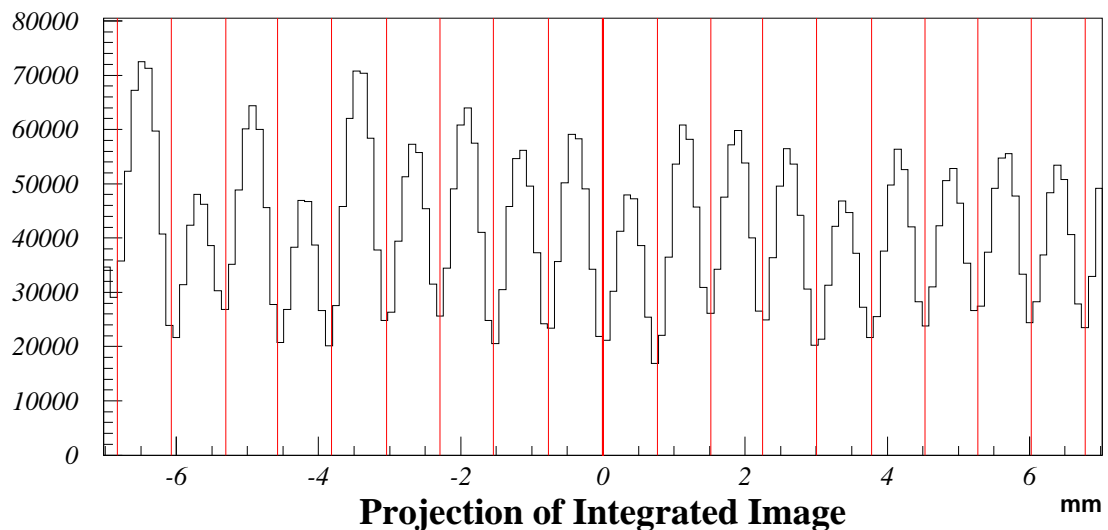
Figure A.2: Integrated image of hundreds of events projected to a horizontal axis. The peak corresponding to each fiber sheet can be seen.
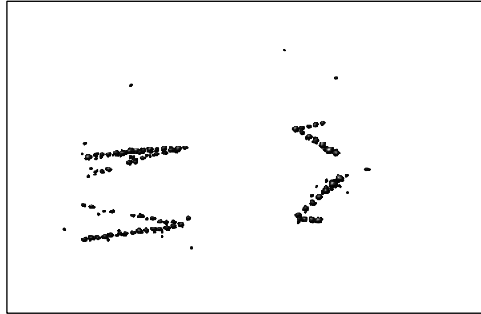
A.2.2   Image clustering

When a raw image is divided simply depending on the horizontal coordinate of each pixel, the center of each photo-cluster is positioned correctly but some part not, as shown in Fig. A.3 (2). This is because even for one photon from a fiber, the size of photoelectrons was broaden when they were amplified in the IIT chain and hit the phosphors. The size of a photo-cluster of a track of a minimum ionizing particle was about 4 pixel × 4 pixel on the CCD.

The mis-reconstruction was solved by clustering the raw image before the sheet separation. The reconstructed position of each pixel was determined from the center position of the cluster it belonged to. The result of the sheet division using this method is presented in Fig. A.3 (3). It can be seen that a raw image was divided into two planes without mis-reconstruction by clustering the raw image.

The image clustering was made by following algorithm:

1. First, searched is a "peak pixel", whose brightness is higher than those of all four adjoining pixels. Each "peak pixel" found is tagged with a unique ID number.

2. The bright pixels adjoining a "peak pixel" are tagged with the same ID as the "peak pixel".

3. If a pixel adjoining an already-tagged pixel has lower brightness than the tagged pixel, it is also tagged with the same ID.

(1) Original Image (Right-side IIT of the U-Block)
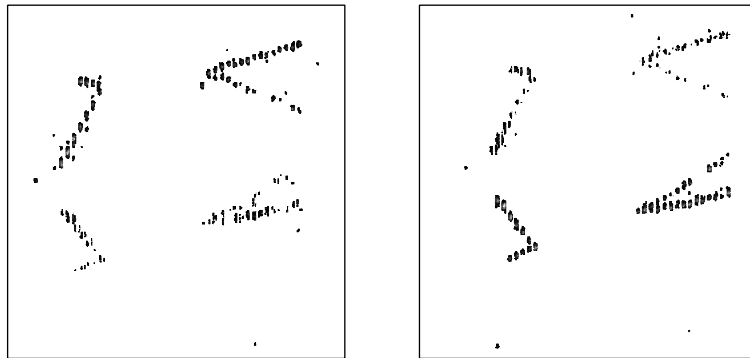
(2) Separated Images without Clustering
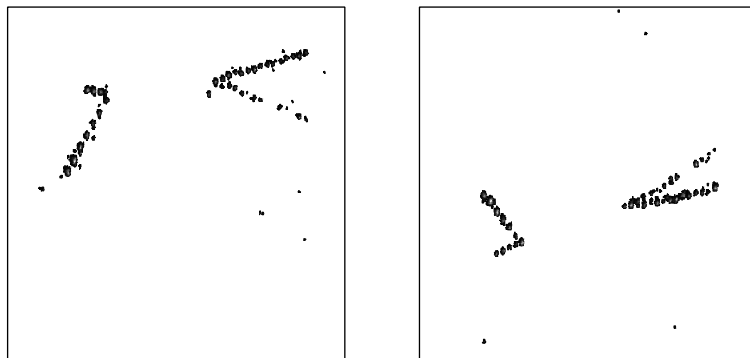
(3) Separated Images with Clustering

Figure A.3: (1) The raw overlapped image, and the separated images (2) without and (3) with the clustering method. In the simple image division without the clustering method, some part of photo-clusters were mis-positioned. The directions of the divided images were changed for the SciFi event display (Fig. 3.8). See text for details of the clustering method.
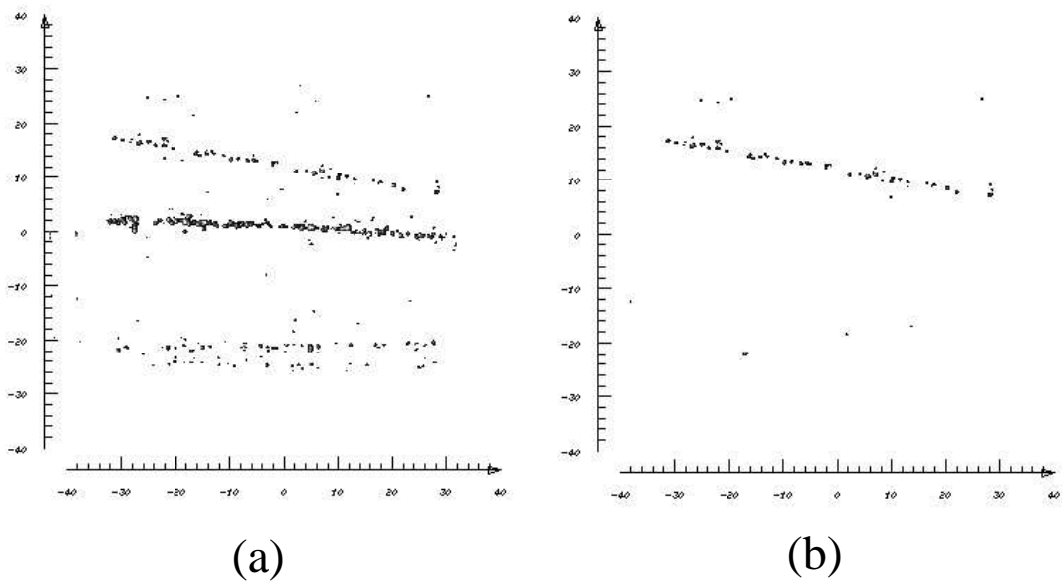
(a)   (b)

Figure A.4: Example of "image cleaning-up". The left side (a) shows a CCD image before cleaning-up, and the right side (b) the image after cleaning-up.

4. All bright pixels are tagged in these manner. Then, pixels with same ID are remarked as a cluster.

A.3 Resolving image overlap

Tracks of two or more successive triggered events can be appeared in one image, depending on the timings of triggers, as described in Sec. 2.8. If two triggers are fired in two fields timing, three fields data are acquired. The first and the second fields belong to the first triggered event, and the second and the third fields belong to the second triggered event; only the second field has overlapped tracks. After the clustering method mentioned above is applied to the image composed of the first two fields, clusters only in the second fields have just one-pixel size in vertical. By requiring the vertical sizes of clusters being larger than one, we can extract only the tracks belonging to the first triggered event. Only the tracks of the second triggered event can be extracted in the same manner from the image composed of the last two fields. Figure A.4 shows an example of such a "cleaning-up" process of a half-overlap image.

On the other hand, if two triggers are fired in one field timing, both two fields have the images of the two events. Such fully overlapped images cannot be resolved. Track information measured by the spectrometer system was used to identify tracks belonging to each triggered event.

Appendix B

Twin-Hypernuclei Event

B.1 Event description

Figure B.1 shows a photograph and schematic drawing of the second twin hyper-nuclei event found in E373. A Ξ^- hyperon stopped at point A, from which two charged particles (#1, #2) were emitted. The particle of track#1 decayed into three charged particles (#3, #4, #5) at point B, while the particle of track#2 into two charged particles (#6, #7) at point C.

The lengths and angles of these tracks are summarized in Table B.1. Track#1 and track#2 are collinear within the measurement errors. The particle of track#5 left upstream from the emulsion stack. The image from the scintillating-fiber detectors is shown in Fig. B.2. Since the particle of track#5 escaped from the emulsion was detected in the SciFi-Bundle but not observed in the U-Block, only the lower limit of the length of track#5 was obtained.
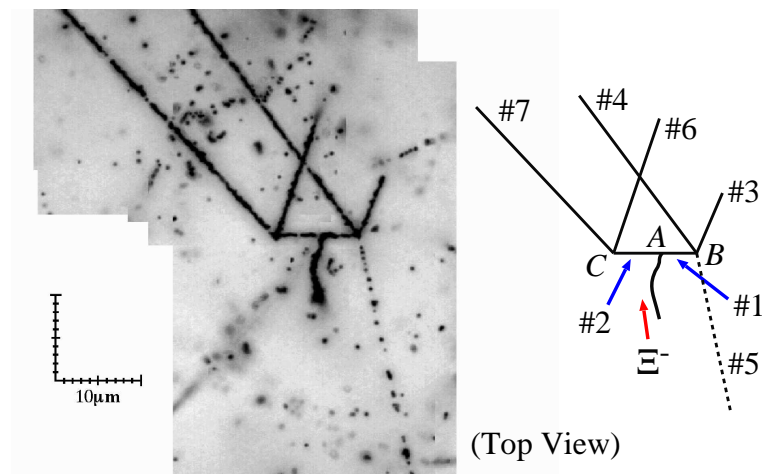
Figure B.1: Photograph and schematic drawing of the second twin-hypernuclei event.

The range-energy relation was calibrated using the measured ranges of α particles, which were emitted from the decays of ^{228}Th, ^{212}Po and ^{214}Po in the emulsion.
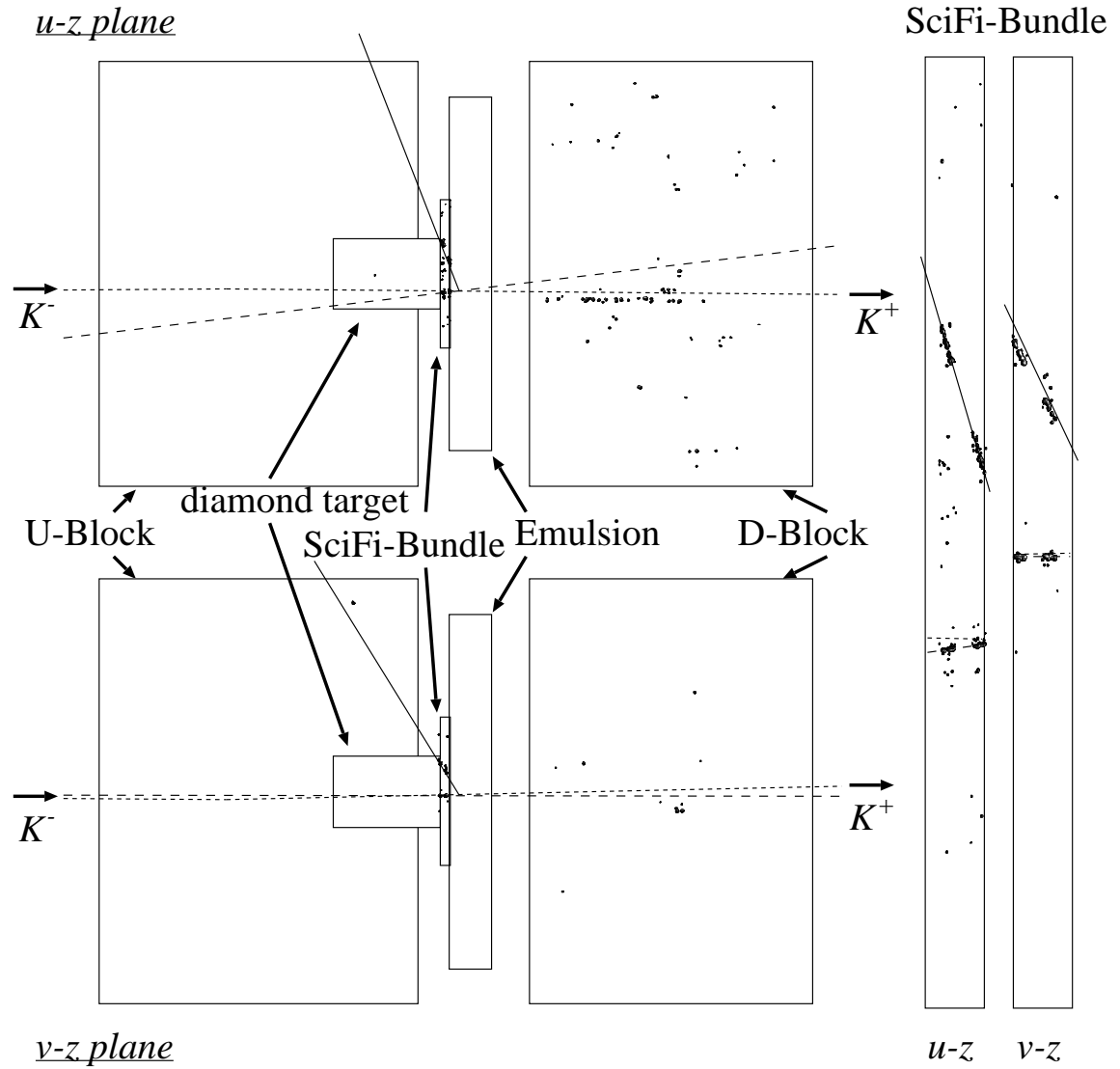
104

Figure B.2: Image of the scintillating-fiber detectors. The dot lines are tracks of incoming K^- and outgoing K^+ mesons measured with the spectrometer system. The dash lines are tracks of the Ξ^- hyperon scanned with the SciFi-Bundle. The solid lines are extrapolated using the position and angle of track#5 in the emulsion.

The ranges of α particles from ^{228}Th, ^{212}Po ^{214}Po are 23.3 ± 0.4 μm, 46.8 ± 0.6 μm and 38.4 ± 0.9 μm, respectively. The density of the emulsion calculated with SRIM2000 is 3.644 ± 0.033 g/cm^3. This is consistent with the measurement value of 3.629 ± 0.063 g/cm^3, which was obtained from the measured weight and thickness of the emulsion plate.

B.2   Event reconstruction

First, the reconstruction of the production vertex A was made. We checked all production modes assuming the Ξ^- hyperon was captured from a light nucleus in emulsion (^{12}C, ^{14}N, or ^{16}O). The kinetic energies of track#1 and #2 were obtained from their ranges. For the modes with neutron emissions, the kinetic energies of the neutrons were calculated from the momentum balance. For the modes without neutron emissions, if the sum of the momenta of the two charged particles (track#1, and #2) deviated from zero by more than three standard deviations, that decay mode was rejected. The sum of the kinetic energies of the charged and neutral particles is referred to as the total energy release, E_{total}, and the difference between E_{total} and the Q-value is the Ξ^- hyperon binding energy, B_{Ξ^-}. The modes were rejected, in which the Ξ^- hyperon is unbound, that is, B_{Ξ^-} is negative even three standard deviations taken into account. The results are listed in Table B.2.

The nuclide of the hypernucleus of track#2 was selected from its decay vertex C. We calculated E_{total} for all decay modes of single-Λ hypernuclei, and selected only those which E_{total} is not more than the Q-value of the decay. The results are listed in Table B.3. Unfortunately, no event selection could be made at the decay vertex of the hypernucleus of track#1 (point A), because the length of track#5 is unknown.

By comparing Table B.2 with Table B.3, three interpretations remained:
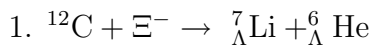
1. ^{12}C $+ \Xi^- \rightarrow\ ^7_\Lambda$Li $+^6_\Lambda$ He

Table B.1: Lengths and angles of tracks.

point	track#	length [μm]	θ [degree]	ϕ [degree]	
A	#1	4.1 ± 0.3	93.3 ± 9.7	179.0 ± 6.9	single-hypernucleus
	#2	5.7 ± 0.4	87.3 ± 6.2	356.8 ± 2.9	single-hypernucleus
B	#3	7.9 ± 0.4	89.9 ± 2.3	247.5 ± 4.4	
	#4	75.6 ± 0.8	84.2 ± 0.2	304.8 ± 0.2	
	#5	6287	73.4 ± 0.2	100.7 ± 0.8	left emulsion
C	#6	4158 ± 18	152.0 ± 0.2	250.4 ± 2.0	
	#7	1204 ± 6	126.3 ± 0.2	311.0 ± 0.2	

Table B.2: Possible production modes of the twin hypernuclei.

Target	#1	#2		Q-value [MeV]	E_{total} [MeV]	B_{Ξ^-} [MeV]
^{12}C	$^{7}_{\Lambda}$Li	$^{6}_{\Lambda}$He		5.2	3.6 ± 0.2	1.6 ± 0.3
^{12}C	$^{7}_{\Lambda}$Li	$^{5}_{\Lambda}$He	$1n$	5.1	4.0 ± 0.3	1.1 ± 0.4
^{12}C	$^{5}_{\Lambda}$He	$^{7}_{\Lambda}$Li	$1n$	5.1	7.9 ± 0.9	-2.8 ± 1.0
^{14}N	$^{9}_{\Lambda}$Be	$^{5}_{\Lambda}$He	$1n$	18.2	8.2 ± 1.0	10.0 ± 1.0
^{14}N	$^{5}_{\Lambda}$He	$^{9}_{\Lambda}$Be	$1n$	18.2	18.3 ± 2.2	-0.1 ± 2.2
^{14}N	$^{9}_{\Lambda}$Li	$^{6}_{\Lambda}$Li		4.2	4.6 ± 0.3	-0.4 ± 0.3
^{14}N	$^{8}_{\Lambda}$Li	$^{7}_{\Lambda}$Li		7.2	4.6 ± 0.3	2.6 ± 0.3
^{16}O	$^{10}_{\Lambda}$Be	$^{7}_{\Lambda}$Li		5.5	5.4 ± 0.3	0.0 ± 0.4
^{16}O	$^{9}_{\Lambda}$Be	$^{8}_{\Lambda}$Li		9.9	5.4 ± 0.3	4.4 ± 0.4

Table B.3: Possible decay modes of the hypernucleus (track#2).

hypernucleus	#6	#7		Q-value [MeV]	E_{total} [MeV]
$^{4}_{\Lambda}$He	p	p	$2n$	166.0	> 86.9
$^{5}_{\Lambda}$He	p	p	$3n$	144.7	> 73.9
$^{5}_{\Lambda}$He	d	p	$2n$	146.9	> 133.7
$^{5}_{\Lambda}$He	p	d	$2n$	146.9	> 114.6
$^{6}_{\Lambda}$He	p	p	$4n$	144.5	> 67.3
$^{6}_{\Lambda}$He	d	p	$3n$	146.8	> 109.1
$^{6}_{\Lambda}$He	p	d	$3n$	146.8	> 94.3
$^{6}_{\Lambda}$He	p	t	$2n$	153.0	> 141.9
$^{7}_{\Lambda}$He	p	p	$5n$	139.9	> 63.4
$^{7}_{\Lambda}$He	d	p	$4n$	142.1	> 96.5
$^{7}_{\Lambda}$He	p	d	$4n$	142.1	> 83.9
$^{7}_{\Lambda}$He	t	p	$3n$	148.3	> 144.3
$^{7}_{\Lambda}$He	p	t	$3n$	148.3	> 114.1
$^{7}_{\Lambda}$He	d	d	$3n$	144.3	> 133.4
$^{8}_{\Lambda}$He	p	p	$6n$	140.1	> 60.7
$^{8}_{\Lambda}$He	d	p	$5n$	142.4	> 88.9
$^{8}_{\Lambda}$He	p	d	$5n$	142.4	> 77.7
$^{8}_{\Lambda}$He	t	p	$4n$	148.6	> 125.2
$^{8}_{\Lambda}$He	p	t	$4n$	148.6	> 99.8
$^{8}_{\Lambda}$He	d	d	$4n$	144.6	> 116.2

This case includes the charged particles only, so the kinematic fit can be applied on the production vertex A, giving following results. In the case both of hypernuclei were produced in ground states, the binding energy of the Ξ^- hyperon, B_{Ξ^-}, is 1.6 ± 0.3 MeV. If the $^7_\Lambda$Li hypernucleus was produced in the excited state, whose excitation energy is $E_x = 0.7$ MeV, the value of B_{Ξ^-} is 0.9 ± 0.3 MeV.

2. ^{12}C $+ \Xi^- \rightarrow \ ^7_\Lambda$Li $+^5_\Lambda$He $+ n$
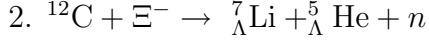
   If both of hypernuclei were produced in ground states, the value of B_{Ξ^-} is 1.1 ± 0.4 MeV, while the case of the production of the excited state of the $^7_\Lambda$Li hypernucleus gives $B_{\Xi^-} = 0.4 \pm 0.4$ MeV.
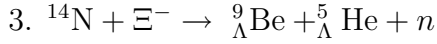
3. ^{14}N $+ \Xi^- \rightarrow \ ^9_\Lambda$Be $+^5_\Lambda$He $+ n$

   In the case both of hypernuclei were produced in ground states, the value of B_{Ξ^-} is 10.0 ± 1.0 MeV. If the $^9_\Lambda$Be hypernucleus was produced in the excited state, whose excitation energy is $E_x = 3.0$ MeV, the value of B_{Ξ^-} is 6.9 ± 1.0 MeV.

The case 3. can be interpreted as the Ξ^- hyperon capture from the nuclear $0s$ state because of its large value of B_{Ξ^-}. This interpretation is less likely, because the absorption rate from the orbit is less than 0.1 %, according to theoretical calculations [78]. The fact that the two Λ-hypernuclei were emitted back-to-back indicates two-body production without neutron emission. Based on simple phase space analysis, however, the probability of such a topology to occur is as large as 20 % both in the case 2. and in 3. Therefore, we cannot reject the case 2. and 3. only from the topology. The interpretation of $^7_\Lambda$Li production in the excited state in the case 2. gives quite consistent value of B_{Ξ^-} with the case that the Ξ^- hyperon was absorbed from the atomic $3D$ orbit. The other B_{Ξ^-} values can correspond to the Ξ^- hyperon capture from the atomic $2P$ state.

Appendix C

Reanalysis of E176 Events

C.1 Double-hypernucleus event

The double-hypernucleus event reported by the E176 experiment was interpreted as $^{10}_{\Lambda\Lambda}$Be or $^{13}_{\Lambda\Lambda}$B, and gave the value of $\Delta B_{\Lambda\Lambda}$ of -4.9 ± 0.7 MeV or 4.9 ± 0.7 MeV, respectively [32, 33]. However, the possibility of the single- or double-hypernuclear production in excited states was ignored in the analysis. We have, therefore, reanalyzed the event by using recalibrated range-energy relation in the emulsion and up-to-date values of masses of hyperons and mesons.

The photograph and schematic drawing of the event is presented in Fig. C.1. Two charged particles (track#1 and #2) were emitted from the Ξ^- hyperon capture point A. The particle of track#1 decayed at point B into a π^- meson (track#4) and another charged particle (track#3), which decayed again into three charged particles (track#5, #6, #7) at point C. The lengths and emission angles of the tracks are summarized in Table C.1.

The kinetic energies of the charged particles were calculated from their ranges. The range-energy relation was calibrated using α decays of thorium series in the emulsion and μ^+ decays from π^+ meson decays at rest. The range of α particles from the decay of ^{212}Po was 50.7 ± 0.5 μm, and that of muons was 640.1 ± 27.6 μm. The density of the emulsion was calculated to be 3.385 ± 0.032 g/cm^3. For the modes with neutron emissions, the kinetic energies of the neutrons were calculated from the momentum balance. For the modes without neutron emissions, if the sum of the momenta of the charged particles deviated from zero by more than three standard deviations, that mode was rejected.

All possible decay modes of the double-hypernucleus (track#1) were checked by the event reconstruction on the vertex B. The results for $\Delta B_{\Lambda\Lambda} > -20$ MeV are listed in Table C.2.

The reconstruction of the production vertex A was performed assuming the Ξ^- hyperon was captured from a light nucleus in emulsion (^{12}C, ^{14}N, or ^{16}O). The results for $\Delta B_{\Lambda\Lambda} < 20$ MeV are listed in Table C.3.

As for the decay vertex C, there remained so many interpretations with neutron emission, and we could not reconstruct the decay mode of the single-
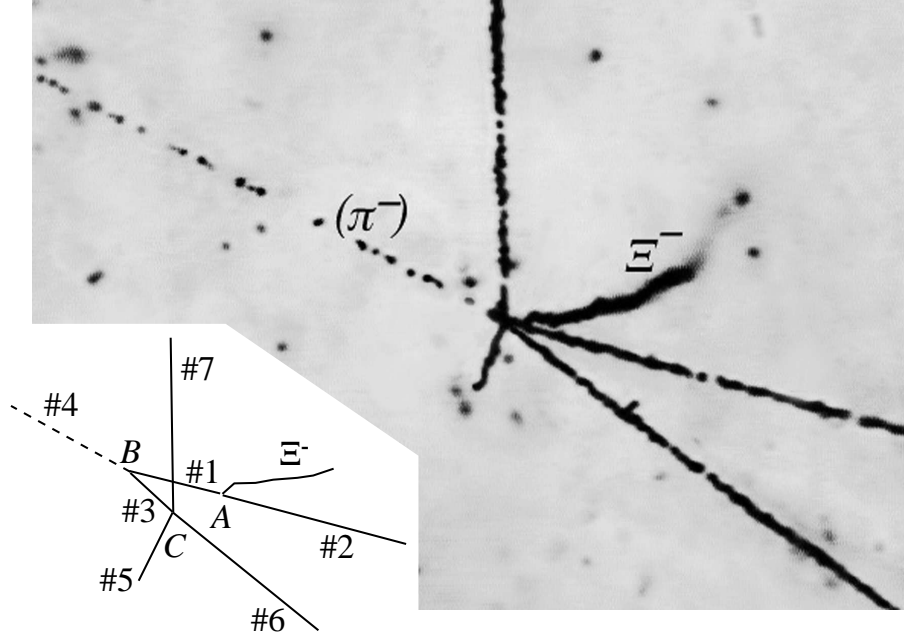
Figure C.1: Photograph and schematic drawing of the E176 double-hypernucleus event.

Table C.1: Lengths and emission angles of the tracks derived from Ref. [32]. At point A, B, and C, angles are expressed by a dip angle (θ) with respect to the direction of the Ξ^- hyperon, track#1, and track#3, and an azimuthal angle (ϕ) with respect to the direction of track#1, #3, and #5, respectively.

point	track#	length [μm]	θ [degree]	ϕ [degree]	
A	#1	3.9 ± 0.4	62.4 ± 7.0	0.0 ± 7.0	double-hyp.
	#2	200.4 ± 3.6	108.8 ± 1.9	177.0 ± 0.2	
B	#3	1.9 ± 0.4	25.5 ± 17.0	0.0 ± 17.0	single-hyp.
	#4	24096.5 ± 763.5	149.9 ± 1.3	176.0 ± 0.2	π^-
C	#5	5.2 ± 0.4	115.8 ± 4.6	0.0 ± 4.6	
	#6	85.7 ± 1.6	13.9 ± 0.3	34.4 ± 0.3	
	#7	70.8 ± 1.3	92.3 ± 0.9	149.3 ± 0.3	

Table C.2: Possible decay modes of the double-hypernucleus. The errors on $B_{\Lambda\Lambda}$ and $\Delta B_{\Lambda\Lambda}$ do not include those of the binding energies of single-hypernuclei. Only the cases of $\Delta B_{\Lambda\Lambda} > -20$ MeV are listed.

double-hyp.	#3	#4		$B_{\Lambda\Lambda}$ [MeV]	$\Delta B_{\Lambda\Lambda}$ [MeV]
$^{6}_{\Lambda\Lambda}\text{He}$	$^{6}_{\Lambda}\text{Li}$	π^-		2.8 ± 0.8	-3.4 ± 0.8
$^{7}_{\Lambda\Lambda}\text{He}$	$^{6}_{\Lambda}\text{Li}$	π^-	$1n$	3.4 ± 0.9	-5.0 ± 0.9
$^{7}_{\Lambda\Lambda}\text{He}$	$^{7}_{\Lambda}\text{Li}$	π^-		10.5 ± 0.8	2.2 ± 0.8
$^{9}_{\Lambda\Lambda}\text{He}$	$^{6}_{\Lambda}\text{Li}$	π^-	$3n$	< 2.2	< -12.1
$^{9}_{\Lambda\Lambda}\text{He}$	$^{7}_{\Lambda}\text{Li}$	π^-	$2n$	< 8.9	< -5.4
$^{9}_{\Lambda\Lambda}\text{He}$	$^{8}_{\Lambda}\text{Li}$	π^-	$1n$	17.3 ± 0.8	3.0 ± 0.8
$^{9}_{\Lambda\Lambda}\text{He}$	$^{9}_{\Lambda}\text{Li}$	π^-		21.4 ± 0.8	7.1 ± 0.8
$^{7}_{\Lambda\Lambda}\text{Li}$	$^{7}_{\Lambda}\text{Be}$	π^-		5.7 ± 0.8	-3.3 ± 0.8
$^{8}_{\Lambda\Lambda}\text{Li}$	$^{7}_{\Lambda}\text{Be}$	π^-	$1n$	-0.0 ± 0.9	-11.2 ± 0.9
$^{8}_{\Lambda\Lambda}\text{Li}$	$^{8}_{\Lambda}\text{Be}$	π^-		12.5 ± 0.8	1.3 ± 0.8
$^{9}_{\Lambda\Lambda}\text{Li}$	$^{8}_{\Lambda}\text{Be}$	π^-	$1n$	5.2 ± 0.9	-8.4 ± 0.9
$^{9}_{\Lambda\Lambda}\text{Li}$	$^{9}_{\Lambda}\text{Be}$	π^-		24.1 ± 0.8	10.5 ± 0.8
$^{10}_{\Lambda\Lambda}\text{Li}$	$^{8}_{\Lambda}\text{Be}$	π^-	$2n$	< 3.2	< -13.8
$^{10}_{\Lambda\Lambda}\text{Li}$	$^{9}_{\Lambda}\text{Be}$	π^-	$1n$	21.9 ± 0.9	4.9 ± 0.9
$^{10}_{\Lambda\Lambda}\text{Li}$	$^{10}_{\Lambda}\text{Be}$	π^-		26.1 ± 0.8	9.1 ± 0.8
$^{9}_{\Lambda\Lambda}\text{Be}$	$^{9}_{\Lambda}\text{B}$	π^-		8.1 ± 0.8	-5.6 ± 0.8
$^{10}_{\Lambda\Lambda}\text{Be}$	$^{10}_{\Lambda}\text{B}$	π^-		8.4 ± 0.8	-5.0 ± 0.8
$^{11}_{\Lambda\Lambda}\text{Be}$	$^{10}_{\Lambda}\text{B}$	π^-	$1n$	5.7 ± 1.4	-12.5 ± 1.4
$^{11}_{\Lambda\Lambda}\text{Be}$	$^{11}_{\Lambda}\text{B}$	π^-		16.6 ± 0.8	-1.6 ± 0.8
$^{12}_{\Lambda\Lambda}\text{B}$	$^{12}_{\Lambda}\text{C}$	π^-		18.9 ± 0.9	-1.5 ± 0.9
$^{13}_{\Lambda\Lambda}\text{B}$	$^{12}_{\Lambda}\text{C}$	π^-	$1n$	4.6 ± 2.4	-18.1 ± 2.4
$^{13}_{\Lambda\Lambda}\text{B}$	$^{13}_{\Lambda}\text{C}$	π^-		27.2 ± 0.8	4.4 ± 0.8
$^{14}_{\Lambda\Lambda}\text{B}$	$^{13}_{\Lambda}\text{C}$	π^-	$1n$	20.7 ± 2.4	-2.0 ± 2.4
$^{14}_{\Lambda\Lambda}\text{B}$	$^{14}_{\Lambda}\text{C}$	π^-		29.3 ± 0.8	6.6 ± 0.8
$^{14}_{\Lambda\Lambda}\text{C}$	$^{14}_{\Lambda}\text{N}$	π^-		13.4 ± 0.9	-10.0 ± 0.9
$^{15}_{\Lambda\Lambda}\text{C}$	$^{15}_{\Lambda}\text{N}$	π^-		20.5 ± 0.9	-3.8 ± 0.9

Table C.3: Possible production modes of the double-hypernucleus. The errors on the mass of Ξ^- hyperon and the binding energies of single-hypernuclei are not included in the errors on $B_{\Lambda\Lambda}$ and $\Delta B_{\Lambda\Lambda}$. Only the cases of $\Delta B_{\Lambda\Lambda} < 20$ MeV are listed.
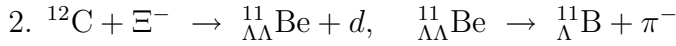
Target	#1	#2		$B_{\Lambda\Lambda}$ [MeV]	$\Delta B_{\Lambda\Lambda}$ [MeV]
^{12}C	$^{9}_{\Lambda\Lambda}$Be	t	$1n$	28.7 ± 1.0	15.0 ± 1.0
^{12}C	$^{10}_{\Lambda\Lambda}$Be	p	$2n$	> 18.0	> 4.6
^{12}C	$^{10}_{\Lambda\Lambda}$Be	d	$1n$	15.8 ± 1.1	2.4 ± 1.1
^{12}C	$^{10}_{\Lambda\Lambda}$Be	t		9.1 ± 0.3	-4.3 ± 0.3
^{12}C	$^{11}_{\Lambda\Lambda}$Be	p	$1n$	20.0 ± 1.9	1.8 ± 1.9
^{12}C	$^{11}_{\Lambda\Lambda}$Be	d		12.4 ± 0.3	-5.8 ± 0.3
^{14}N	$^{11}_{\Lambda\Lambda}$B	p	$3n$	> 33.0	> 15.2
^{14}N	$^{11}_{\Lambda\Lambda}$B	d	$2n$	> 30.6	> 12.8
^{14}N	$^{11}_{\Lambda\Lambda}$B	t	$1n$	24.6 ± 1.5	6.8 ± 1.5
^{14}N	$^{12}_{\Lambda\Lambda}$B	p	$2n$	> 27.3	> 6.8
^{14}N	$^{12}_{\Lambda\Lambda}$B	d	$1n$	25.6 ± 2.3	5.1 ± 2.3
^{14}N	$^{12}_{\Lambda\Lambda}$B	t		14.1 ± 0.4	-6.3 ± 0.4
^{14}N	$^{13}_{\Lambda\Lambda}$B	p	$1n$	24.3 ± 3.5	1.5 ± 3.5
^{16}O	$^{12}_{\Lambda\Lambda}$B	^{4}He	$1n$	40.3 ± 3.3	19.9 ± 3.3
^{16}O	$^{13}_{\Lambda\Lambda}$B	^{3}He	$1n$	39.6 ± 2.1	16.8 ± 2.1
^{16}O	$^{14}_{\Lambda\Lambda}$B	^{3}He		33.5 ± 0.5	10.7 ± 0.5
^{16}O	$^{13}_{\Lambda\Lambda}$C	d	$2n$	> 40.8	> 19.2
^{16}O	$^{13}_{\Lambda\Lambda}$C	t	$1n$	35.4 ± 2.7	13.8 ± 2.7
^{16}O	$^{14}_{\Lambda\Lambda}$C	p	$2n$	> 29.1	> 5.8
^{16}O	$^{14}_{\Lambda\Lambda}$C	d	$1n$	29.5 ± 3.9	6.1 ± 3.9
^{16}O	$^{15}_{\Lambda\Lambda}$C	p	$1n$	38.2 ± 5.4	13.9 ± 5.4

hypernucleus (track#3).

Taking into account the possibility of the productions in excited states, the following six interpretations satisfies the consistency of the values of $B_{\Lambda\Lambda}$ and $\Delta B_{\Lambda\Lambda}$ between Table C.2 and Table C.3.

1. $^{12}\text{C} + \Xi^- \rightarrow {}^{10}_{\Lambda\Lambda}\text{Be} + t, \quad {}^{10}_{\Lambda\Lambda}\text{Be} \rightarrow {}^{10}_{\Lambda}\text{B} + \pi^-$
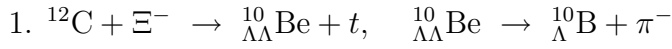
   By applying the kinematic fits both on the production vertex A and on the decay vertex B, we obtained $\Delta B_{\Lambda\Lambda} - B_{\Xi^-} = -4.30 \pm 0.20$ MeV and $\Delta B_{\Lambda\Lambda} = -4.41 \pm 0.77$ MeV, respectively. If we assume the Ξ^- hyperon was captured from an atomic $3D$ state of ^{12}C ($B_{\Xi^-} = 0.13$ MeV), the mean value of $\Delta B_{\Lambda\Lambda}$ was -4.18 ± 0.20 MeV.

2. $^{12}\text{C} + \Xi^- \rightarrow {}^{11}_{\Lambda\Lambda}\text{Be} + d, \quad {}^{11}_{\Lambda\Lambda}\text{Be} \rightarrow {}^{11}_{\Lambda}\text{B} + \pi^-$

   The kinematic fits on the production vertex A and the decay vertex B resulted in $\Delta B_{\Lambda\Lambda} - B_{\Xi^-} = -6.80 \pm 0.47$ MeV and $\Delta B_{\Lambda\Lambda} = -1.04 \pm 0.88$ MeV, respectively. This interpretation is possible if the ${}^{11}_{\Lambda\Lambda}\text{Be}$, ${}^{11}_{\Lambda}\text{B}$, or both were produced in excited states. If the ${}^{11}_{\Lambda}\text{B}$ was produced in the ground state, and if the Ξ^- hyperon was assumed to be captured from an atomic $3D$ state of ^{12}C, the excitation energy of ${}^{11}_{\Lambda\Lambda}\text{Be}$ was $E_x = 5.63 \pm 0.78$ MeV.
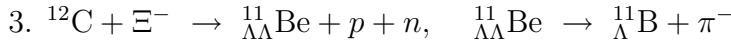
3. $^{12}\text{C} + \Xi^- \rightarrow {}^{11}_{\Lambda\Lambda}\text{Be} + p + n, \quad {}^{11}_{\Lambda\Lambda}\text{Be} \rightarrow {}^{11}_{\Lambda}\text{B} + \pi^-$

   Since this mode includes the neutron emission from the production vertex A, the kinematic fit can not be applied on the vertex. We obtained $\Delta B_{\Lambda\Lambda} - B_{\Xi^-} = 1.80 \pm 1.99$ MeV from the production vertex. As for the decay vertex B, which is same as the previous interpretation, the kinematic fit gave $\Delta B_{\Lambda\Lambda} = -1.04 \pm 0.88$ MeV. With the assumption of the Ξ^- hyperon capture from an atomic $3D$ state of ^{12}C, the mean value of $\Delta B_{\Lambda\Lambda}$ was -0.65 ± 0.83 MeV.

4. $^{14}\text{N} + \Xi^- \rightarrow {}^{12}_{\Lambda\Lambda}\text{B} + d + n, \quad {}^{12}_{\Lambda\Lambda}\text{B} \rightarrow {}^{12}_{\Lambda}\text{C} + \pi^-$
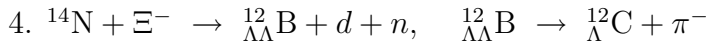
   We obtained $\Delta B_{\Lambda\Lambda} - B_{\Xi^-} = 5.14 \pm 2.26$ MeV from the production vertex A, where the kinematic fit can not be applied due to the neutron emission. The kinematic fit on the decay point B yielded $\Delta B_{\Lambda\Lambda} = -0.46 \pm 0.79$ MeV. Although there is a large discrepancy between the values of B_{Ξ^-} from the two vertices, this interpretation can not be excluded because of the large error of the value. By assuming the Ξ^- hyperon absorption from an atomic $3D$ state of ^{14}N ($B_{\Xi^-} = 0.17$ MeV), the mean value of $\Delta B_{\Lambda\Lambda}$ was obtained to be 0.15 ± 0.74 MeV.

5. $^{14}\text{N} + \Xi^- \rightarrow {}^{12}_{\Lambda\Lambda}\text{B} + t, \quad {}^{12}_{\Lambda\Lambda}\text{B} \rightarrow {}^{12}_{\Lambda}\text{C} + \pi^-$
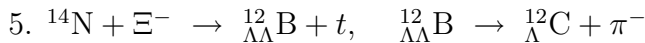
Table C.4: Possible values of $B_{\Lambda\Lambda}$, $\Delta B_{\Lambda\Lambda}$, and the excitation energy E_x of the double-hypernucleus.

species	$B_{\Lambda\Lambda}$ [MeV]	$\Delta B_{\Lambda\Lambda}$ [MeV]	E_x [MeV]
$^{10}_{\Lambda\Lambda}$Be	9.24 ± 0.18	-4.18 ± 0.20	0
$^{11}_{\Lambda\Lambda}$Be (2-body)	11.55 ± 0.17 $\sim 17.18 \pm 0.76$	-6.67 ± 0.47 $\sim -1.04 \pm 0.88$	$0 \sim 5.63 \pm 0.78$
$^{11}_{\Lambda\Lambda}$Be (3-body)	17.58 ± 0.71	-0.65 ± 0.83	0
$^{12}_{\Lambda\Lambda}$B (3-body)	20.64 ± 0.74	0.15 ± 0.74	0
$^{12}_{\Lambda\Lambda}$B $\left(^{12}_{\Lambda\Lambda}\text{B}^*\right)$	20.02 ± 0.78	-0.46 ± 0.79	6.94 ± 0.80
$^{12}_{\Lambda\Lambda}$B $\left(^{12}_{\Lambda\Lambda}\text{B}^*, \,^{12}_{\Lambda}\text{C}^*\right)$	17.31 ± 0.79	-3.17 ± 0.80	4.23 ± 0.81
$^{12}_{\Lambda\Lambda}$B $\left(^{12}_{\Lambda}\text{C}^*\right)$	13.13 ± 0.18	-7.36 ± 0.21	0
$^{13}_{\Lambda\Lambda}$B	28.04 ± 0.74	5.30 ± 0.75	0
$^{13}_{\Lambda\Lambda}$B $\left(^{13}_{\Lambda}\text{C}^*\right)$	23.4 ± 0.7	0.6 ± 0.8	0

The kinematic fits on the production vertex A and the decay vertex B gave $\Delta B_{\Lambda\Lambda} - B_{\Xi^-} = -7.57 \pm 0.21$ MeV and $\Delta B_{\Lambda\Lambda} = -0.46 \pm 0.79$ MeV, respectively. If the Ξ^- hyperon was assumed to be captured from an atomic $3D$ state of ^{14}N, and if the $^{12}_{\Lambda}$C was produced in the excited state of $E_x = 6.05$ MeV, the mean value of $\Delta B_{\Lambda\Lambda}$ was -7.36 ± 0.21 MeV. If the $^{12}_{\Lambda}$C was produced in the first excited state of $E_x = 2.71$ MeV, the value of $\Delta B_{\Lambda\Lambda}$ was -3.17 ± 0.80 MeV and the excitation energy of $^{12}_{\Lambda\Lambda}$B was $E_x = 4.23 \pm 0.81$ MeV. If the $^{12}_{\Lambda}$C was produced in the ground state, the excitation energy of $^{12}_{\Lambda\Lambda}$B was $E_x = 6.94 \pm 0.80$ MeV.
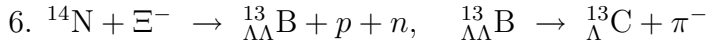
6. $^{14}\text{N} + \Xi^- \; \rightarrow \; ^{13}_{\Lambda\Lambda}\text{B} + p + n, \quad ^{13}_{\Lambda\Lambda}\text{B} \; \rightarrow \; ^{13}_{\Lambda}\text{C} + \pi^-$

Since this mode includes the neutron emission from the production vertex A, the kinematic fit can not be applied on the vertex. We obtained $\Delta B_{\Lambda\Lambda} - B_{\Xi^-} = 1.51 \pm 3.50$ MeV from the production vertex. By applying the kinematic fit on the decay vertex B, we obtained $\Delta B_{\Lambda\Lambda} = 5.47 \pm 0.77$ MeV. If we assume that the Ξ^- hyperon was captured from an atomic $3D$ state of ^{14}N, and that the $^{13}_{\Lambda}$C was produced in the ground state, the value of $\Delta B_{\Lambda\Lambda}$ was 5.30 ± 0.75 MeV. If the $^{13}_{\Lambda}$C was produced in the excited state of $E_x = 4.9$ MeV, the value was reduced to 0.6 ± 0.8 MeV.

The possible values of $B_{\Lambda\Lambda}$, $\Delta B_{\Lambda\Lambda}$, and the excitation energy E_x of the double-hypernucleus are summarized in Table C.4. If we expect that the value of $\Delta B_{\Lambda\Lambda}$ does not vary drastically depending on the species, the most probable interpretation is the excited single-hypernuclear production in the case 6;

$$^{14}\text{N} + \Xi^- \; \rightarrow \; ^{13}_{\Lambda\Lambda}\text{B} + p + n,$$
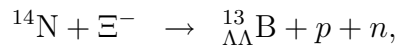
$$\begin{aligned}
{}^{13}_{\Lambda\Lambda}\mathrm{B} &\rightarrow {}^{13}_{\Lambda}\mathrm{C}^* + \pi^-, \\
B_{\Lambda\Lambda} &= 23.4 \pm 0.7 \ \text{MeV}, \\
\Delta B_{\Lambda\Lambda} &= 0.6 \pm 0.8 \ \text{MeV}.
\end{aligned}$$

C.2   "Kariya" event

The E176 experiment has been reported another example of the formation of doubly strange nuclear system, called "Kariya" event [96]. It could be interpreted as the production of a double-hypernucleus or twin-hypernuclei, depending on the Ξ^- hyperon capture point.

Schematic drawings of both interpretations and a photograph taken with an optical microscope as well as three-dimensional images obtained by a Laser Scanning Microscope System (LSM) are shown in Fig. C.2. If the event is interpreted as the sequential decay of a double-hypernucleus, a Ξ^- hyperon was captured at point A, from which two charged particles (#1, #3) were emitted. The particle of track#1 decayed into three charged particles (#2, #4, #5) at point B, and one of them (track#2) decayed again into a π^- meson (track#8) and two other charged particles (#6, #7) at point C. In the interpretation of twin hypernuclei emission, on the other hand, a Ξ^- hyperon was stopped at point A'. Two charged particles (#1', #2') were emitted from there, both of which decayed into three charged particles (#3', #4, #5, and #6, #7, #8) at point B and C, respectively. The lengths and angles of these tracks are summarized in Table C.5 and Table C.6.

First, the event reconstruction was performed on the decay vertex C of the single-hypernucleus (track#2 or #2'), which is common to both of the interpretations of a double-hypernucleus and twin hypernuclei. Same parameter as in the analysis of the double-hypernucleus event was used for the range-energy relation. We selected the possible decay modes, where the total energy release, E_{total}, agreed with the Q-value within three standard deviations. Additionally, in the modes without neutron emission, the momentum balance needed to be established within three standard deviations. As a result, the single-hypernucleus was interpreted as ${}^3_\Lambda\mathrm{H}$ or ${}^4_\Lambda\mathrm{H}$, as listed in Table C.7.

In the case of the production of a double-hypernucleus, the reconstruction of the production mode was made at point A with the assumption of the Ξ^- hyperon capture from a light nucleus in emulsion. The results for $\Delta B_{\Lambda\Lambda} < 20$ MeV are listed in Table C.8. It was impossible to reconstruct the decay mode of the double-hypernucleus (track#1), because there remained so many interpretations with neutron emission on the decay vertex B. Since all of the modes listed in Table C.8 give very large value of $\Delta B_{\Lambda\Lambda}$ compared to that obtained from Nagara event, it is difficult to interpret the "Kariya" event as the production of a double-hypernucleus.

In the case of twin-hypernuclear production, all possible production modes of the twin hypernuclei are listed in Table C.9. Although it was not required in the reconstruction on the production vertex that one of the single-hypernuclei
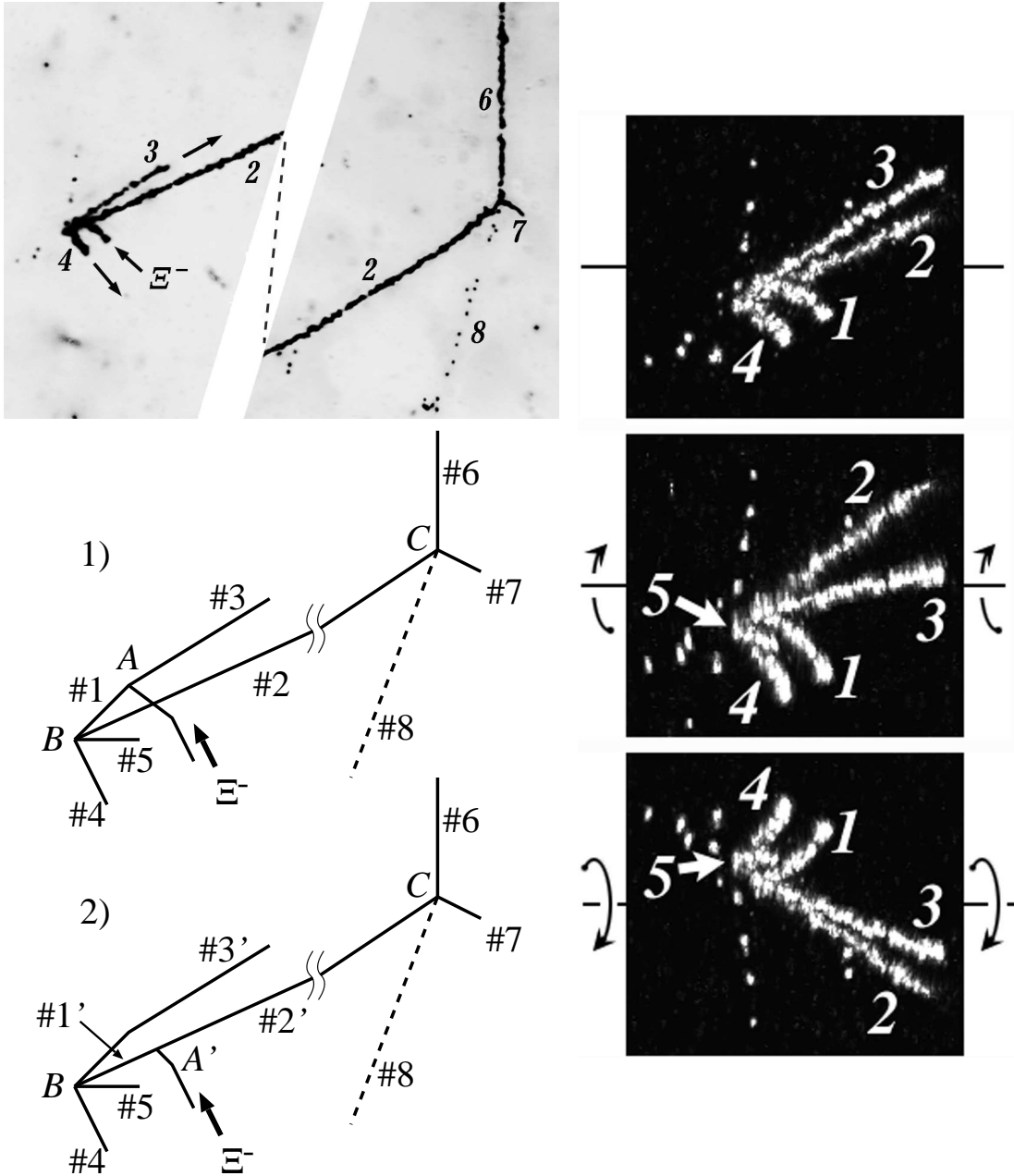
Figure C.2: Photographs and schematic drawings of "Kariya" event. 1) is for the interpretation of a double-hypernuclear production, while 2) is for that of twin-hypernuclear emission. a), b), and c) are three-dimensional images around the Ξ^- hyperon capture point obtained by a LSM.

Table C.5: Lengths and angles of tracks with the interpretation of a double-hypernucleus.

point	track#	length [μm]	θ [degree]	ϕ [degree]	
A	#1	2.4 ± 0.7	91.7 ± 0.5	137.8 ± 0.2	double-hyp.
	#3	2511.1 ± 75.3	120.7 ± 0.1	331.5 ± 1.1	
B	#2	287.5 ± 5.6	36.5 ± 0.1	335.1 ± 0.4	single-hyp.
	#4	90.7 ± 2.71	153.2 ± 0.1	46.9 ± 0.1	
	#5	7.6 ± 0.7	161.9 ± 0.1	331.5 ± 0.1	
C	#6	415.7 ± 12.5	47.7 ± 1.4	90.5 ± 0.6	
	#7	3.5 ± 0.7	129.1 ± 0.9	327.0 ± 3.2	
	#8	14087 ± 423	119.7 ± 3.0	254.1 ± 1.0	π^-

Table C.6: Lengths and angles of tracks with the interpretation of twin hypernuclei. The angle of track#1$'$ is opposite to that of track#2$'$.

point	track#	length [μm]	θ [degree]	ϕ [degree]	
A'	#1$'$	3.9 ± 0.7	-	-	single-hyp.
	#2$'$	283.5 ± 5.5	36.5 ± 0.1	335.1 ± 0.4	single-hyp.
B	#3$'$	2513.5 ± 75.4	120.7 ± 0.1	331.5 ± 1.1	
	#4	90.7 ± 2.71	153.2 ± 0.1	46.9 ± 0.1	
	#5	7.6 ± 0.7	161.9 ± 0.1	331.5 ± 0.1	
C	#6	415.7 ± 12.5	47.7 ± 1.4	90.5 ± 0.6	
	#7	3.5 ± 0.7	129.1 ± 0.9	327.0 ± 3.2	
	#8	14087 ± 423	119.7 ± 3.0	254.1 ± 1.0	π^-

Table C.7: Possible decay modes of the hypernucleus (track#2 or #2$'$).

hypernucleus	#6	#7	#8		Q-value [MeV]	E_{total} [MeV]
$^3_\Lambda$H	p	p	π^-	$1n$	35.5	36.3 ± 0.7
$^3_\Lambda$H	p	d	π^-		37.7	36.1 ± 0.7
$^4_\Lambda$H	p	t	π^-		35.8	36.0 ± 0.7

Table C.8: Possible production modes of the double-hypernucleus. The errors on the mass of Ξ^- hyperon and the binding energies of single-hypernuclei are not included in the errors on $B_{\Lambda\Lambda}$ and $\Delta B_{\Lambda\Lambda}$. Only the cases of $\Delta B_{\Lambda\Lambda} < 20$ MeV are listed.

Target	#1		#2		$B_{\Lambda\Lambda}$ [MeV]	$\Delta B_{\Lambda\Lambda}$ [MeV]
^{12}C	$^{11}_{\Lambda\Lambda}$Be	p		$1n$	37.5 ± 1.1	19.3 ± 1.1
^{14}N	$^{12}_{\Lambda\Lambda}$B	p		$2n$	> 39.9	> 19.4
^{14}N	$^{13}_{\Lambda\Lambda}$B	p		$1n$	32.2 ± 1.1	9.5 ± 1.1
^{16}O	$^{14}_{\Lambda\Lambda}$C	p		$2n$	> 36.4	> 13.0
^{16}O	$^{15}_{\Lambda\Lambda}$C	p		$1n$	36.0 ± 2.8	11.6 ± 2.8

Table C.9: Possible production modes of the twin hypernuclei.

Target	#1′	#2′	Q-value [MeV]	E_{total} [MeV]	B_{Ξ^-} [MeV]
^{14}N	$^{12}_{\Lambda}$B	$^{3}_{\Lambda}$H	13.5	13.1 ± 0.7	0.4 ± 0.7
^{16}O	$^{14}_{\Lambda}$C	$^{3}_{\Lambda}$H	12.2	13.9 ± 0.9	-1.6 ± 0.9
^{16}O	$^{13}_{\Lambda}$C	$^{4}_{\Lambda}$H	15.0	15.3 ± 0.9	-0.3 ± 0.9

(track#2′) should be $^{3}_{\Lambda}$H or $^{4}_{\Lambda}$H, all possible modes included $^{3}_{\Lambda}$H or $^{4}_{\Lambda}$H as the species of track#2′. The event reconstruction on the decay vertex B of the other single-hypernucleus (track#1′) could not be made because of so many possible decay modes with neutron emission.

Hence, we concluded that the "Kariya" event was interpreted much likely as the emission of twin-hypernuclei, either of followings;

$$
\begin{aligned}
^{14}\text{N} + \Xi^- &\rightarrow {}^{12}_{\Lambda}\text{B} + {}^{3}_{\Lambda}\text{H}, \\
^{16}\text{O} + \Xi^- &\rightarrow {}^{14}_{\Lambda}\text{C} + {}^{3}_{\Lambda}\text{H}, \\
^{16}\text{O} + \Xi^- &\rightarrow {}^{13}_{\Lambda}\text{C} + {}^{4}_{\Lambda}\text{H}.
\end{aligned}
$$
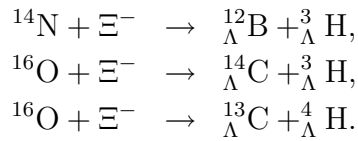
By applying the kinematic fit on the production vertex, the Ξ^- binding energy, B_{Ξ^-}, for each mode was obtained to be 0.79 ± 0.25 MeV, 0.07 ± 0.41 MeV, and 0.01 ± 0.29 MeV, respectively. The values of B_{Ξ^-} of the last two modes are consistent with the Ξ^- hyperon absorption from an atomic $3D$ state of the target ^{16}O nucleus (0.23 MeV), whereas that of the first production mode can be considered as the Ξ^- hyperon capture from an atomic $2P$ state of ^{14}N.

Bibliography

[1] R. L. Jaffe, Phys. Rev. Lett. **38** (1977) 195–198.

[2] T. Sakai, K. Shimizu, and K. Yazaki, Prog. Theor. Phys. Suppl. **137** (2000) 121.

[3] Y. C. Tang and R. C. Herndon, Phys. Rev. Lett. **14** (1965) 991.

[4] A. R. Bodmer, Q. N. Usmani, and J. Carson, Nucl. Phys. **A422** (1984) 510–526.

[5] X.-c. Wang, H. Takaki, and H. Bando, Prog. Theor. Phys. **76** (1986) 865.

[6] H. Bando, Prog. Theor. Phys. **67** (1982) 699.

[7] Y. Yamamoto, H. Takaki, and K. Ikeda, Prog. Theor. Phys. **86** (1991) 867.

[8] Y. Yamamoto, T. Motoba, H. Himeno, K. Ikeda, and S. Nagata, Prog. Theor. Phys. Suppl. **117** (1994) 361.

[9] H. Himeno, T. Sakuda, S. Nagata, and Y. Yamamoto, Prog. Theor. Phys. **89** (1993) 109.

[10] S. B. Carr, I. R. Afnan, and B. F. Gibson, Nucl. Phys. **A625** (1997) 143.

[11] T. Yamada and C. Nakamoto, Phys. Rev. **C62** (2000) 034319.

[12] J. Schaffner *et al.*, Ann. Phys. **235** (1994) 35–76.

[13] M. M. Nagels, T. A. Rijken, and J. J. de Swart, Phys. Rev. **D12** (1975) 744.

[14] M. M. Nagels, T. A. Rijken, and J. J. de Swart, Phys. Rev. **D15** (1977) 2547.

[15] M. M. Nagels, T. A. Rijken, and J. J. de Swart, Phys. Rev. **D20** (1979) 1633.

[16] P. M. M. Maessen, T. A. Rijken, and J. J. de Swart, Phys. Rev. **C40** (1989) 2226.

[17] T. A. Rijken, V. G. J. Stoks, and Y. Yamamoto, Phys. Rev. **C59** (1999) 21.

[18] T. A. Rijken, Nucl. Phys. **A691** (2001) 322c.

[19] T. Ueda *et al.*, Prog. Theor. Phys. **99** (1998) 891.

[20] Y. Fujiwara, C. Nakamoto, and Y. Suzuki, Phys. Rev. Lett. **76** (1996) 2242–2245.

[21] Y. Fujiwara, C. Nakamoto, and Y. Suzuki, Phys. Rev. **C54** (1996) 2180–2200.

[22] M. Prakash, M. Prakash, J. M. Lattimer, and C. J. Pethick, Astrophys. J. **390** (1992) 77–80.

[23] S. Tsuruta, Phys. Rep. **292** (1998) 1–130.

[24] S. Balberg and N. Barnea, Phys. Rev. **C57** (1998) 409–416.

[25] T. Takatsuka and R. Tamagaki, Prog. Theor. Phys. **102** (1999) 1043–1048.

[26] D. Page, M. Prakash, J. M. Lattimer, and A. W. Steiner, Phys. Rev. Lett. **85** (2000) 2048–2051.

[27] T. Takatsuka, S. Nishizaki, Y. Yamamoto, and R. Tamagaki, Prog. Theor. Phys. **105** (2001) 179–184.

[28] M. Danysz *et al.*, Nucl. Phys. **49** (1963) 121.

[29] R. H. Dalitz, D. H. Davis, P. H. Fowler, A. Motwill, J. Pniewski, and J. A. Zakrzewski, Proc. Roy. Soc. Lond. **A426** (1989) 1.

[30] D. J. Prowse, Phys. Rev. Lett. **17** (1966) 782.

[31] A. S. Mondal, A. K. Basak, M. M. Kasim, and A. Husain, Nuov. Cim. **28A** (1975) 42.

[32] S. Aoki *et al.*, Prog. Theor. Phys. **85** (1991) 1287–1298.

[33] C. B. Dover, D. J. Millener, A. Gal, and D. H. Davis, Phys. Rev. **C44** (1991) 1905.

[34] S. Aoki *et al.*, Prog. Theor. Phys. **85** (1991) 951–956.

[35] J. K. Ahn *et al.*, Phys. Rev. Lett. **87** (2001) 132504.

[36] S. Aoki *et al.*, Prog. Theor. Phys. **89** (1993) 493–500.

[37] S. Aoki *et al.*, Phys. Lett. **B355** (1995) 45.

[38] B. Bhowmik, Nuov. Cim. **29** (1963) 1.

[39] D. H. Wilkinson, S. J. S. Lorant, D. K. Robinson, and S. Lokanathan, Phys. Rev. Lett. **3** (1959) 397.

[40] P. Khaustov *et al.*, Phys. Rev. **C61** (2000) 054603.

[41] S. Aoki *et al.*, Phys. Rev. Lett. **65** (1990) 1729–1732.

[42] J. K. Ahn *et al.*, Phys. Lett. **B378** (1996) 53–58.

[43] J. K. Ahn *et al.*, Phys. Rev. **C62** (2000) 055201.

[44] R. E. Chrien, Nucl. Phys. **A629** (1998) 388c.

[45] B. Bassalleck, Nucl. Phys. **A639** (1998) 401.

[46] A. Yamamoto *et al.*, Nucl. Instr. Meth. **203** (1982) 35.

[47] C. B. Dover and A. Gal Brookhaven Nat. Lab. Upton - BNL-31728 (REC.SEP.82) 75p.

[48] M. Ishino *et al.*, Nucl. Instr. Meth. **457** (2001) 581.

[49] S. Yamashita, Ph.D. thesis, Kyoto University (1995), (unpublished).

[50] H. Torii, Master's thesis, Kyoto University (1998), (unpublished).

[51] D. E. Alburger and M. May, Nucl. Instrum. Meth. **A443** (2000) 27.

[52] T. Iijima *et al.*, Nucl. Phys. **A546** (1992) 588–606.

[53] H. Akikawa *et al.*, to be submitted to Nucl. Instrum. Meth. A.

[54] Y. H. Iwata, Master's thesis, Gifu University (2000), (unpublished).

[55] H. Tanaka, Master's thesis, Aichi University of Education (1998), (unpublished).

[56] A. Ichikawa *et al.*, Nucl. Instrum. Meth. **A417** (1998) 220.

[57] J. K. Ahn *et al.*, Nucl. Instr. Meth. **A457** (2001) 137.

[58] M. Suehiro, Master's thesis, Kyoto University (1995), (unpublished).

[59] T. Tabaru, Master's thesis, Kyoto University (1996), (unpublished).

[60] J. K. Ahn *et al.*, Phys. Lett. **B444** (1998) 267.

[61] A. Ichikawa, Ph.D. thesis, Kyoto University (2001), (unpublished).

[62] A. Ichikawa *et al.*, to be submitted to Nucl. Instrum. Meth. A.

[63] S. Aoki *et al.*, Nucl. Instrum. Meth. **B51** (1990) 466.

[64] S. Aoki *et al.*, to be submitted.

[65] J. K. Ahn *et al.*, Proceedings of International Symposium on Hadrons and Nuclei, Seoul, Korea, 2001, AIP Conf. Proc. **594** (2001) 180.

[66] A. Ichikawa *et al.*, Phys. Lett. **B500** (2001) 37–46.

[67] J. F. Ziegler and J. P. Biersack, ©IBM Co., `http://www.srim.org/`.

[68] H. H. Heckman *et al.*, Phys. Rev. **117** (1960) 544.

[69] W. H. Barkas *et al.*, Nuov. Cim. **8** (1958) 185.

[70] Y. S. Iwata, Master's thesis, Gifu University (2002), (unpublished).

[71] C. F. Powell, P. H. Fowler, and D. H. Perkins, The Study of Elementary Particles by the Photographic Method, Pergamon Press, 1959, and references in there.

[72] W. H. Barkas *et al.*, Phys. Rev. **98** (1955) 605.

[73] M. Juric *et al.*, Nucl. Phys. **B52** (1973) 1.

[74] H. Bando, K. Ikeda, and T. Motoba, Prog. Theor. Phys. **66** (1981) 1344.

[75] H. Bando, K. Ikeda, and T. Motoba, Prog. Theor. Phys. **67** (1982) 508.

[76] D. E. Groom *et al.*, Eur. Phys. J. **C15** (2000) 1.

[77] C. J. Batty, E. Friedman, and A. Gal, Phys. Rev. **C59** (1999) 295.

[78] D. Zhu, C. B. Dover, A. Gal, and M. May, Phys. Rev. Lett. **67** (1991) 2268.

[79] T. Koike, (private communication).

[80] H. Akikawa *et al.*, Phys. Rev. Lett. **88** (2002) 082501.

[81] I. N. Filikhin and A. Gal, Phys. Rev. **C65** (2002) 041001.

[82] E. Hiyama, M. Kamimura, T. Motoba, T. Yamada, and Y. Yamamoto, Phys. Rev. **C66** (2002) 024007.

[83] K. S. Myint, S. Shinmura, and Y. Akaishi, Eur. Phys. J. **A16** (2003) 21–26.

[84] Y. Fujiwara, M. Kohno, C. Nakamoto, and Y. Suzuki, Phys. Rev. **C64** (2001) 054001.

[85] S. Nishizaki, T. Takatsuka, and Y. Yamamoto, Prog. Theor. Phys. **108** (2002) 703–718.

[86] T. Takatsuka, Proceedings of Recent Progress of Strangeness Nuclear Physics, Tsukuba, Japan, 2002, KEK Proceedings **2002-29** (2003) 210–216.

[87] R. W. Stotzer *et al.*, Phys. Rev. Lett. **78** (1997) 3646.

[88] K. Yamamoto *et al.*, Phys. Lett. **B478** (2000) 401–407.

[89] A. T. M. Aerts and C. B. Dover, Phys. Rev. **D28** (1983) 450, the modified calculation is presented in Ref. [88].

[90] K. Imai *et al.*, kEK-PS E522 proposal (2002).

[91] K. Itonaga, T. Ueda, and T. Motoba, talk at VII International Conference on Hypernuclear and Strange Particle Physics (HYP2000) Torino, Oct 2000.

[92] A. Parreño, A. Ramos, and C. Bennhold, Phys. Rev. **C65** (2002) 015205.

[93] J. K. Ahn *et al.*, Nucl. Phys. **A625** (1997) 231.

[94] G. Bohm *et al.*, Acta Physica Polonika **A37** (1970) 135.

[95] T. Hasegawa *et al.*, Phys. Rev. **C53** (1996) 1210–1220.

[96] K. Nakazawa *et al.*, Proceedings of the 23rd INS International Symposium (1995) 261.

[97] O. Hashimoto *et al.*, Phys. Rev. Lett. **88** (2002) 042503.

[98] Y. Sato, Ph.D. thesis, Tohoku University (1999), (unpublished).

[99] A. Ramos, M. Vicente-Vacas, and O. E., nucl-th/0206036 .

[100] Y. Sato, (private communication).

List of Figures

List of Tables